Interface Optimization for Improved Photovoltaic Devices

Thesis by
Rebecca Denise Glaudell

In Partial Fulfillment of the Requirements for the
Degree of
Doctor of Philosophy in Physics

CALIFORNIA INSTITUTE OF TECHNOLOGY
Pasadena, California

2022
Defended August 9, 2021

ACKNOWLEDGEMENTS

The information, data, or work presented herein was funded in part by the U.S. Department of Energy through the Bay Area Photovoltaic Consortium under Award Number DE-EE0004946 and additionally through the Energy Efficiency and Renewable Energy Program, under Award Number DE-EE0006335 for Quantum Energy and Sustainable Solar Technology Engineering Research Center; by the National Science Foundation (NSF) Graduate Research Fellowship under Grant No. 1144469; and in part by the NSF and the Department of Energy (DOE) under NSF CA No. EEC-1041895. Any opinions, findings and conclusions or recommendations or expressed in this material are those of the author(s) and do not necessarily reflect those of NSF or DOE. We acknowledge support from the Beckman Institute of the California Institute of Technology to the Molecular Materials Research Center, where XPS data were collected.

Thanks to my advisor Prof. Harry Atwater, my thesis committee chair Prof. David Hsieh, and members Profs. Gil Refael and Axel Scherer, and my candidacy committee chair Prof. Andrei Faraon. Thanks to my first research mentor at Caltech, Alireza Ghaffari, who was always willing to lend a hand or just chat. Thanks to Bruce Brunschwig for keeping the MMRC running. Thanks to all the faculty, staff, and students in QESST for their support and inspiration, especially Prof. Stuart Bowden, Prof. Christiana Honsberg, Andre Augusto, and Pradeep Balaji. Thanks to all the administrative staff in the Atwater Group, in APhMS, in Physics, in EAS, and in PMA for keeping things going.

I could not possibly name all the students and postdocs who have influenced and enabled my thesis work, nor all my peers in Caltech organizations who have worked tirelessly to make Caltech and the world a better place, whether through music or socializing or activism.

Thanks to my family for the unconditional support. Thanks most to my partner Ron for all the laughs and thoughtful conversations along the way. My life is brighter with you in it.

ABSTRACT

The wide band gaps and superior conductivity of ZnS_xSe_{1-x} semiconductors to amorphous Si suggest an alternative carrier-selective contact in silicon heterojunction solar cells. Electron-selective ZnS_xSe_{1-x} front contacts on p-type c-Si solar cells are explored by simulating in Sentaurus TCAD a large design parameter space informed by experimentally determined optoelectronic properties. Comparable performance to experimental and simulated p-SHJ reference devices is shown, with a champion simulated device efficiency of 20.8%. X-ray photoelectron spectroscopy is used to measure band offsets at interfaces for the aforementioned ZnS_xSe_{1-x}-c-Si photovoltaic devices as well as various carrier-selective contacts and passivation layers for GaAs photovoltaic devices.

PUBLISHED CONTENT AND CONTRIBUTIONS

[1] R. Glaudell, “The Legacy of William Shockley: Racism and Ableism in STEM,” in *2021 IEEE 48th Photovoltaic Specialists Conference (PVSC)*,
R.G. participated in the conception of this work, gathered and analyzed data, and wrote the manuscript., Fort Lauderdale, FL, USA: IEEE, Jun. 20, 2021, pp. 1887–1889. doi: `10.1109/PVSC43889.2021.9518411`.

[2] R. Glaudell, P. Balaji, S. Bowden, A. Augusto, and H. A. Atwater, “ZnS$_x$se$_{1-x}$ carrier-selective contacts for silicon photovoltaics,” in *2021 IEEE 48th Photovoltaic Specialists Conference (PVSC)*,
R.G. participated in the conception of this project, fabricated samples, gathered and analyzed data, and wrote the manuscript., Fort Lauderdale, FL, USA: IEEE, Jun. 20, 2021, pp. 0652–0655. doi: `10.1109/PVSC43889.2021.9518976`.

[3] M. E. Phelan, M. M. Potter, P. Balaji, *et al.*, “Fabrication techniques for high-performance Si heterojunction (SHJ) microcells,” in *2021 IEEE 48th Photovoltaic Specialists Conference (PVSC)*,
R.G. gathered and analyzed data and helped write the manuscript., Fort Lauderdale, FL, USA: IEEE, Jun. 20, 2021, pp. 0330–0334. doi: `10.1109/PVSC43889.2021.9518579`.

[4] M. M. Potter, M. E. Phelan, P. Balaji, *et al.*, “Silicon heterojunction microcells,” *ACS Applied Materials & Interfaces*, vol. 13, no. 38, pp. 45 600–45 608, Sep. 29, 2021,
R.G. gathered and analyzed data and helped write the manuscript. doi: `10.1021/acsami.1c11122`.

[5] R. Glaudell, “Women* in Physics, Math and Astronomy at Caltech: Supporting Women in STEM,” in *2020 47th IEEE Photovoltaic Specialists Conference (PVSC)*,
R.G. conceived of this work, gathered and analyzed data, and wrote the manuscript., Calgary, AB, Canada: IEEE, Jun. 14, 2020, pp. 2147–2150. doi: `10.1109/PVSC45281.2020.9300477`.

[6] P. Jahelka, R. Glaudell, and H. Atwater, “Non-epitxaial GaAs/organic heterojunction solar cells with 830mv Voc,” in *2020 47th IEEE Photovoltaic Specialists Conference (PVSC)*,
R.G. gathered and analyzed data and helped write the manuscript., Calgary, AB, Canada: IEEE, Jun. 14, 2020, pp. 0649–0651. doi: `10.1109/PVSC45281.2020.9300460`.

[7] Y. Kim, P. C. Wu, R. Sokhoyan, *et al.*, “Phase modulation with electrically tunable vanadium dioxide phase-change metasurfaces,” *Nano Letters*, vol. 19, no. 6, pp. 3961–3968, Jun. 12, 2019,

R.G. gathered and analyzed data and helped write the manuscript. DOI: `10.1021/acs.nanolett.9b01246`.

[8] R. D. Glaudell and H. A. Atwater, “Energy band alignment of ZnS_xSe_{1-x} films on Si for photovoltaic carrier-selective contacts,” in *2018 IEEE 7th World Conference on Photovoltaic Energy Conversion (WCPEC) (A Joint Conference of 45th IEEE PVSC, 28th PVSEC & 34th EU PVSEC)*,
R.G. participated in the conception of this project, fabricated samples, gathered and analyzed data, and wrote the manuscript., Waikoloa Village, HI: IEEE, Jun. 2018, pp. 2132–2134. DOI: `10.1109/PVSC.2018.8548022`.

TABLE OF CONTENTS

LIST OF ILLUSTRATIONS

LIST OF TABLES

NOMENCLATURE

6N. Referring to the purity of a material by counting the number of consecutive nines in a decimal representation, i.e. 99.9999%.

Absorption. The physical or chemical process in which atoms, molecules, or ions enter some bulk phase liquid or solid material.

Adsorption. The adhesion of atoms, ions, or molecules from a gas, liquid, or dissolved solid to a surface.

Amorphous. Referring to materials lacking long-range order in atomic positioning, denoted by "a-” before crystal name, i.e. "a-Si”.

Atomic force microscopy. A highly sensitive technique that images a sample surface by measuring the deflection of a cantilever as it is scanned over a sample surface.

Band gap. The distance between the valence band of electrons and the conduction band; the minimum energy that is required to excite an electron up to the conduction band where is can participate in conduction.

Chemical vapor deposition, CVD. A vacuum deposition method used to produce high quality, high-performance solid materials.

Conduction band. The lowest energy band with available states for electron conduction.

Conductivity. A measure of a material’s ability to conduct and electric current.

Crystalline. Referring to materials with highly ordered microscopic structure, forming a lattice of atoms that extend in all directions, often denoted by "c-” before the crystal name, i.e. "c-Si”.

Czochralski method. A method of crystal growth used to obtain single crystals of semiconductors.

Desorption. The opposite process of sorption (adsorption or absorption) where an atom, ion, or molecule is released from or through a surface.

Diffraction. The process by which a beam of light or other system of waves is spread out as a result of passing through a narrow aperture or across an edge, such as those created by crystals.

Doping. The introduction of impurities into a semiconductor for the purpose of modulating its electrical, optical, and structural properties.

Effusion. A gas escaping from a containter through a hole considerably smaller than the mean free path of the molecules.

Energy-dispersive X-ray spectroscopy (EDS, EDX, EDAX). An analytical technique used for elemental analysis, relying on an interaction between X-ray excitation and a sample.

Epitaxy. A type of crystal growth or material deposition in which new crystalline layers are formed with one or more well-defined orientations with respect to a crystalline seed layer.

Ewald sphere. A geometric construction used in crystallography that demonstrates the relation between the wavevector of the incident and diffracted beams, the diffraction angle for a given reflection and the reciprocal lattice of the crystal.

Ex-situ. Off site, referring to events that take place with exposure to an external environment, not under vacuum.

Finite energy. An energy type whose source is not replenished on the same time scale at which it is consumed.

Fossil fuel. A natural fuel such as coal or gas, formed in the geological past from the remains of living organisms.

Heterojunction. An interface between two layers or regions of dissimilar semiconductors with unequal band gaps.

Hole. The absence of an electron at a position where one could exist in atomic lattice, leaving a net positive charge.

In-situ. Literally "on-site” in Latin, referring to an event that takes place without exposure to an external environment.

Isothermal. Uniform, constant temperature.

Lifetime. The average time before an excited charge carrier recombines..

Mean free path length. The average distance over which a moving particle travels before substantially changing its direction or energy, typically as a result of one or more successive collisions with other particles.

Mole fraction. A unit of the amount of a constituent (expressed in moles) divided by the total amount of all constituents in a mixture.

N-type. Referring to semiconductors with impurities that donate extra electrons to the bulk crystal conduction band..

Ohmic contact. A low resistance electrical junction between a metal and semiconductor where current varies linearly with applied voltage.

Open-circuit voltage, V_{oc}. The voltage at which no current flows across a device.

P-type. Referring to semiconductors with impurities that accept electrons from the bulk crystal valence band, creating extra holes..

Parasitic absorption. Light absorption that does not lead to a collected charge carrier.

Passivation. The inertness of a material, especially a surface, to carrier recombination.

Photon recycling. reabsorption of photons emitted after radiative recombination events.

Photovoltaic effect. The generation of voltage and electric current upon exposure to light. A physical and chemical phenomenon.

Photovoltaics (PV). The conversion of light into electricity using semiconducting materials that exhibit the photovoltaic effect.

Reciprocal lattice. The Fourier transform of another lattice. When applied to a physical lattice, such as a crystal, a representation of available momentum states.

Reflection high-energy electron diffraction (RHEED). A technique used to characterize the surface of crystalline materials.

Renewable energy. An energy type whose consumption one year does not directly impact how much is available for consumption the next year, i.e. solar energy, wind energy.

Resistivity. A fundamental property measuring how strongly a material resists electrical current.

Scanning electron microscope. A type of electron microscope that produces images of a sample by scanning the surface with a focused beam of electrons..

Semiconductor. A material with a electrical conductivity between that of an insulator (non-conducting) and most metals (conducting).

Short-circuit current, J_{sc}. The current at which a device is short-circuited, i.e. no voltage across the device.

Specular reflection. The mirror-like reflection of waves from a surface.

Stoichiometry. The relationship between the relative quantities of substances forming a compound.

Sublimation. The transition of a substance directly from the solid state to the gas state, without passing through the liquid state.

Substrate. An underlying substance or layer, the surface on which a material is deposited.

Surface reconstruction. The process by which atoms at the surface of a crystal assume a different structure than that of the bulk.

Transmission electron microscopy (TEM). A high-resolution imaging technique in which a beam of electrons passes through a thin sample to produce an image.

Triple point. The temperature and pressure at which the three phases (gas, liquid, and solid) of a substance coexist in thermodynamic equilibrium.

Vacuum. A space devoid of matter.

Valence band. The outermost band of electron orbitals that electrons can jump out of, moving into the conduction band when excited.

X-ray diffractometry (XRD). A measurement technique in which the atoms of a crystal cause an interference pattern of the waves present in an incident beam of X-rays, yielding information about the atomic spacing of the lattice.

X-ray photoelectron spectroscopy (XPS). A surface-sensitive quantitative technique based on the photoelectric effect that can identify the elements in a sample, their chemical state, and overall electronic structure.

X-ray reflectivity (XRR). A surface-sensitive analytical technique measuring the intensity a beam of X-rays reflected from flat surface as a function of incident X-ray angle.

Chapter 1

INTRODUCTION

1.1 Battling the Climate Crisis with Photovoltaics

As humans, we have access to energy sources of two types: renewable and finite. By renewable we refer to sources whose consumption one year does not directly impact how much is available for consumption the next year. A finite energy resource is not replenished on the same time scale at which we consume it. The volume of each sphere in Fig. 1.1 represents the amount of energy available each year from different renewable resources (adapted from [1]). This includes energy sources that depend on sunlight, such as the burning of biomass like wood, which requires sunlight to grow. The largest, yellow sphere represents energy from the sun, and the spheres that lay on top of it represent energy sources that are derived from sunlight. Less than 1% of sunlight is absorbed by organic matter through photosynthesis, represented

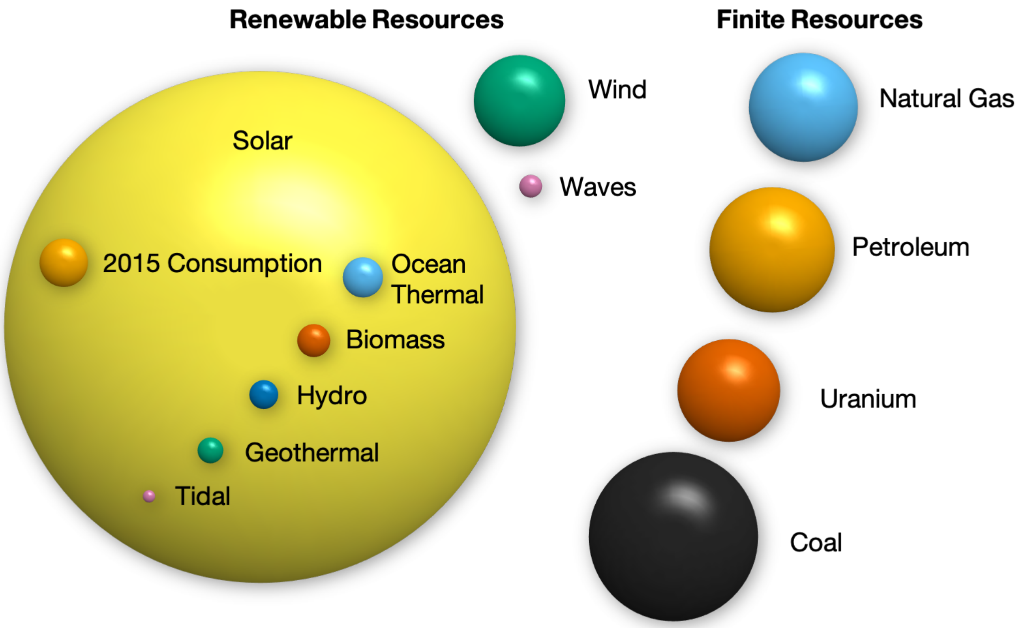

Figure 1.1: Representation of available terrestrial energy resources, adapted from [1]. Volume of spheres is proportional to maximum estimated annual available resource for renewables (left) and total available resource for finite resources (right). 2015 global consumption is also shown. Solar-derived renewable energy sources are overlaid on total solar resource.

by the green sphere on the left. For much of human history, our activities were limited to those that could be maintained by renewable resources, essentially limited by photosynthesis processes, and thus limited to accessible land. The land available limited the amount of food available. When humans gained control of fire, more land became habitable as heat could be provided throughout the year [2]. More energy could be extracted from food, and sufficient heat for tool production could be achieved. During the Neolithic Revolution, settled agriculture further reduced the competition for food between humans and animals, allowing for an order of magnitude population expansion [3].

Besides renewable resources, we also can use energy from finite resources, such as natural gas, petroleum, nuclear energy from uranium, and coal. Derived from decayed organic matter, the energy stored in carbon-based fossil fuels like coal is ultimately from the sun too, but it takes millions of years to reach this state, so is not renewable on human time scales. The spheres on the right of Fig. 1.1 represent the energy available through such finite resources of all known stores on Earth. Although coal has been used as a heat source as early as the Neolithic area, until the Industrial Revolution, most production needs were still met by land-limited resources [2], [4]. Heat was primarily produced through wood, which limited the output of metals which require significant heat to smelt. Other raw materials such as wool or leather required land and food for sheep and cattle, the tending of which also required significant human labor. Mechanical energy sources were limited to wind, water, and human or animal labor.

Before the Industrial Revolution, coal mining was limited to depths around 150 feet, below which mines would flood [2]. The late 17th century invention of the “Miner’s Friend” water pump sought to address this problem, but using only vacuum and no moving parts to move water, it was still limited in its feasible operating depths [5]. Especially in Britain where usable water ways for watermills would be exhausted by 1830, there was a demand for greater usage of the energy-dense coal. Eventually, high rates of coal production were enabled through the development of the steam engine, beginning with Newcomen’s atmospheric engine in 1712, optimized for draining mines, and coming into full force with James Watts’ higher efficiency steam engine in 1776. In Great Britain, the Industrial Revolution was underway, leading to an exponential increase in the per capita annual energy consumption, driven by coal, visualized in Fig. 1.2 [2]. However, as with all revolutions, there were costs. During the Neolithic Revolution, the change to cereal-based diets and denser populations correlated with a reduction in life expectancy, an increase in

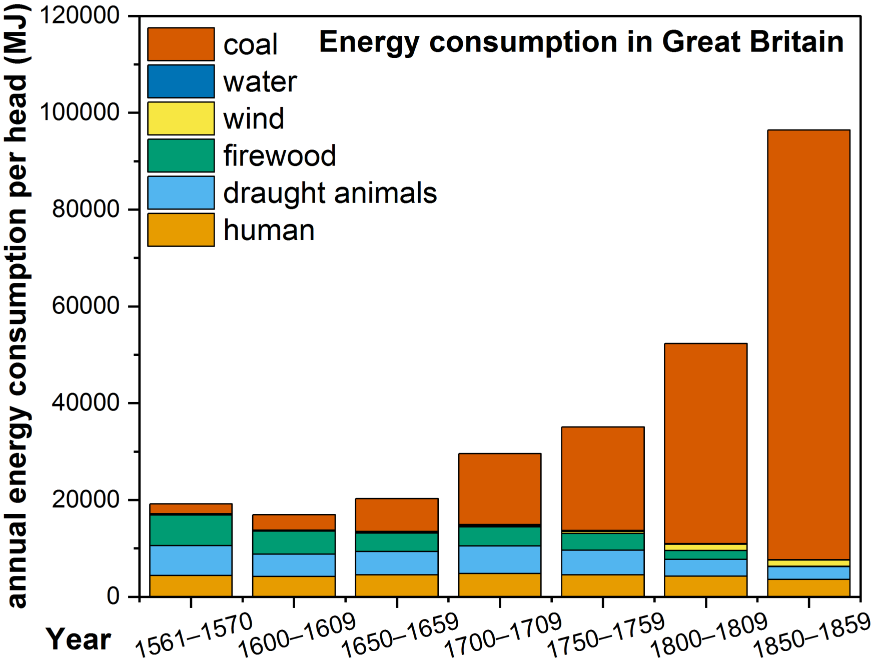

Figure 1.2: Average annual energy consumption per person in Great Britain by energy source for decades between 1561 and 1859 [2]. Energy source is designated by bar section color, stacked from top to bottom as coal (dark orange), water, wind, firewood, draught animals, and human. Coal-based energy consumption increases exponentially with time.

infant mortality, infectious diseases, and nutritional deficiencies [6], [7]. A social elite emerged and monopolized decision making, deepening social divisions and gender inequality [8], [9]. Before the Industrial Revolution, technological advances in sea travel enabled access to raw materials and labor outside of their local limits, through seizure of land from and enslavement and trafficking of indigenous peoples throughout the globe. With the Industrial Revolution came dangerous working and living conditions, again reduced nutritional access, and widespread child labor [10]. One of the most significant consequences of the energy revolution that enabled the Industrial Revolution is climate change.

The Industrial Revolution is considered one of the most significant periods of change in human history, following the domestication of animals. New energy-intensive technology enabled a boom in production and economic growth. The increasing demand for coal power with new technology, a growing population, and improving standards of living (for some) drove an unprecedented human effect on the Earth's atmosphere. The concentration in the atmosphere of greenhouse gases that trap heat near the Earth's surface began a steep climb, and soon to follow was a slow increase in the average global temperature, as shown in Fig. 1.3. Compared to the 1850–1900 baseline, the global average temperature has increased by 1.2°C [11]. The temperature rise on land is about twice that, leading to more frequent and more devastating wildfires and heatwaves [12]. Extreme weather events of all kinds have increased in frequency, leading to loss of life and destruction of cities. The burning of fossil fuels for energy consumption is the largest contributor to carbon dioxide and methane emissions, which are in turn the largest contributors to greenhouse gases and thus global warming. Fig. 1.4 shows how the rise in annual energy consumption is dominated by finite resource usage (coal, oil, and gas) and peaks with carbon dioxide atmospheric concentration. To slow or stop climate change, we must eliminate our reliance on fossil fuels in favor of a carbon-neutral future.

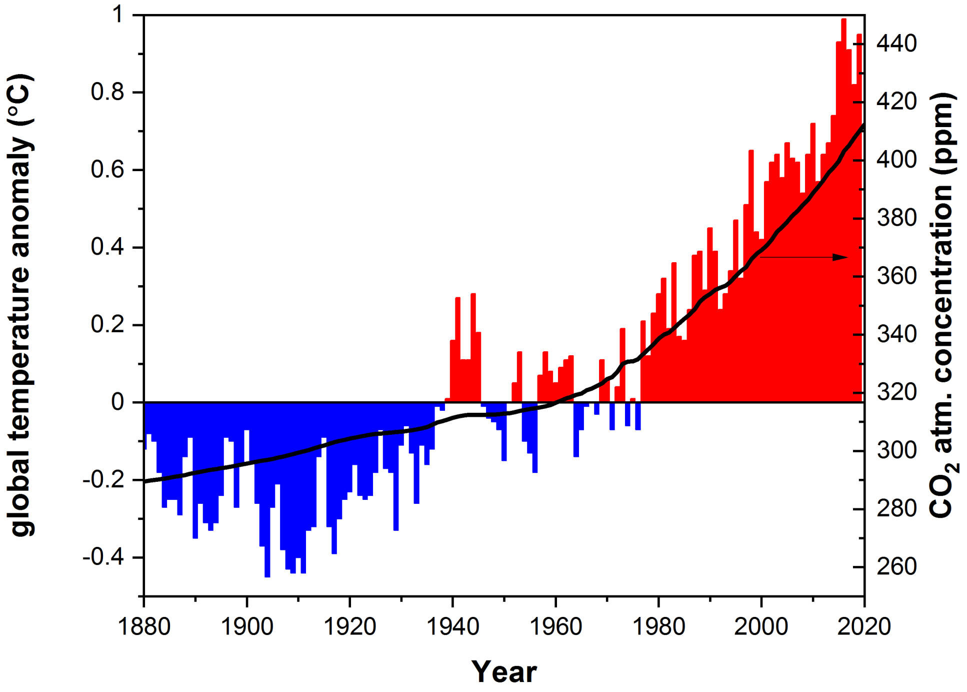

Figure 1.3: Average global temperature anomaly and CO_2 atmospheric concentration over time from 1880 to 2020 [11], [12]. The increase in global temperature follows the increase in CO_2 atmospheric concentration.

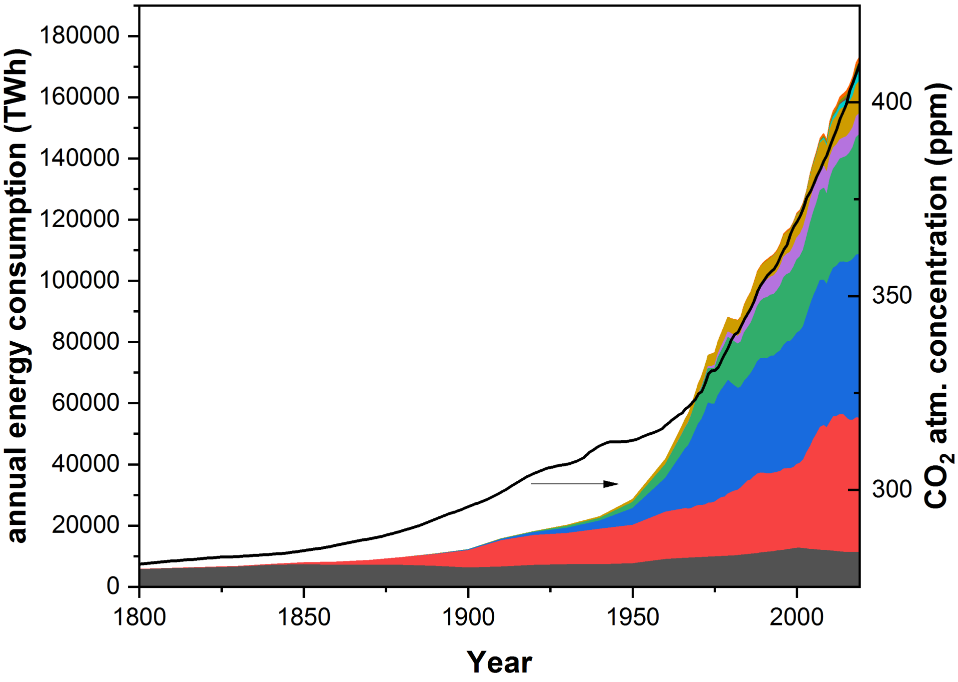

Figure 1.4: Average global energy consumption and CO_2 atmospheric concentration over time from 1800 to 2020 [11], [12]. The increase in CO_2 atmospheric concentration follows the increase in global energy consumption. From bottom to top, the annual energy consumption by type is separated into the categories biomass (gray), coal (red), oil (blue), gas (green), nuclear (purple), hydro (gold), wind (cyan), solar (brown), biofuel (olive), and other (orange).

At 23000 TWy/y, the energy that reaches the Earth as sunlight is much greater than all available fossil fuel resources and much greater than global annual energy needs. Sunlight can be converted to electricity via photovoltaic devices, where electric charge carriers are excited upon the absorption of photons within semiconductor materials. The efficiency at which incident sunpower can be converted to electrical power depends on how much light reaches the absorbing semiconductor and how many charge carriers are collected at the electrical contacts. Efficiency improvements lead to lower energy costs, greater renewable energy production, and when used to replace fossil fuels, the avoidance of further carbon dioxide emitted to the atmosphere. Thus we are motivated to reduce parasitic absorption and increase charge carrier collection, and do so by optimizing the interfaces of photovoltaic devices.

1.2 Crystalline Silicon Photovoltaics

Silicon photovoltaics (PV) have dominated the PV market since their debut in 1954. The current record efficiency for non-concentrated crystalline-Si–based solar cells was set at 26.6% by a variant of a silicon heterojunction (SHJ) cell by Kaneka [13]. We aim to improve upon a SHJ design by exchanging an amorphous Si carrier-selective contact (CSC) for Zn-based II-VI semiconductors to decrease parasitic absorption and increase conductivity.

1.3 Silicon Heterojunction Devices

While amorphous Si (a-Si) is effective for passivating the crystalline Si (c-Si) base and creating carrier-selective contacts, the low lateral conductivity in the a-Si layers creates a requirement for a transparent conducting oxide (TCO) on top. Within both the a-Si and TCO layers, parasitic absorption (absorption without collected carriers) offsets the gains in open-circuit voltage V_{oc} with losses in short-circuit current density J_{sc}, amounting to 2.1 mA/cm^2 lost below 600 nm and 0.5 mA/cm^2 above 1000 nm in a 20.8%-efficient SHJ-style cell [14].

The losses in the 1.7-eV band gap a-Si can be mitigated by replacing the front CSC (intrinsic a-Si and doped a-Si) with a wide-band gap II-VI semiconductor, such as ZnS, ZnSe, or a $\mathrm{ZnS_xSe_{1-x}}$ alloy. Furthermore, if such a layer has improved lateral conductivity compared to a-Si, a TCO will not be necessary and the parasitic absorption in ITO (indium tin oxide, a TCO) can be avoided. However, given the difficulty in matching the a-Si passivation of c-Si, we include a comparison of simulated device performance with the full replacement of the front a-Si with $\mathrm{ZnS_xSe_{1-x}}$ and with the replacement of only the doped front a-Si with $\mathrm{ZnS_xSe_{1-x}}$, leaving the a-Si:i for passivation. See Fig. 1.5 for a general schematic of the proposed device design.

1.4 GaAs Photovoltaics

While silicon PV dominates the market, the high capital expense of manufacturing and the low operating margins limit the rate at which manufacturing rates can increase. Silicon photovoltaic technology cannot scale fast enough to meet the rate at which we must ramp up pv electricity generation to reach carbon neutral goals and limit global warming. The most expensive parts of silicon device manufacturing is the trichlorosilane production, the Siemens CVD process, and Czochralski growth [15]. These are essential steps to the production of a silicon wafer, and limit the

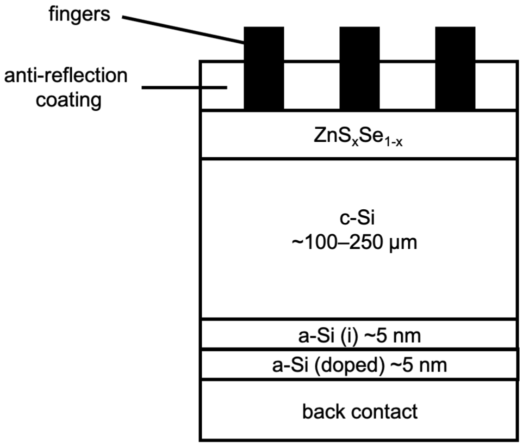

Figure 1.5: Device stack for proposed design. The doping, thickness, and mole fraction of the ZnS_xSe_{1-x} layer are chosen for optimal performance as predicted by simulation.

minimum sustainable price of a PV module. Other wafer-based technologies face similar growing pains, but semiconductors such as GaAs, with stronger absorption and higher efficiency limits than Si PV suggest viability of high-efficiency low-material-use devices based on nanowires and wafer reuse. Costs can be cut further by avoiding vacuum or epitaxial growth, which calls for alternative methods of passivation and carrier-selective contacts that can be created through liquid rather than vacuum or CVD (chemical vapor deposition) processing.

Chapter 2

DEPOSITION OF ZNS$_{\mathrm{X}}$SE$_{1-\mathrm{X}}$ BY MOLECULAR BEAM EPITAXY

2.1 Introduction to ZnS$_{\mathrm{x}}$Se$_{1-\mathrm{x}}$ Deposition

Fabrication of ZnS, ZnSe, or ZnS$_{\mathrm{x}}$Se$_{1-\mathrm{x}}$ films is possible using many techniques, including molecular beam epitaxy, thermal evaporation, metal-organic chemical vapor deposition, and chemical bath deposition [16], [17], [18]. ZnS and ZnSe both exist in zinc blende or sphalerite form and wurtzite form, both named after the ZnS minerals sphalerite and wurtzite. The zinc blende form has underlying face centered cubic symmetry and the wurtzite form underlying hexagonal symmetry. The zinc blende crystal structures of ZnS and ZnSe are the more stable forms, and transition to wurtzite above 1000°C. Prior work has shown that extrinsic doping is required for low enough resistivity to fabricate reliable Ohmic contacts, which remained a challenge in this study [19]. Extrinsic doping is achieved through non-equilibrium growth techniques, including molecular beam epitaxy and metal-organic chemical vapor deposition [20].

2.2 Fundamentals of Molecular Beam Epitaxy

Molecular beam epitaxy (MBE) is a ultrahigh vacuum deposition technique from growing thin films. Slow growth rates, typically around 1 monolayer/sec, allow for surface migration of the source molecules on the surface so that very smooth layers are obtained [21]. Shutters in front of the sources and substrate, with the slow growth rate and in-situ surface monitoring techniques, enable abrupt changes in composition. The underlying principle of MBE is analogous to steam condensing on a pot lid over boiling water. A beam flux leaves a high-temperature source, like the boiling water, and condenses when it sticks to the cooler substrate, like the water on a pot lid. The ultrahigh vacuum requirement for MBE is based on the reduction of source/contaminant interaction before reaching the substrate by the long mean free paths enabled in vacuum. The mean free path length of a gaseous molecule with diameter d at pressure p and temperature T is

$$L = \frac{kT}{\sqrt{2}\pi p d^2}. \tag{2.1}$$

Even at moderate vacuum pressures, this mean free path is on the order of tens of centimeters, so the beam nature of the source molecule flow can be maintained within the distance from the source to the substrate. The pressure of residual gas species in the vacuum chamber can still contribute to contamination of the deposited layers at a rate based on the partial pressure p_i of the residual species i, the molecular weight M_i and the residual gas temperature T as

$$w_i = p_i\sqrt{\frac{N_A}{2\pi k M_i T}} \tag{2.2}$$

where N_A is the Avogadro constant. With a goal of a 10^5 higher deposition rate for the source than the contaminant, and an assumed N_2 contaminant molecule and temperature of 300 K, residual gas pressures below 10^{-9} Pa are required.

Besides the low growth rate and low background pressures, MBE is characterized by the effusion process that governs the evaporation of most source materials. Gas sources, electron beam evaporators, pulsed laser deposition systems, etc. can be incorporated into an MBE in addition to the effusion cells. Effusion refers to a gas escaping from a container through a hole considerably smaller than the mean free path of the molecules. This small opening enables the beam nature of mass flow MBE calls for. Early investigations of evaporation rates in vacuum concluded that a liquid has a maximum evaporation rate, as there is a non-zero return flux of molecules in the gas phase [21]. In addition to evaporated molecules in the return flux returning to the condensed phase, some are also reflected back rather than condensing. Characterizing this reflected fraction as $1 - a_v$, where a_v is known as the evaporation coefficient, the evaporation rate from a condensed source is given by the Hertz-Knudsen equation:

$$\frac{dN_e}{A_e dt} = a_v(p_{eq} - p)\sqrt{\frac{N_A}{2\pi M k T}} \tag{2.3}$$

where dN_e is the number of molecules vaporating from the surface with area A_e, p_{eq} is the equilibrium pressure on the surface, and p the hydrostatic pressure [21]. Effusion cells used in MBE are designed to have a relatively large isothermal enclosure with pressure p_{eq} and with a small orifice with thin walls. In an ideal orifice design, with diameter one-tenth or less of the evaporant mean free path, the orifice and surrounding walls do not contribute significantly to scattering, adsorbiong, or desorbtion of the escaping molecules. Since the orifice does not reflect vapor molecules, $a_v = 1$, and the total effusion rate Γ_e of molecules from the effusion cell per unit time into a vacuum chamber with pressure p_v is given by

$$\Gamma_e \equiv \frac{dN_e}{dt} = A_e(p_{eq} - p_v)\sqrt{\frac{N_A}{2\pi MkT}}. \tag{2.4}$$

These relations hold for molecules evaporating from solid as well as liquid sources. This sublimation from solid to gas without an intermediate liquid state occurs at pressures below a material's triple point where the solid, liquid, and gas phases coexist. Given the reduced pressures in MBE chambers, this is commonly the phase transition occurring in effusion cells. The equilibrium pressure p_{eq} within the effusion cell cavity is given by the vapor pressure of the heated material. Governed by the Clausius-Clapeyron relation, the vapor pressure of any substance increases non-linearly with temperature. The Clausius-Clapeyron relation describes the slope of pressure with respect to temperature on a coexistence curve separating two phases of a material. The slope depends on the specific latent heat L and specific volume change of the phase transition Δv as

$$\frac{dP}{dT} = \frac{L}{T\Delta v}. \tag{2.5}$$

Of the materials involved in this study, zinc has a particularly high vapor pressure that can lead to contamination of other films being deposited in the same system [22]. For comparison, the vapor pressure of Zn is ≈1 mTorr, while Si does not reach that vapor pressure range until ≈1500°C.

2.3 Non-epitaxial Deposition

Thin films of $\mathrm{ZnS_xSe_{1-x}}$ were deposited on crystalline Si wafers in an SVT Associates molecular beam epitaxy system from compound sources of 6N ZnS and 6N ZnSe. The films were deposited in thicknesses varying from a few nanometers to a few hundred nanometers as necessary for the characterization that followed. Samples fabricated for interface and thin-film characterization purposes (rather than for a complete photovoltaic device) were prepared using the following procedure. Crystalline Si wafers were cleaned using the HF-last procedure described in [23]. This cleaning procedure was chosen for its efficacy and reproducibility compared to a standard RCA clean [23]. After this ex-situ cleaning, the c-Si substrates were immediately transferred to the MBE load lock. In the MBE growth chamber, the dyhydride layer terminating the c-Si surface was removed by heating the substrate to 300°C, soaking for 30 minutes, heating the substrate to 550°C, soaking for 20 minutes, then allowing the substrate to cool to 200°C for deposition [23]. Surface

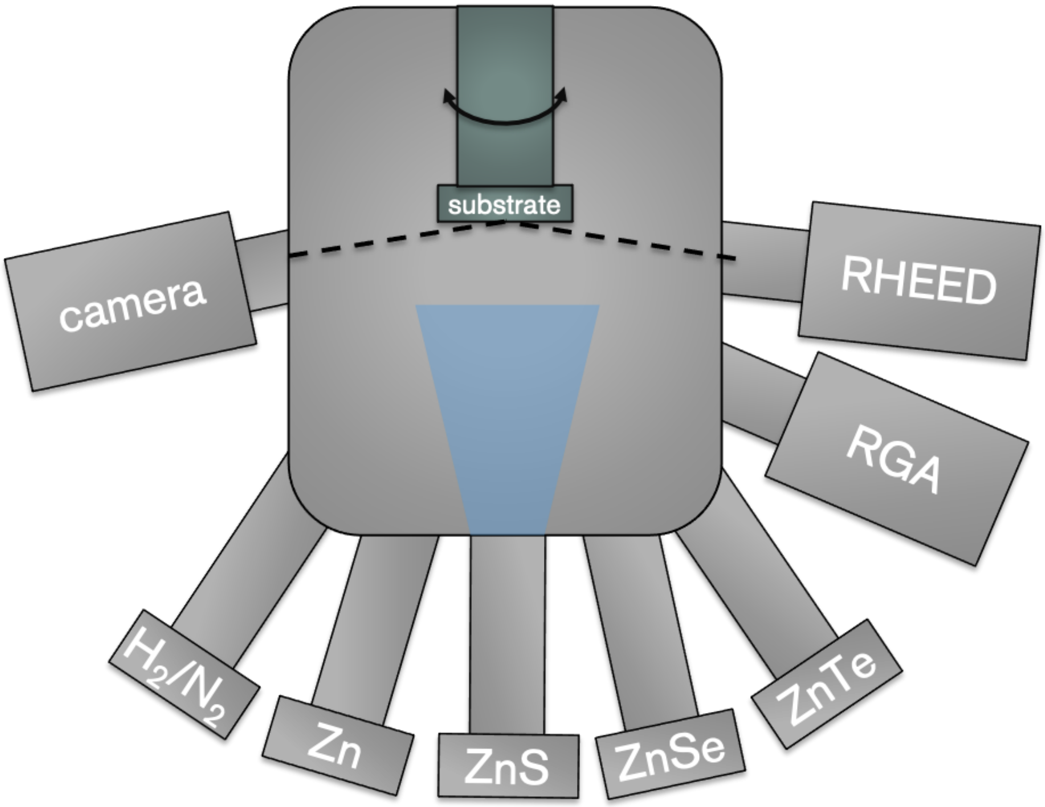

Figure 2.1: Illustration of the molecular beam epitaxy system employed in this work. Depicted are ZnS, ZnSe, and ZnTe compound source effusion cells, Zn effusion cell, RF plasma atomic hydrogen and nitrogen source (H_2 N_2), residual gas analyzer (RGA), and reflection high energy electron diffraction (RHEED) gun, and kSA 400 camera mount for capturing RHEED images. The substrate manipulator rotates along the vertical axis.

reconstruction of Si from $< 1\times1 >$ to $< 2\times1 >$ was confirmed via in-situ reflection high-energy electron diffraction (RHEED).

In order to vary the mole fraction x of the deposited $\mathrm{ZnS_xSe_{1-x}}$, the ZnS source temperature T_{ZnS} was varied between 700°C and 855°C and the ZnSe source temperature T_{ZnSe} was varied between 600°C and 750°C. The base pressure of the MBE was $\approx10^{-9}$ Torr before substrate and source heating and the background pressure during deposition was $\approx10^{-8}$ Torr. The beam fluxes from the ZnS and ZnSe sources ranged between 10^{-8} Torr and 10^{-6} Torr, depending on the source temperatures. The substrates were rotated during the deposition of thick (> 10 nm) samples to maintain uniform thickness. A Telemark 568 Multi-pocket electron beam source was used to dope select $\mathrm{ZnS_xSe_{1-x}}$ films n-type with Al during deposition.

The c-Si substrates were high-lifetime wafers, with the passivating a-Si layers as discussed in [24], [25]. The lifetime was measured on bare c-Si wafers, on c-Si with double-side a-Si passivation before and after heating and ZnS_xSe_{1-x} deposition, and on c-Si with single-side a-Si passivation and ZnS_xSe_{1-x} deposited on the opposite side to determine the effects of fabrication on passivation. The heated samples, whether or not ZnS_xSe_{1-x} was deposited, were put through the same cycle that is used for in-situ c-Si surface preparation for ZnS_xSe_{1-x} deposition: 300°C for 30 min then 550°C for 20 min, before cooling the substrate to 200°C for deposition.

Chapter 3

CHARACTERIZATION OF II-VI FILMS

3.1 Growth Rate and Film Morphology

Thickness Measurements

Thickness measurements were primarily performed using X-ray reflectivity scans, as no additional fabrication is required to define the step from film to substrate as necessary for profilometry or atomic force microscopy thickness measurements. XRR-based measurements were correlated with ellipsometry thickness fits.

X-Ray Reflectivity

Specular X-ray reflectivity is a non-destructive technique that can be used to measure thicknesses of single- or multi-layer structures, or additionally to make estimates of density and roughness of said layers. A Bragg geometry is employed where the angle between the incident X-ray and the detector (2θ) is twice the angle between the incident X-ray and the surface normal (ω), so that the portion of x-rays reflected at each interface between layers of different densities is collected at the detector. At low incident angle, a significant portion of the the x-ray is specularly reflected to the detector, creating a background signal that decays over several orders of magnitude as ω^{-4}. As the the path length difference between x-rays reflected at different interfaces coherently interfere with changing incident angle, Kiessig fringes overlay the background signal [26]. The positions of the fringe peaks are related to the layer thickness d as

$$\theta^2 = m^2 \left(\frac{\lambda}{2d}\right)^2 + \alpha_c^2 \tag{3.1}$$

where m is the fringe order, λ is the x-ray wavelength, and α_c is the critical angle below which the x-rays are totally reflected at the top surface. Low order fringes can be easily missed above the high-intensity background at the lowest angles of incidence, but α_c can be determined separately from the XRR spectra and its square can be compared to the y-intercept of the linear fit of θ^2 as a function of m^2 to confirm correct ordering.

Film Morphology

Film morphology was monitored by eye as well as XRR, scanning electron microscopy (SEM), and atomic force microscopy (AFM). SEM images were taken in a Zeiss 1550 VP field emission SEM. AFM images were taken in an Asylum AFM. HF-cleaning technique played a significant role in film uniformity. In samples deposited on substrates with a-Si layers for passivation or hole collection at the rear, a full HF-dip was not employed so as to avoid damaging the a-Si. Instead, a drop-etch was used where dilute HF or commercial buffered oxide etch were dropped via pipette on the c-Si surface. Uniform coverage with etchant was impossible due to surface tension, and sometimes the surface tension broke and the etchant spread off of the substrate. Vapor etching above concentrated HF was also evaluated as a one-side surface preparation method, but RHEED imaging showed that the drop etch more reliably removed the c-Si oxide, if not as well as a full HF dip would.

Reflection High Energy Electron Diffraction

Reflection high energy electron diffraction images are a powerful in-situ characterization tool common to MBE systems. A RHEED pattern is essentially the projection of the interaction of the reciprocal space surface lattice with the Ewald sphere of the incoming wave, and will change with the surface crystal orientation, the surface reconstruction, and the direction of the incoming wave [27].. In this work, RHEED imaging was used to evaluate surface preparation techniques and to determine the deposition type of the thin film. The incident electron beam was provided by a STAIB RH30 at 20 kV beam energy and 1.4 A filament current, and the images were captured with a kSA 400 camera and software system.

(a) RHEED image of HF-last–cleaned < 211 > c-Si

(b) RHEED image of ZnSe:Al thin film deposited on substrate shown in (a)

Figure 3.1: Reflection high-energy electron diffraction images of < 211 > c-Si before (a) and after (b) deposition of ZnSe:Al. Presence of streaks displays single-crystalline nature of the surface layer lattices.

X-Ray Diffractometry

X-ray diffractometry was used to determine the crystallinity of the deposited samples. Because the wavelength of an X-ray is of the same magnitude as the separation between lattice planes in a crystal, x-rays incident on a crystal plane at angle θ will be coherently diffracted at certain angles related to the plane separation. For a plane defined by Miller indices hkl, the peaks in diffracted X-ray are determined by Bragg's law

$$n\lambda = 2d_{hkl}\sin\theta \tag{3.2}$$

where n is an integer, λ is the wavelength of the incident beam, and d_{hkl} is the separation between adjacent hkl planes in the crystal [26]. The beam is coherently diffracted at the same angle at which it is incident on the plane, so if the plane is parallel to the surface normal of the crystal, the diffracted beam will also be oriented at angle θ from the surface. Single crystal X-ray diffractometers general consist of a stationary X-ray source and a goniometer with independently controlled detector optics and sample stage. The sample orientation is defined to be 0° when the surface is parallel to the incident X-ray, and similarly, the detector is at 0° when it is directly in line with the X-ray. Thus, for planes parallel to the sample surface, the coherently diffracted X-ray produced at incident angle θ can be detected at detector angle 2θ. For clarity, the sample orientation is often referred to by the angle ω, and the detector by angle 2θ. In the Bragg-Bretano geometry, there is no offset between ω and θ, and in the corresponding 2θ-ω scan, the sample and detector are rotated simultaneously to detect diffraction peaks from planes parallel to the surface. In the case of off-cut substrates, as were used in this study, where the substrate surface is not parallel to crystal orientation, an ω offset δ can be defined so that the detector angle $2\theta = 2(\omega - \delta)$ and peaks corresponding to the named substrate orientation can be observed. For crystals with underlying cubic symmetry, which is the case for all crystals of interest in this study, the lattice plane spacing d_{hkl} is related to the Miller indices and lattice constant a by

$$d = \frac{a}{\sqrt{h^2 + k^2 + l^2}}. \tag{3.3}$$

The symmetry of some lattice planes leads to destructive rather than constructive interference at the angle defined in (3.2), and the diffraction peak is forbidden. The scattering intensity is related to the squared modulus of the structure factor F_{hkl} for crystals, which is defined as

$$F_{hkl} = \sum_{j=1}^{N} f_j \mathrm{e}^{-2\pi i (hx_j + ky_j + lz_j)} \tag{3.4}$$

where f_j is the element dependent scattering factor of the j-th atom and x_j, y_j, and z_j are the positional coordinates of the j-th atom. For a diamond cubic lattice, such as is present in crystalline silicon, the structure factor evaluates to 0 when h, k, and l are of mixed parity and

$$F_{hkl} = \begin{cases} 8f, & h+k+l = 4N \\ 4(1 \pm i)f, & h+k+l = 2N+1 \\ 0, & h+k+l = 4N+2 \end{cases} \tag{3.5}$$

otherwise where N is an integer. This means that for single diffraction, silicon only has allowed peaks when Miller indices are all even and sum to a multiple of 4 or are all odd. So for <001> Si, within the angular range available, we only expect to see a peak at the <004> location in the Bragg-Bretano geometry. However, the <002> peak forbidden under single diffraction conditions is allowed under diffraction from multiple planes, known as Umweganregung [28]. This peak is quite narrow and is visible in XRD scans when well-aligned to the <001> lattice planes. For zinc blende structures, the structure factor evaluates to 0 for mixed parity and

$$F_{hkl} = \begin{cases} 4(f_A + f_B), & h+k+l = 4N \\ 4(f_A \pm i f_B), & h+k+l = 2N+1 \\ 4(f_A - f_B), & h+k+l = 4N+2 \end{cases} \tag{3.6}$$

otherwise, where f_A and f_B refer to the scattering factors for elements A and B present in the structure. Thus certain peaks forbidden in Si, such as the <002> peak, are allowed in zinc blende materials but suppressed depending on how similar the scattering factors are between the constituent elements. Near 8 keV energy, corresponding to the Cu $k_1\alpha$ wavelength present in the XRD system used in this study, the zinc, sulfur, and selenium scattering factors are 28, 16, and 33.

X-ray diffraction spectra were collected in a PANalytical X'Pert Pro MRD with a Cu $k_1\alpha$ incident X-ray with a hybrid monochromator in the incident beam path and a triple-axis monochromator in the diffracted beam path. For consistency, $2\theta - \omega$ scans taken on off-cut substrates were aligned to the <001> lattice place rather than

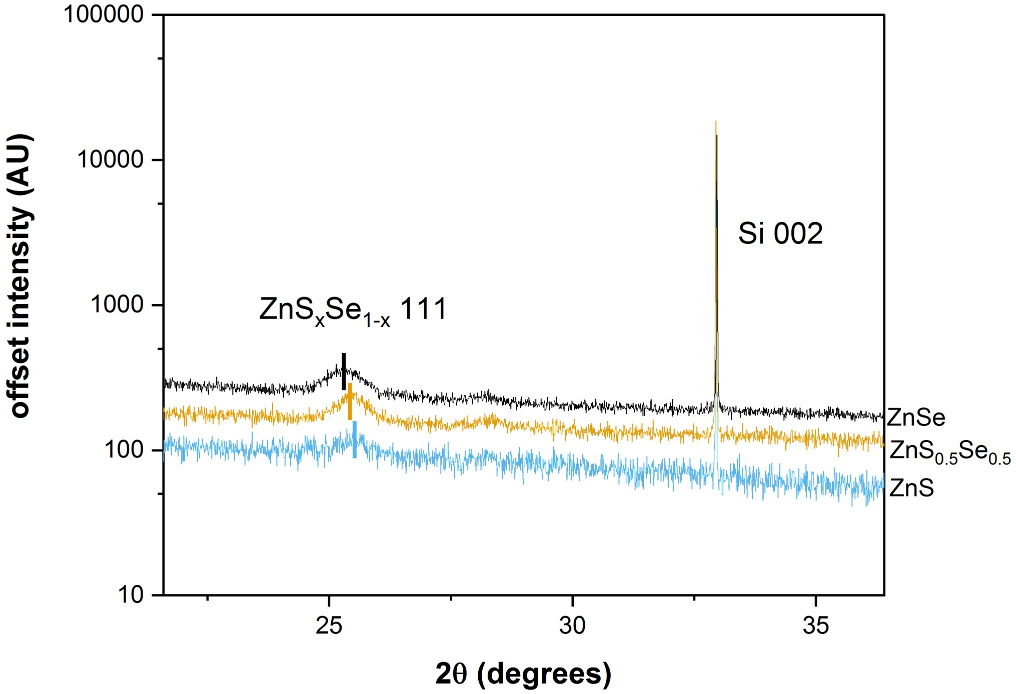

Figure 3.2: Diffracted x-ray intensity as a function of detector angle from $2\theta - \omega$ scan taken on ZnS_xSe_{1-x} films in the Bragg-Bretano geometry, aligned to the offcut Si -<001> substrate. The ZnS_xSe_{1-x} <111> peak is visible, shifting from lower angle to higher angle with increasing mole fraction. The sharp multiple diffraction Si <002> peak is also visible.

the surface normal. This means that when non-epitaxial films were deposited, they are not parallel to the substrate lattice but rather the substrate surface, which offsets the 2θ location of their diffraction peaks. The shifting position of the dominant <111> peak with mole fraction composition is shown in Fig. 3.2

3.2 Stoichiometry

Stoichiometry of samples was determined via a combination of methods as they were incorporated into other characterization methods. Samples imaged via transmission electron microscopy (TEM) and scanning electron microscopy (SEM) were also characterized by energy-dispersive X-ray spectroscopy (EDS). EDS characterizes X-rays emitted from a sample when an electron excited by the imaging electron beam (in the case of TEM and SEM) returns to a lower energy shell. The stoichiometry of samples characterized via x-ray photoelectron spectroscopy (XPS) was determined from the ratio of peak areas of the relevant species core level lines. The peak areas were calculated from the difference between raw data intensity and the modeled background, rather than the integrated peak intensity from modeled component peaks. This area calculation was chosen as the best representation of the number of contributing electrons. While modeled component peaks are important for determining peak position and binding energy shifts, and relative concentrations of different bonding states within the same core level region, the mathematical models of peak shapes do not always do a good job of matching the raw data, and their integrated areas can vary significantly with different choice in shape. In either case, when relative atomic concentrations are determined using XPS peak areas, relative sensitivity factors specific to the XPS system are used to calibrate the areas.

3.3 Electrical Properties

Resistivity Measurements

A standard four-point probe set up was used to quickly measure thin film resistivity. Four equally spaced probes are brought into contact with the sample in a straight line, such that the spacing s is much greater than the film thickness t and much less than the sample diameter D. A current is applied across the outer two probes and a voltage measured across the inner two probes. If the aforementioned assumptions of sample and probe geometry are valid, the sheet resistance in $\Omega/\Box$ is given by

$$\rho_{\Box}(\Omega/\Box) = \frac{\pi}{\ln 2}\frac{V}{I}. \tag{3.7}$$

For samples of known thickness t, the sheet resistivity can be determined as

$$\rho_{\mathrm{cm}}(\Omega - \mathrm{cm}) = \frac{\pi}{\ln 2}\frac{V}{I}t. \tag{3.8}$$

The four-point probe set had imperfect horizontal alignment (tips not sufficiently level with each other) and thinness of the layers of interest made sheet resistance measurements in this technique particularly tricky. The I-V Software used to take the measurements had a convenient DC measurement mode where the software would alert when a current threshold was reached as the probes were lowered. Many measurements were taken in one of two extremes. At a lower contact threshold (10^{-6}), all four probes would not actually be touching the sample. At a higher contact threshold (5×10^{-6}-1×10^{-5}), the probes would punch through and measure the substrate rather than the film. If the probes do not make Ohmic contact with the $\mathrm{ZnS_xSe_{1-x}}$ film, the contact threshold will not be met unless transport is through the substrate. In the films that were measurable, sheet resistivities ≈1 Ω-cm were higher than expected based on earlier samples produced in the same MBE system under similar conditions, which achieved $\rho = 0.002$ Ω-cm for ZnS films and $\rho = 0.001$ Ω-cm for ZnSe films [29].

Hall Measurements

Moving charge carriers experience a force perpendicular to an applied magnetic field. When such a field is applied in the direction of a surface normal of a semiconductor, charges accumulate on one side of the sample, creating a voltage across the semiconductor. This effect is known as the Hall effect and the resulting voltage as the Hall voltage. For a sample in the x-y plane, with positive current through the semiconductor in the x-direction and positive magnetic field in the z-direction, both electrons and holes drift in the negative y-direction, thus the potential difference across the sample is in the y direction. As charge carriers accumulate, the potential difference defense and electric field that opposes the Lorentz force created by the magnetic field, and a steady state is reached when the electric force from charge accumulation balances the magnetic force in the opposite direction. The potential difference at steady state is measured as the Hall voltage. With voltage referenced on the positive y-direction face of the sample edge, and the Hall voltage measured on the negative y-direction side, Hall voltage is negative for n-type semiconductors where the predominant charge carriers are electrons and positive for p-type semiconductors with holes as the primary charge carriers.

Carrier Concentration

At steady state, $\boldsymbol{F} = q\left(\boldsymbol{E} + \boldsymbol{v} \times \boldsymbol{B}\right) = 0$, so $E_y = v_x B_z$. Where w is the width of the sample in the y-direction, the electric field is related to the Hall voltage by $E_y = -\frac{V_H}{w}$. The (known) current in the x direction is related to the charge carrier velocity by

$$I_x = q[C] \times v_x[cm/s] \times n[1/cm^3] \times tw[cm^2] = qv_x ntw$$

where q is the charge of the electron or hole, n is the carrier density, and t is the sample thickness so that $t \times w$ is the cross-sectional area in the direction of current (x). Thus, the charge carrier volume density is given by

$$n = \frac{I_x B_z}{qtw|V_H|}$$

and the charge carrier sheet density n_s by

$$n_s = \frac{IB}{q|V_H|}.$$

Hall measurements were performed in a LakeShore FastHall Measurement system with high-resistance contact measurement capabilities. This was important as electrical contact with the ZnS_xSe_{1-x} layers was quite difficult. Of the samples on which Hall measurements were possible, the contact resistances were on the order of 1 MΩ. The best sample showed carrier concentration of 3×10^{16} cm^{-3} as fabricated. Secondary ion mass spectrometry measurements showed Al concentration of 10^{19} cm^{-3}, suggesting that the donors were well below fully activated. In an attempt to increase the donor activation, samples were annealed for 2–3 hours at 400°C in a furnace under forming gas. This raised the carrier concentration of the best sample to 10^{18} cm^{-3}, still below the desired level for the intended photovoltaic device. In an effort to raise the Al concentration of the CSC, the e-beam current was increased during ZnS deposition, but the resulting samples were metallic, with much higher Al concentration than intended.

Microwave Photoconductivity Decay Lifetime Measurements

Looking forward to full-device fabrication, a deposition order that did not compromise the passivating effect of a-Si on c-Si was sought. Specifically, the high temperatures (up to 550°C) involved in the default ZnS_xSe_{1-x} deposition preparation was expected to significantly degrade the lifetime of the passivated c-Si. However, as shown in Fig. 3.3, there was not a large difference in the milliseconds-long lifetimes of a double-side a-Si passivated c-Si substrate before and after heating to 300°C for 30 min and then 550°C for 20 min. The effective lifetime of carriers in a single-side a-Si passivated c-Si wafer was also measured with and without ZnS_xSe_{1-x} thin films at high, low, and no aluminum doping. While there is an increase in lifetime of 5 μs between front-side-bare c-Si and $ZnS{:}n^+$ coated c-Si, the effect is not sufficient to consider ZnS_xSe_{1-x} deposited in this method as “passivating.” As such, we also simulated devices where the passivating thin intrinsic a-Si layer is left at both the front and back of the c-Si, and a CSC is completed with ZnS_xSe_{1-x}:n on front and a-Si:p on back.

Table 3.1: Substrate details

Substrate	Layers
S1	40 nm a-Si:i/150 μm <211> c-Si:p/40 nm a-Si:i
S4	5 nm a-Si:i/c-Si/5 nm a-Si:i/5 nm a-Si:p+
S2	c-Si/5 nm a-Si:i/5 nm a-Si:p+

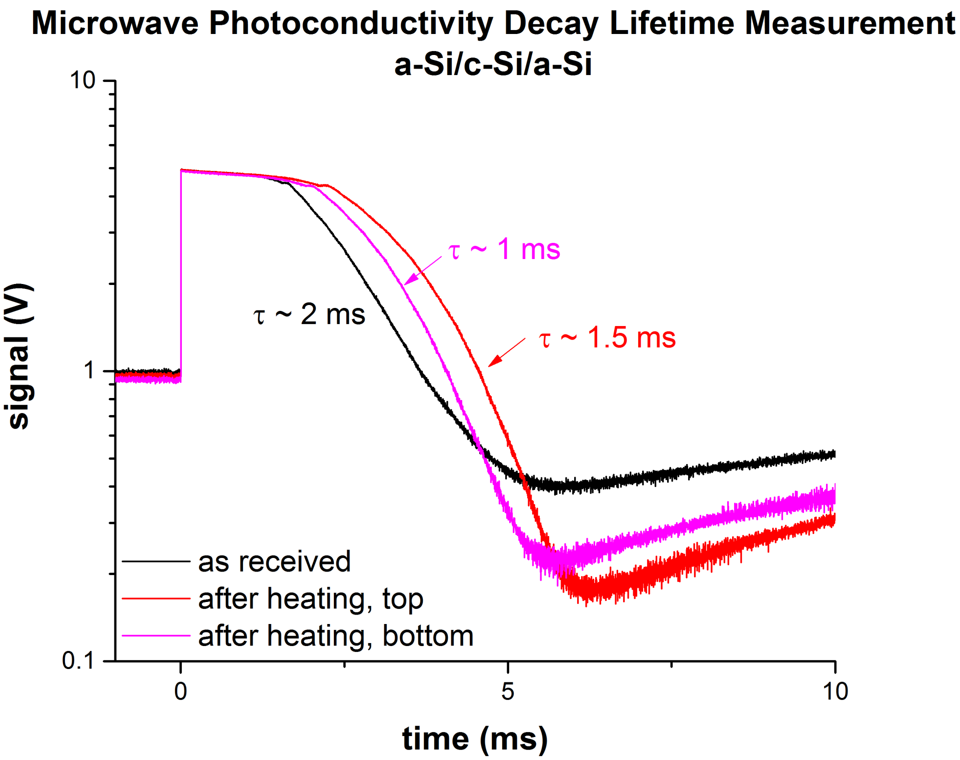

Figure 3.3: Microwave photoconductivity decay of double-side a-Si–passivated c-Si wafers before (lifetime τ ~2 ms) and after heating (τ ~1 ms).

Microwave photoconductivity measurements were conducted in a Freiberg MDP Spot system. Free carriers are generated with above-band-gap laser excitation on a sample that is coupled to a waveguide cavity. The microwave absorption, monitored with an IQ (in-phase and quadrature components) detector, is a function of photoconductivity [30]. The exponential decay in photoconductivity after a rectangular excitation pulse correlates with the effective lifetime of excited carriers [31]. Knowledge of the sample geometry allows one to place bounds on the surface recombination velocity at the $\mathrm{ZnS_xSe_{1-x}}$-Si interface.

The effective lifetime measured via microwave photoconductivity measurements were used to estimate the surface recombination velocity of the top surface, informing device simulation. The surface recombination velocity is related to the effective lifetime τ_{eff}, bulk lifetime τ_b, cell width W, and minority carrier diffusivity D as

$$S = \sqrt{D\left(\frac{1}{\tau_{eff}} - \frac{1}{\tau_{bulk}}\right)} \tan\left[\frac{W}{2}\sqrt{\frac{1}{D}\left(\frac{1}{\tau_{eff} - \tau_b}\right)}\right]. \tag{3.9}$$

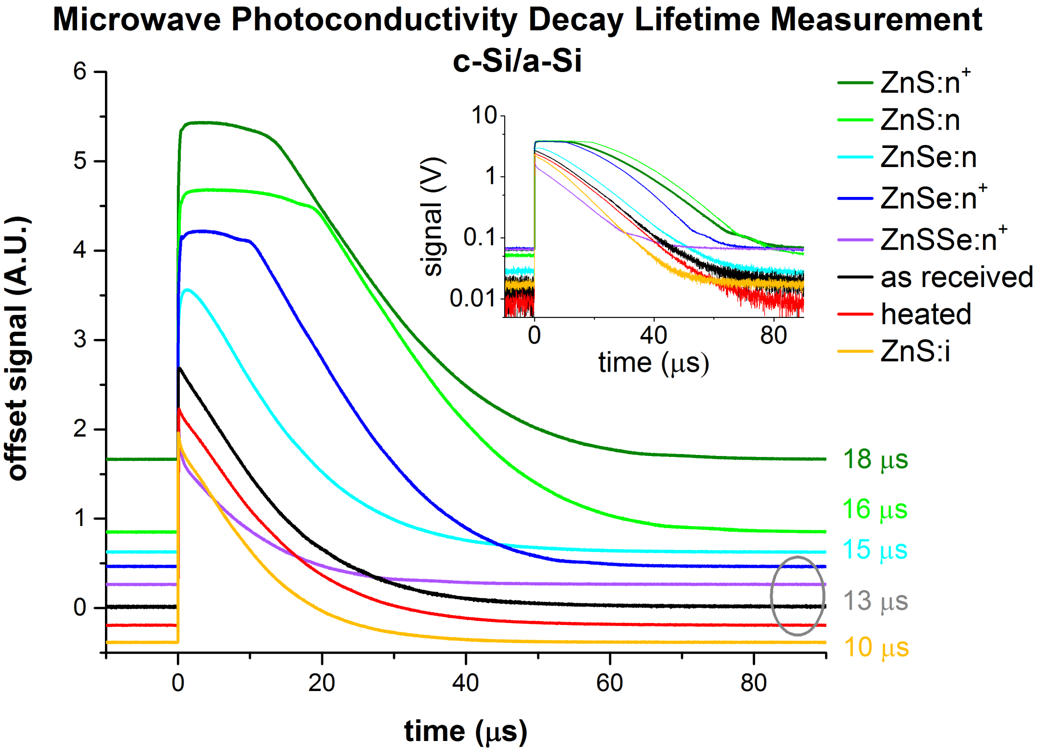

Figure 3.4: Microwave photoconductivity decay of back-side a-Si–passivated c-Si wafers with and without ZnS_xSe_{1-x} thin films on top. Inset shows signal voltage on a log scale.

Table 3.2: Lifetime measurements

Device	**Substrate**	**Max sub temp (°C)**	**Source temp (°C)**	**Lifetime (μs)**
S1	See Table 3.1	RT	–	2300
S4	See Table 3.1	RT	–	400
S4	S4	200	–	340
S4/100 nm Ag	S4	RT	–	280
S2	See Table 3.1	RT	–	25
S2	S2	200	–	25
S2/100 nm Ag	S2	RT	–	16
ZnS:Al 20 min	S4	200	855	29
ZnS:Al 20 min	S2	200	855	61
ZnS:Al 10 min	S4	200	855	62
ZnS:Al 10 min	S2	200	855	390
ZnS:Al 60 min	S2	200	750	42
ZnS:Al 60 min	S4	200	750	146
ZnS:Al 60 min	S2	RT	750	54
ZnS:Al 60 min	S4	RT	750	60
ZnS:Al 20 min	S2	150	855	197
ZnS:Al 20 min	S4	150	855	192

Chapter 4

BAND ENERGETICS OF PHOTOVOLTAIC CONTACTS

4.1 Experimental Determination of Energy Band Alignment

Valence Band Offset

The energy-band offset between the $\mathrm{ZnS_xSe_{1-x}}$ and Si conduction bands has an important influence on device performance and was calculated using the Kraut method [32]. The Kraut method measures the valence band offset at the interface between two materials, as shown in (4.1).

$$\Delta E_{VB} = \left(E_{CL}^{\mathrm{film}} - E_{VBM}^{\mathrm{film}}\right)_{\mathrm{b}} - \left(E_{CL}^{\mathrm{sub}} - E_{VBM}^{\mathrm{sub}}\right)_{\mathrm{b}} - \Delta E_{CL,\mathrm{i}}. \tag{4.1}$$

Measured by x-ray photoelectron spectroscopy (XPS), E_{CL} is the core-level binding energy peak position and E_{VBM} is the binding energy of the valence band maximum (VBM). The VBM of the bulk samples was measured as the intersection of linear fits of the lowest binding energy electrons and the background. For each valence band offset measurement, the binding energy of one core level represented in the film material ($E_{CL,\mathrm{film}}$: Zn 2p 3/2 or Se 3d 5/2) and the binding energy of one core level represented in the substrate material ($E_{CL,\mathrm{Si}}$: Si 2p 3/2) is chosen. The XPS spectra of electrons ejected from the valence band of the substrate and film in an interfacial sample overlap, so the offset between valence band maxima is difficult to measure directly. Instead, the binding energy of VBM electrons in bulk samples of $\mathrm{ZnS_xSe_{1-x}}$ and bare Si substrates are measured. Since the difference in binding energy between electrons in a particular core level and electrons at the valence band maximum, i.e. $(E_{CL} - E_{VBM})_{\mathrm{bulk}}$, is constant for a given material, the shift of binding energies of core level electrons at the interface ($E_{CL,i}$) from their position in the bulk ($E_{CL,\mathrm{film}}$ or $E_{CL,\mathrm{Si}}$) is the same as the shift between VBM binding energies at the interface from those in the bulk. Thus the bulk VBM binding energies can be corrected to those at the interface, and the valence band offset can be found, as visualized in Fig 4.1. Knowledge of the band gap of each material allows one to calculate the conduction band offset. The band offsets are reported in the energy-band scale (greater number ⇒ greater potential energy) while the core-level peak and valence band maximum positions are reported in the binding-energy scale (greater number ⇒ less potential energy). The XPS measurements were performed in a Kratos Analytical AXIS Ultra DLD. The band gaps of the $\mathrm{ZnS_xSe_{1-x}}$ films were

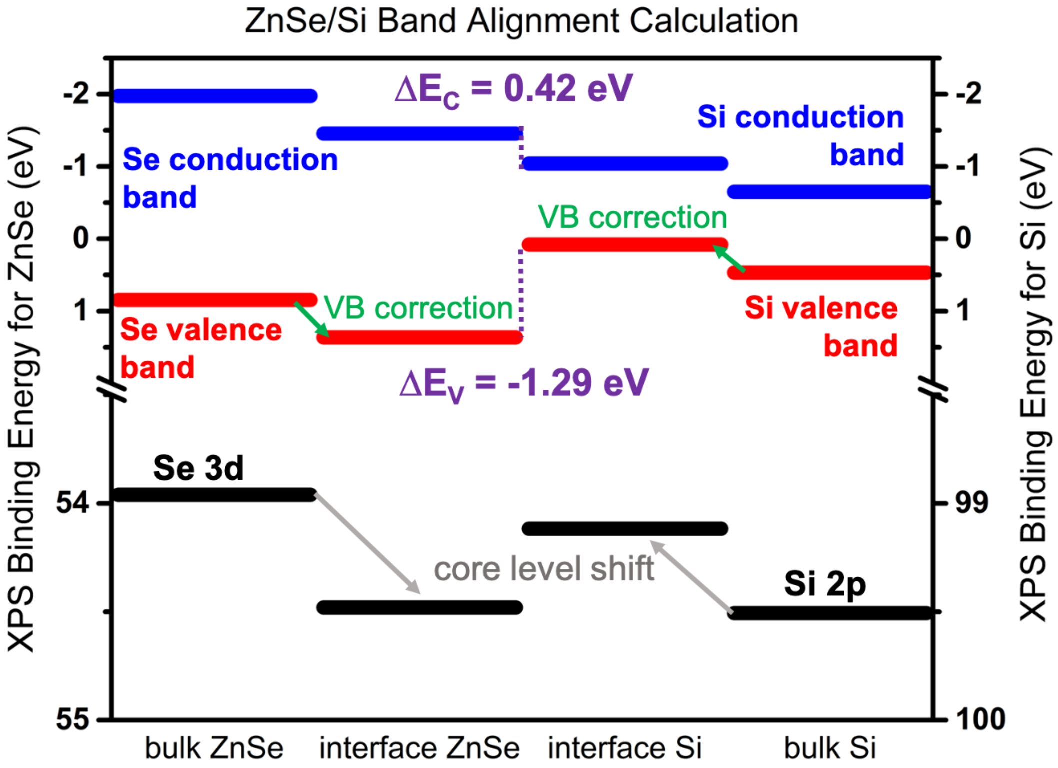

Figure 4.1: The offset in valence band energy at the interface between two materials, given in the energy band scale, is calculated from the valence band maximum position of the materials in bulk, given in the binding energy scale, and shift in VBM position at the interface, inferred from the shift in core level peaks relative to those in the bulk.

measured with spectroscopic ellipsometry. The band gaps of the ZnS_xSe_{1-x} films were linearly interpolated from the band gaps of ZnS and ZnSe as a function of mole fraction x.

Core-Level Electron Energy

X-ray photoelectron spectra taken for core-level electron analysis (Al Kα, 10 mA, 15 kV) were analyzed with Casa XPS software using the provided relative sensitivity factors for Kratos systems. Shirley-type backgrounds were used for background subtraction for all core level spectra. Core level peaks were fit with the modified symmetric Voigt-like lineshape, defined as LA(1.53, 243) in Casa XPS [33]. The first parameter α defines the spread of the Lorentzian tail and the second parameter m defines the width of the convoluted Gaussian.

The binding-energy position of the Si 2p 3/2 peak was used as the substrate core-level reference peak. The doublet peak separation between the Si 2p 3/2 and Si 2p 1/2 contributions is small, so both peaks were modelled to determine the position of the more intense, lower-binding-energy 3/2 peak. The 1/2 peak was constrained to a binding energy 0.6 eV above the Si 2p 3/2 peak, full-width at half-max (FWHM) equal to the FWHM of the Si 2p 3/2, and an area half the size of the Si 2p 3/2 peak. The Zn 2p 3/2, S 2p 3/2, and Se 3d 5/2 peaks positions were each used as the film reference core levels for separate measurements of the band offsets for the $\mathrm{ZnS_xSe_{1-x}}$ spectra, as appropriate for mole fraction composition. The Zn 2p peak has a large doublet separation (≈23 eV), so only the Zn 2p 3/2 peak was modeled to find the position. The Se 3d region was modeled with pairs of doublets where the Se 3d 3/2 contributions were constrained to equal FWHM and two-thirds the area of their respective Se 3d 5/2 photoelectron peak and 0.85 eV separation. The S 2p region was modeled with pairs of doublets with the same FWHM and area constraints as the Si 2p regions. On thin and Se-rich samples, fitting the S 2p peaks posed a particular challenge as the region overlaps with that of the Se 3p core level and Si 2s core level plasmon-loss peaks. Because these higher-intensity peaks greatly reduced the precision and accuracy of the S 2p 3/2 peak position measurement, the S-referenced measurements were not included in the conduction band offset calculation presented in 4.6. The S-referenced measurements are included in 4.3.

For ease in identifying chemical states of peak components, spectra were calibrated to the valence band maximum (set to binding energy 0 eV) when this spectrum was available. This is done not as a charging correction, but to make more transparent the peak-to-peak spacing (such as Ga 3d to Ga 2p bulk peaks) for more informed fitting. For a bare GaAs substrate (sputter-cleaned in situ), the Ga 3d 5/2 peak is located at 18.8 eV binding energy, the As 3d 5/2 peak at 40.7 eV, and the Ga 2p 3/2 peak at 1116.9 eV. With the exception of the GaAs with native oxide sample, in subsequent samples, the peaks nearest these positions are the highest intensity, lowest full-width half max components, consistent with bulk GaAs signal. In the native oxide sample, the $\mathrm{Ga^{3+}}$ oxide state dominates. Previous studies have shown that whenever oxygen is present in GaAs spectra, some $\mathrm{Ga_2O}$ ($\mathrm{Ga^{1+}}$ oxide) contribution is present, and the chemical shift for Ga 2p 3/2 peaks from Ga-As bonds to $\mathrm{Ga^{1+}}$ bonds is 0.55 eV [34], [35]. Thus, in all GaAs samples with O 1s signal (i.e. all except the bare GaAs), we include Ga^{2p+} contributions, constrained to 0.55 eV above the Ga-As peak in the Ga 2p range. GaAs native oxide is additionally composed of $\mathrm{Ga_2O_3}$ ($\mathrm{Ga^{3+}}$), $\mathrm{As_2O_3}$ ($\mathrm{As^{3+}}$), and $\mathrm{As_2O_5}$ ($\mathrm{As^{5+}}$), and the absence of $\mathrm{As^{5+}}$ component is use to distinguish

Ga^{3+} components from other Ga bonding states.

The Ga 2p spectra does not include the Ga 2p 1/2 component, as the doublet spacing is wide and the 2p 3/2 and 2p 1/2 peaks do not overlap. The As 3d spectra is fit only with doublet pairs, with separation constrained to 0.69 eV and 3d 3/2 area constrained to 2/3 of the paired 3d 5/2 component for each chemical state. Following previous work, the Ga 3d spectra is fit with a doublet pair for the bulk contribution (with the same area constraints as the As 3d region), but single Ga 3d peaks for the surface peaks. The energies referenced are for the Ga 3d 5/2 peak. The As-Ga, As^{3+}, and As^{5+} core-level electrons are separated by about 2.5 eV and 1.5 eV, located near 40.5 eV, 44 eV, and 45.5 eV respectively. We find that the raw data for the As 3d bulk signal (from about 40 eV to 43 eV binding energy) is not well fit by a single doublet pair, even for an in-situ oxygen-free sputter-cleaned surface, as shown in Fig. 4.2a. A single pair underfits the spectra on the high-binding-energy side, though is well accounted for by an additional pair located 0.45 eV above the primary GaAs-ascribed peaks (Fig. 4.2b). There is no additional chemical state to which an additional peak pair should correspond. Thus, it is proposed that there is a significant failure of the background and line shape models to accurately reflect the physics in this region. In the absence of an appropriate background and line shape, a compromise is made for consistency, where the second bulk peak pair is always included as a way to model the apparent asymmetry of the As 3d core level peaks.

Valence Band Energy

Photoelectron spectra collected near zero binding energy were collected with X-ray (XPS) and ultraviolet (UPS) excitation. The valence band maximum was determined as the intersection of two linear fits to spectra: one fit through the low signal background (lower binding energy) and one fit through the signal decay.

Conduction Band Offset

The conduction band offset of a film with respect a substrate is related to the valence band offset by the energy band gaps of the film and substrate, and shown in (4.2), where a positive conduction band offset implies the film conduction band is higher (potential energy of electron) than the substrate conduction band.

$$\Delta E_{CB} = \Delta E_{VB} + E_G^{\text{film}} - E_G^{\text{sub}} \tag{4.2}$$

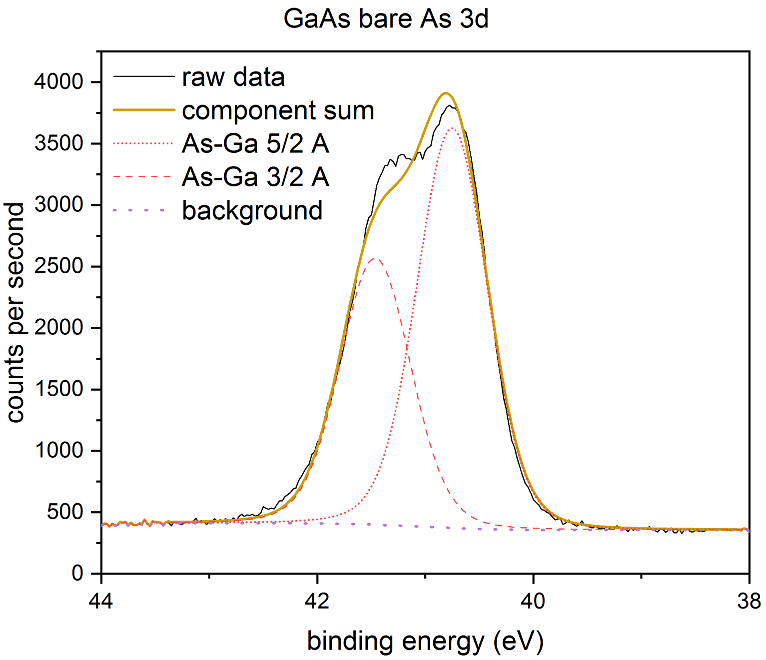

(a) Fitting with single doublet pair

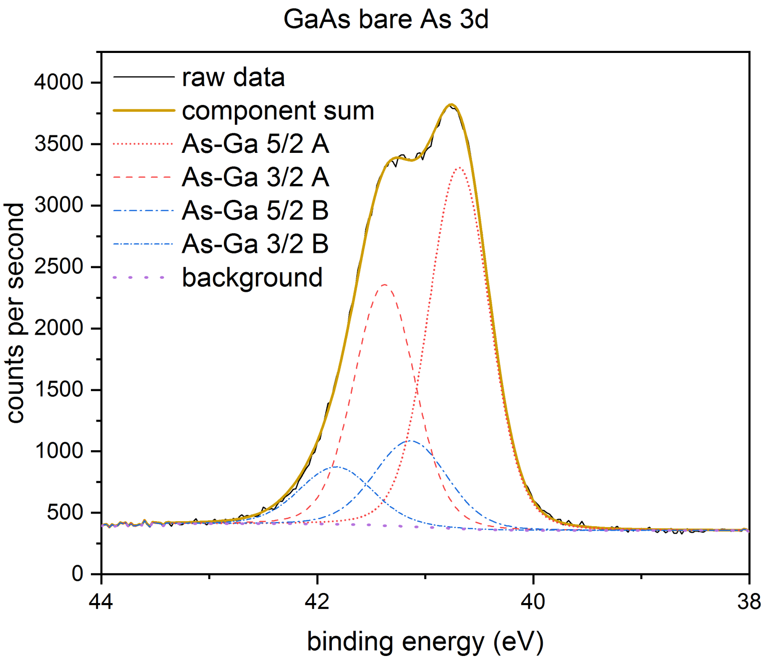

(b) Fitting with supplementary doublet pair

Figure 4.2: High-resolution XPS spectra of As 3d region on bare GaAs wafer (sputtered in-situ) showing (a) high binding-energy underfit with a single doublet pair and (b) asymmetry accounted for by second doublet pair at 0.45 eV higher binding energy.

Limitations

Depending on the conducting nature of the sample of interest, charging of samples during XPS may occur. If negative charge is not refilled at a sufficiently high rate to maintain charge neutrality at the surface, positive charge accumulates, leading the shift of all core-level peaks towards higher binding energy values. This effect can be mitigated with the use of an in-situ charge neutralizer gun, although overcompensation may occur. It is also common practice to "calibrate" sets of spectra to the location of the C 1s peak, as this signal is nearly always present due to the accumulation of adventitious carbon. However, the nature of the adventitious carbon is not always well known, nor is it necessarily chemically consistent between samples [36]. There is also no consensus at what energy this ever-present C 1s peak occurs, so different sets of spectra are "calibrated" to different C 1s binding energies, further diminishing the usefulness of this reference peak. Other studies may calibrate their spectra to a known core level peak of an element common to the samples of interest, such as setting As 3d 5/2 to 41.1 eV binding energy in GaAs samples, although this still relies on the knowledge (or often assumption) that the chemical state of the subject peak is consistent between samples. When we are specifically interested in the binding energy shift of a core level peak at the interface of a sample, the assumption is inappropriate.

In the case of the thin films on semiconducting substrates studied in this work, no significant charging was observed when the sample was mounted on the sample holder with a copper bar across the top. With sufficient surface contact, the bar grounded the sample at the top, while the sample holder itself was assumed to be in electrical contact with the rear of the sample.

There remains a purpose in calibrating the binding energy scale of the obtained photoelectron spectra. Due to the difference in work function between the sample surface and the detector, electrons are accelerated through the analyzer, changing their nominal kinetic energy at the surface from $E_{KE} = h\nu - E_{BE}$ to $E_{KE} = h\nu - E_{BE} - \phi_s$ once ejected from the surface to $E_{KE} = h\nu - E_{BE} - \phi_s + \phi_s - \phi_a = E_{KE} = h\nu - E_{BE} - \phi_a$ when the electrons hit the detector (where ϕ_s and ϕ_a are the surface and analyzer work functions, respectively). Given that all relevant parts of this system are electrically connected and share a common ground (sample, sample holder, analyzer), all Fermi levels (binding energy = 0 eV) should be equilibrated, including all other samples on the sample holder. We cannot directly measure the mid-gap Fermi level of semiconductor samples of interest, but we can observe the Fermi level step down in metallic samples on the same sample holder whose spectra are collected under identical X-ray and analyzer conditions. Then, all spectra can be adjusted by the binding energy offset from 0 eV for the reference metallic sample. When we cannot rule out subtle changes in the potentials through which electrons pass before detection between runs on different days (especially when venting and subsequent realignment/recalibration of the system occurs in the interim), we can gain confidence in the value of comparison of binding energies across different samples by referencing the system Fermi level to 0 eV binding energy.

With the knowledge that there is an option to calibrate spectra for direct comparison between samples, one can also notice that for valence band offset measurements, such calibration is irrelevant. Since the calculation relies on the binding energy *separation* between different core level peaks, and the high-resolution spectra from which the core level binding energies are fit would be subject to the same shift in binding energy during calibration, the presence or absence of calibration does not change the valence band offset measurement. However, when multiple chemical states of the same element are present in the sample (for instance, Ga-As, Ga^{1+} oxide, and Ga^{3+} oxide at a GaAs surface), binding energy calibration can make the identification of the chemical state easier. The binding energy separation remains the most reliable way to compare spectra between samples, especially when details of the data acquisition and calibration are unknown.

4.2 Band Alignment Results

ZnS_xSe_{1-x} on Si

Band offsets of ZnS_xSe_{1-x} on c-Si were found to vary linearly between $\Delta E_{CB} = 0.7\ eV$ for x = 0 (ZnSe) to $\Delta E_{CB} = 1.1\ eV$ for x = 1 (ZnS). The offsets were calculated with each of the constituent elements of the ZnS_xSe_{1-x} as reference, and with as deposited and sputter cleaned surfaces. Because of the time and distance involved in transporting the samples from the MBE system in which they were made to the XPS system in which they were measured, the samples were sputtered cleaned with an argon ion gun to remove any layers contaminated during transport. The calculated band offsets were consistent between the as deposited and cleaned surfaces, suggesting that any adventitious carbon or oxygen contamination did not affect the measurements. However, the offsets calculated with the S 2p peak as reference often deviated from the Zn 2p or Se 3d referenced scans. Figure 4.3 shows

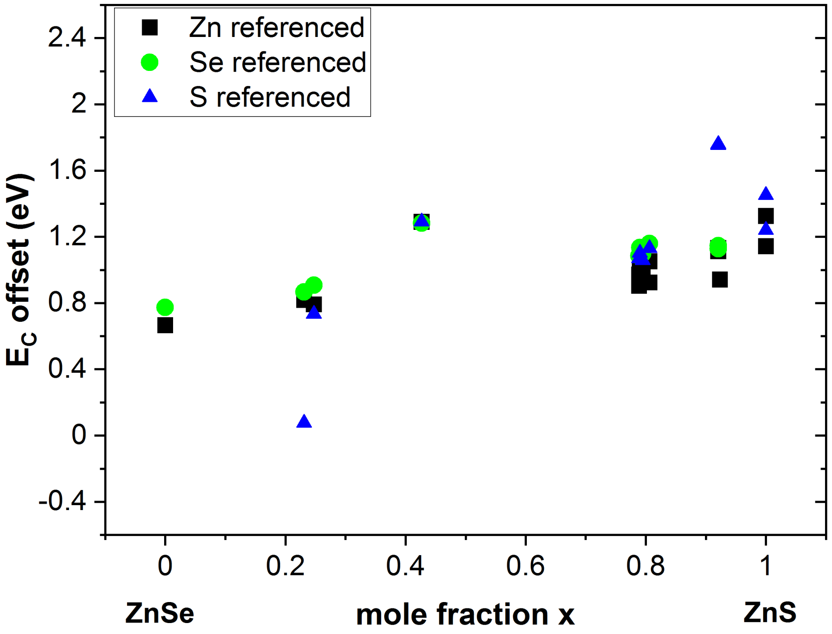

Figure 4.3: ZnS_xSe_{1-x}/Si conduction band offsets as a function of mole fraction, x. Measurements referenced to the Zn 2p 3/2 peak are shown with black squares, to the Se 3d 5/2 peak with green circles, and to the S 2p 3/2 peak with blue triangles.

the offset measurements referenced to Zn, Se, and S with different symbols. The inconsistency between the Zn/Se and S referenced data is due to the overlap of the S 2p core level peaks with the Se 3s peaks and a Si 2s plasmon loss peak. The S 2p region for bulk ZnS_xSe_{1-x} samples with varying mole fraction is shown in Fig. 4.4. The relative intensity of the Se 3s doublet compared to the S 2p doublet increases with increasing Se fraction from top to bottom. The signal from the Si 2s plasmon loss peak is even more intense and broand than the Se 3s contribution, as shown by the S 2p region for the ZnS/Si interfactial sample in Fig. 4.5.

As the Se 3s signal is added to the mixture of photoelectron signal with increasing Se content, the S 2p doublet fitting becomes less certain. These overlaps of Se and Si contributions in S core level spectra also exists in even lower intensity sulfur contributions, so there is not a way to avoid this signal mixing for sulfur-reference measurements. Thus, the S-referenced values are not included in the linear fitting of the conduction band offsets as a function of mole fraction. Additionally, the x≈0.4 measurement appears as an outlier from the linear trend. The interfacial sample for this composition had particularly weak Si 2p signal, as it is believed this lack

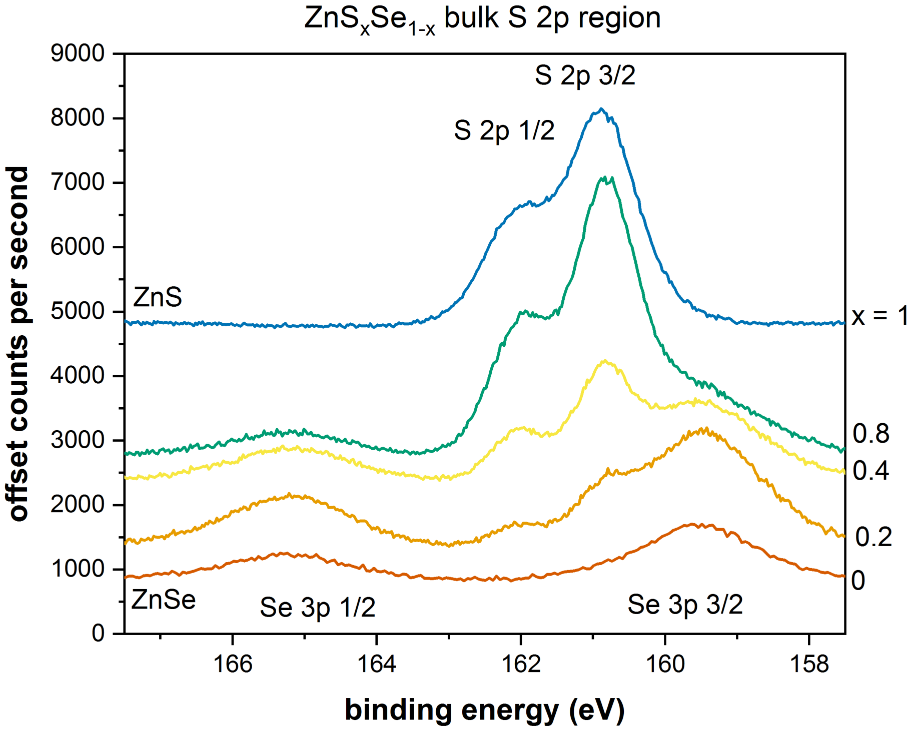

Figure 4.4: Offset x-ray photoelectron spectra in the S 2p core level region (158 eV to 168 eV binding energy) of ZnS_xSe_{1-x} with mole fraction x = 0 (ZnSe, red), 0.2 (orange), 0.4 (yellow), 0.8 (green), 1 and (blue, ZnS) from bottom to top. The Se 3p doublet contributes signal to the S 2p region even when there is no sulfur content in the sample (ZnSe). The S 2p doublet pair lies between the Se 3s doublet pair.

of precision contributed to the offset of each of the Zn, Se, and S referenced band offset measurements at this value. However, the inclusion or exclusion of this data point does not significantly affect the linear fit of the trend shown in Fig. 4.6.

CSCs on GaAs

With the same method as for ZnS_xSe_{1-x} CSC's on Si, several carrier selective contacts were screened for epitaxy-free transport layers on GaAs nanowire cells. The band offsets of SnO_2, perylene, C60, NiO, tris(4-carbazoyl-9-ylphenyl)amine (TCTA), and poly(triaryl amine) (PTAA) on GaAs with and without sulfide and 1-dodecanethiol self-assembled monolayer (SAM) passivation are included in Fig. 4.8. Through this study, SnO_2 and PTAA were identified as good candidates for electron-selective layers, and NiO and TCTA were identified as good candidates for hole-selective layers.

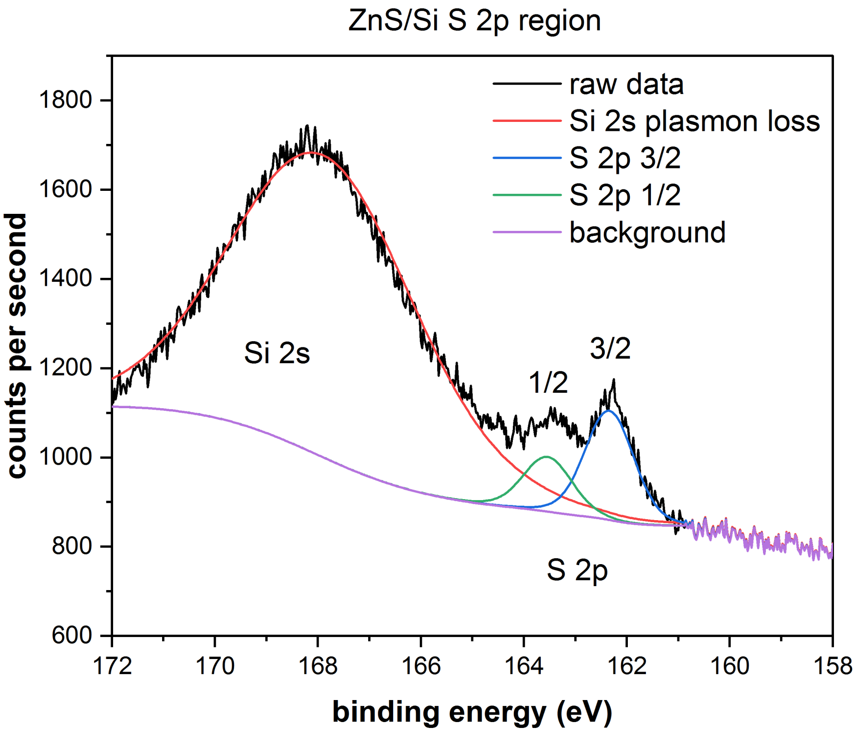

Figure 4.5: X-ray photoelectron spectrum of ZnS in the S 2p core level region, with raw data in black, component peaks from right to left corresponding to a S 2p 3/2 (blue), S 2p 1/2 (green), and Si 2s plasmon loss (red) peaks, and background in purple.

4.3 III-V Semiconductor Passivation Characterization

GaAs has two stable oxide states: Ga_2O_3 (Ga^{3+}) and Ga_2O (Ga^{1+}). The Ga^{3+} oxide dominates in GaAs with a native oxide and is indicative of poor surface passivation (see Fig 4.10). The Ga^{1+} oxide can remain present after passivation, while Ga^{3+} oxide contribution correlates with a poor photoluminescence. Thus, the nature of oxides at a GaAs surface can be used to evaluate a surface treatment for passivation efficacy, where a higher binding energy Ga^{3+} signal implies poor passivation, while lower binding energy Ga^{1+} peak implies a well-passivated surface. This analysis was performed for several surface treatments, with a focus on the chemical states distinguishable from the Ga 2p spectra, supplemented by analysis of the more bulk-sensitive Ga 3d spectra as well as the As 3d region. A comparison of the Ga 2p spectra for a GaAs surface with native oxide and GaAs surface with n-heterocyclic carbene (NHC), dithiothreitol, octanethiol, and sulfide passivation is shown in Fig. 4.9. For the thiol-passivated samples (OT and DTT), there are

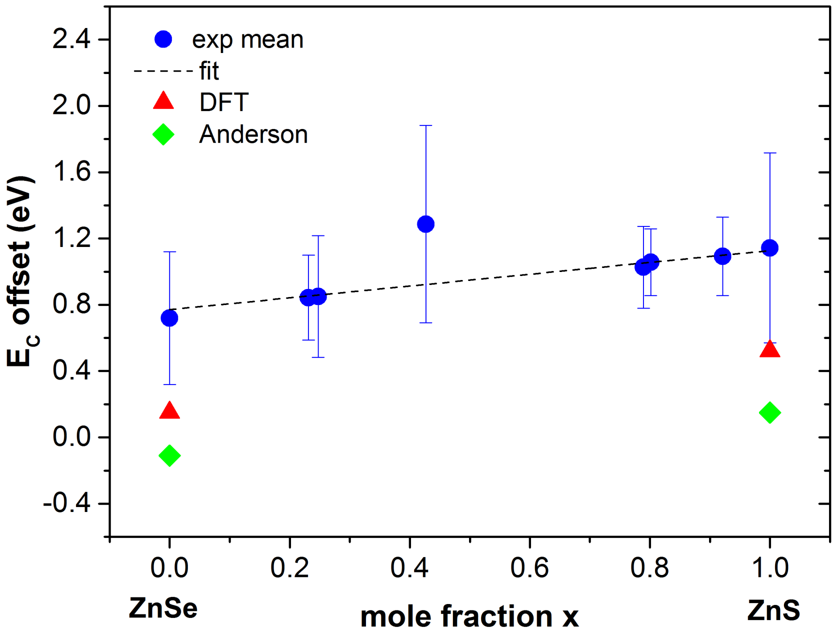

Figure 4.6: Conduction band offset at the ZnS_xSe_{1-x}/Si interface vs mole fraction. Experimental measurement through XPS (blue circles), with the best linear fit (- - -). The density functional theory based predictions (red triangles) is based on [37]. The Anderson model predictions (green diamonds) is based on [38].

additional Ga chemical state peaks evident in both the Ga 2p (Figs. 4.13 and 4.12) and Ga 3d regions at a lower binding energy than the bulk peak. These are assigned to the Ga-thiol bonding state. In the NHC-passivated GaAs spectra (Fig. 4.11), the third spectral component in both the Ga 2p and Ga 3d regions is at a similar binding energy to the Ga^{3+} contributions identified in the native oxide. However, there is no other contribution representative of the Ga-NHC bonds we know must be present, and there is no discernable As^{5+} signal that correlates with a native oxide. Thus we assign the highest binding energy Ga 2p and Ga 3d peaks to Ga-NHC bonds in NHC-passivated samples. In the sulfide passivated samples, there is O 1s signal present, but relatively little, and no evidence of an oxide in the As 3d region. Thus we assume there is very little oxidation of the surface, even a Ga^{1+} oxide, and while there is a small Ga^{1+} contribution fitted (see Fig. 4.14), no oxide contribution is added in the Ga 3d region. Tables 4.1, 4.2, and 4.3 summarize the core level peak spacings in binding energy electron volts.

To further understand the bonding of the DTT and NHC self-assembled monolayers

Table 4.1: Bulk GaAs peak core level binding energy separations in eV.

Surface	**VBM to Ga 3d**	**Ga 3d to As 3d**	**Ga 3d to Ga 2p**
bare	18.8	21.9	1098.1
native oxide	18.8	21.9	1098.1
octanethiol	18.6	21.9	1098.5
dithiothreitol	18.7	21.9	1098.5
n-heterocyclic carbene	18.6	21.9	1098.3
sulfide	18.5	21.9	1098.1

Table 4.2: Ga 3d core level binding energy chemical shifts in eV

Surface	**Ga-As to Ga^{1+}**	**Ga-As to surface state**	**surface state**
native oxide	0.7	1.6	Ga^{3+}
octanethiol	0.8	-1.0	OT
dithiothreitol	1.1	-0.9	DTT
n-heterocyclic carbene	0.6	1.7	NHC
sulfide	–	0.6	S

Table 4.3: Ga 2p core level binding energy chemical shifts in eV

Surface	**Ga-As to surface state**	**surface state**
native oxide	1.4	Ga^{3+}
octanethiol	-0.3	OT
dithiothreitol	-0.1	DTT
n-heterocyclic carbene	1.35	NHC
sulfide	0.3	S

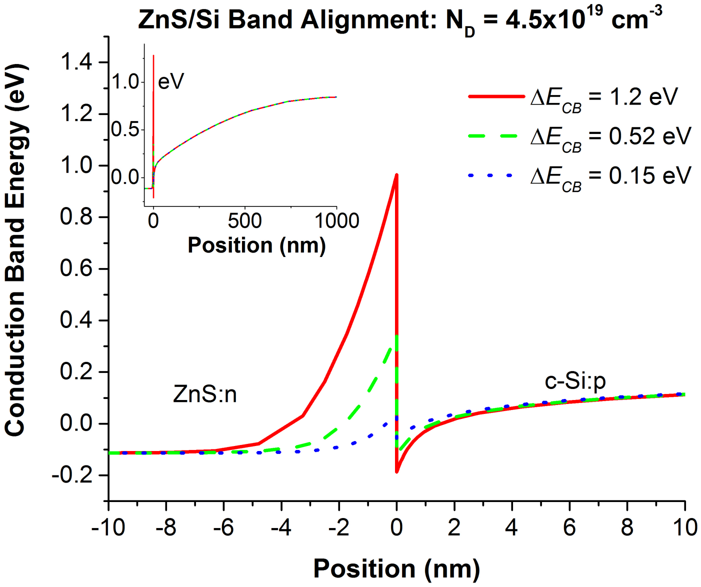

(a) subcaption

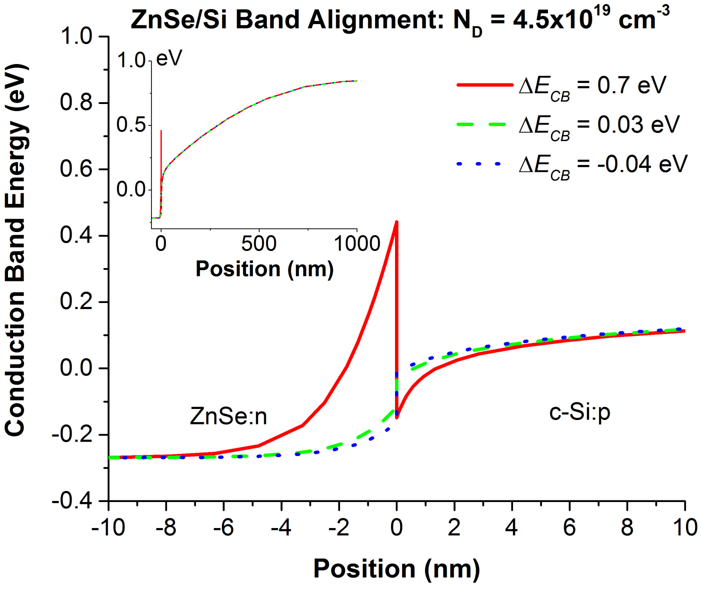

(b) subcaption

Figure 4.7: Conduction band diagrams near ZnS_xSe_{1-x}:n/c-Si:p interfaces for x = 1 (a) and x = 0 (b). Bands are shown assuming different conduction band offsets. From top to bottom, band for experimentally determined offset in solid red line, for DFT-based offset in dashed green line, and for Anderson model offset in dotted blue line. Insets show conduction band out to 1000 nm absorber depth.

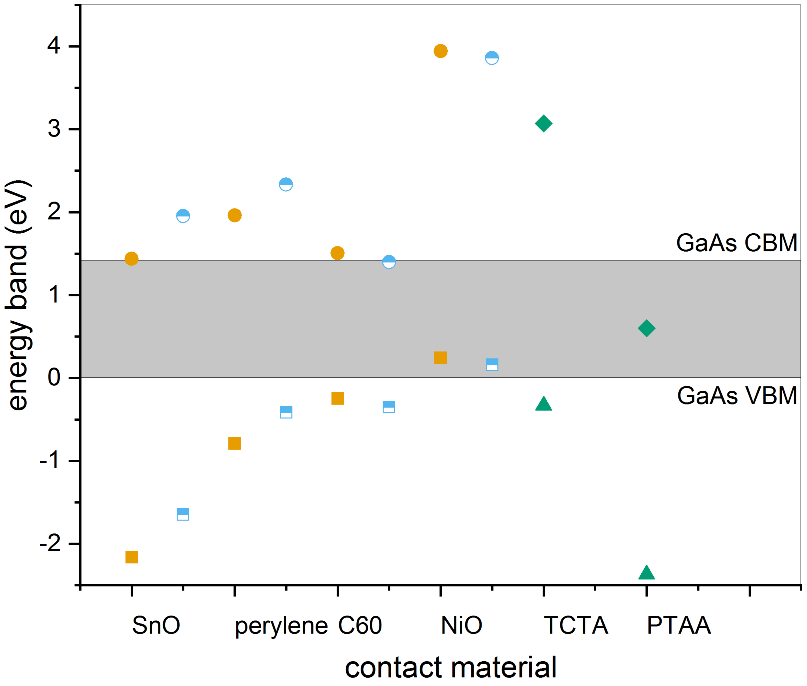

Figure 4.8: Band alignment of potential carrier-selective contacts on GaAs, relative to the GaAs valence band maximum at 0 eV. Measurements of the SnO_2, perylene, C60, and NiOx layers on sulfide-passivated GaAs are shown in filled orange symbols and on SAM-passivated GaAs in half-filled blue symbols. Circles correspond to the conduction band minimum and squares to teh valence band minima. TCTA and PTAA band edges directly on GaAs are shown in filled green symbols, with diamonds for the conduction band minima and triangles for the valence band maxima.

with the GaAs surface, structure relaxation calculations were completed using the Quantum Espresso DFT code with the BURAI frontend and the Materials Cloud Standard solid-state efficiency pseudopotentials. Since the variation in XPS spectra between surface treatments is primarily evident in Ga core levels rather than As, we infer that the passivating layers bond mainly to gallium atoms. We hypothesize that given the similarity in XPS spectra for DTT (two sulfurs) and OT (one sulfur), the two DTT sulfurs are in the same bonds as the OT sulfur, namely both bonded to the GaAs surface. The unbonded forms of DTT and OT are shown in Fig. 4.15.

The initial placement of the DTT was further informed by the closeness in the distance between thiolate groups, 3.9 Å, to the 4.0 Å gallium nearest-neighbor distance on the GaAs <100> surface: sulfurs were placed above nearest-neighbor

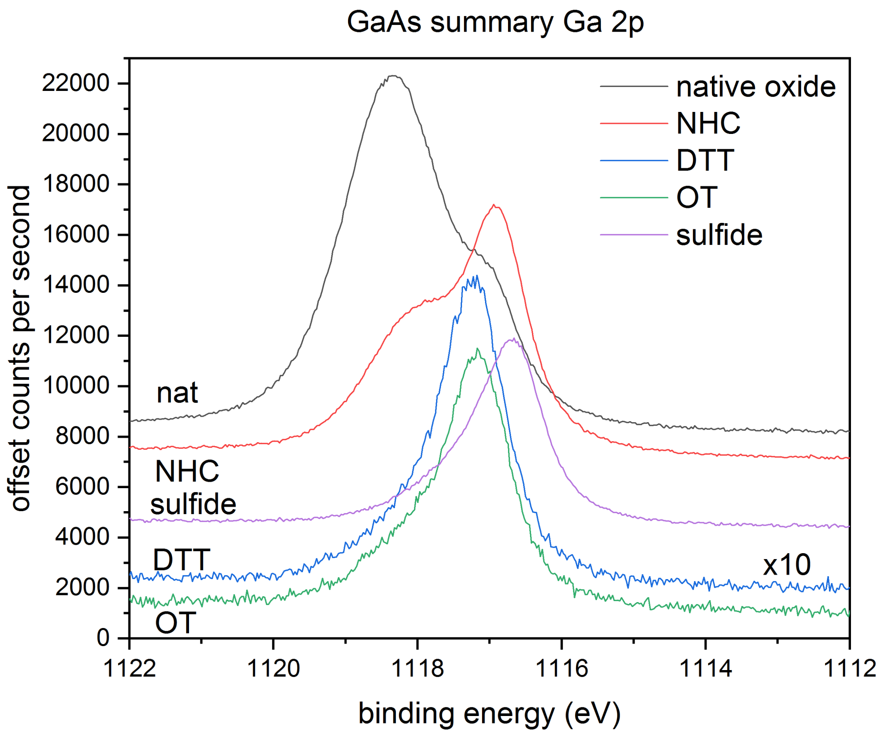

Figure 4.9: Offset Ga 2p XPS spectra of GaAs with, from top to bottom, native oxide (gray), NHC (red), sulfide (purple), DTT (blue), and OT (green) passivation layers.

gallium sites. For the NHC-GaAs calculations, the size of the molecule implies only one carbene can fit per pair of nearest-neighbor gallium atoms, so the initial carbene position was between the nearest neighbors. To allow the GaAs surface to relax, we modelled two layers of the <100>-GaAs surface and fixed the bottom layer to the unperturbed bulk structure. Illustrations of the relaxed structures created in CrystalMaker are included in Fig. 4.16.

The calculations show that the sulfur atoms of the DTT coordinate two gallium atoms each and the carbon backbone lies along the valleys of the surface. For NHC, we find that the carbene strongly breaks the symmetry between the surface gallium atoms. We can characterize the degree of symmetry breaking in each case by comparing the near-neighbor distances between gallium atoms on the surface. For the unperturbed lattice, this is 4.00 Å. For DTT, we find the two nearest neighbors at distances of 4.01 Å and 4.17 Å, deviations of 0.25% and 4%. For NHC the nearest neighbors are 2.59 Å and 4.35 Å away, perturbations of 35% and 9%, respectively.

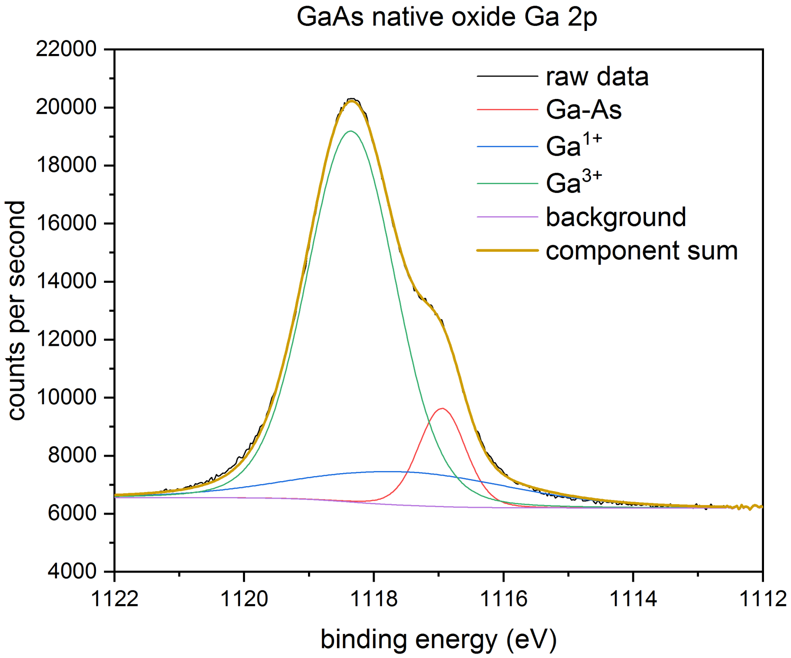

Figure 4.10: Ga 2p XPS of GaAs with native oxide.

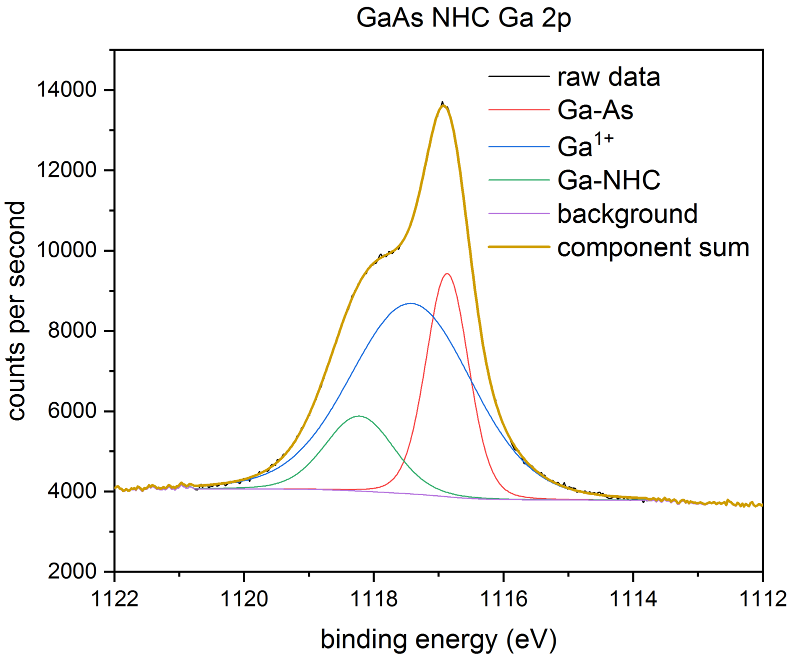

Figure 4.11: Ga 2p XPS of GaAs with NHC passivation.

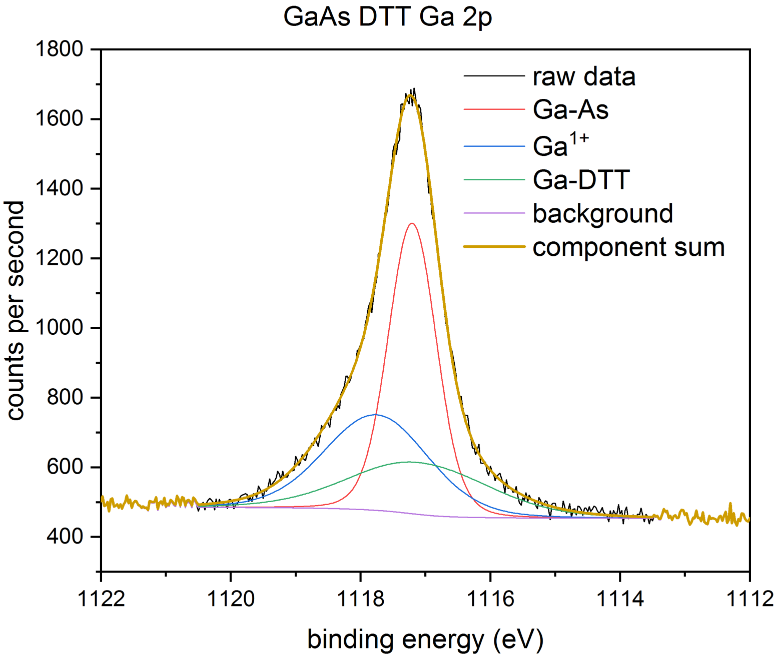

Figure 4.12: Ga 2p XPS of GaAs with DTT passivation.

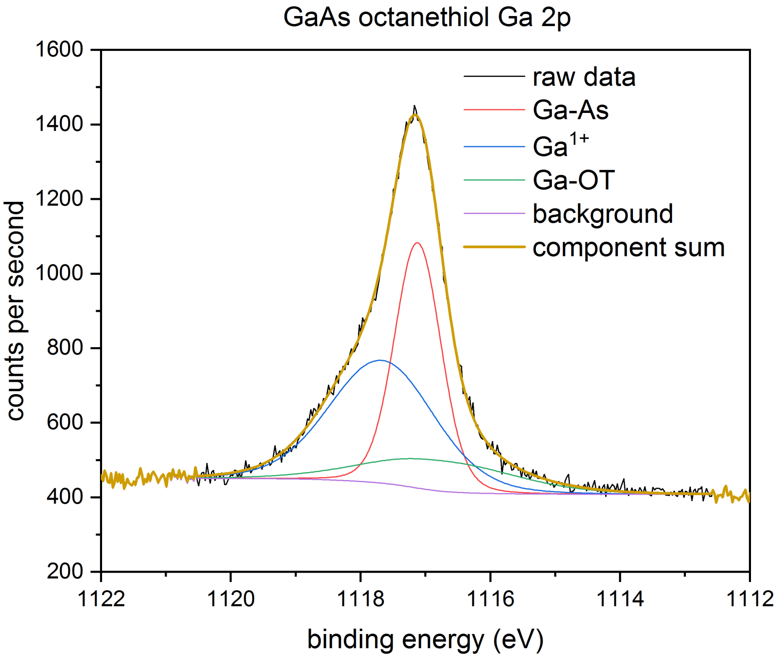

Figure 4.13: Ga 2p XPS of GaAs with OT passivation.

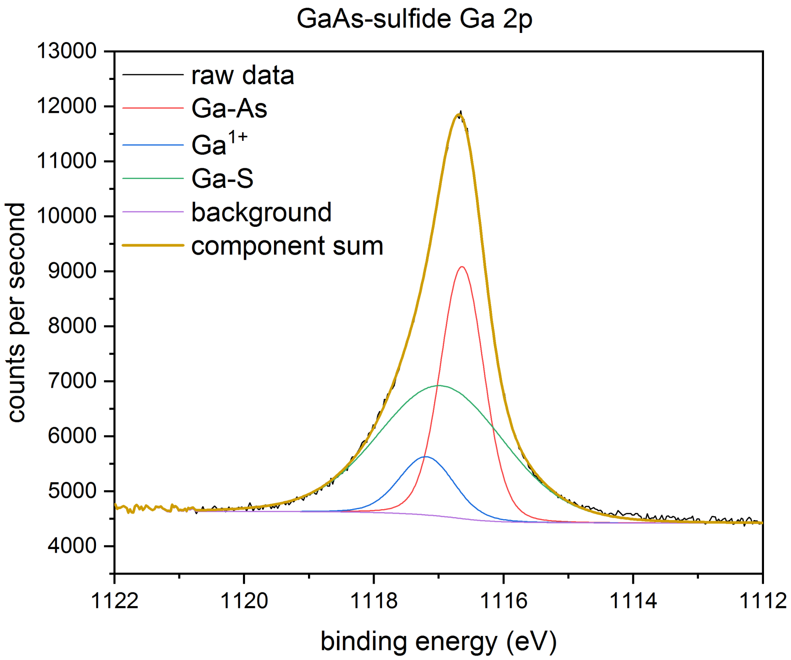

Figure 4.14: Ga 2p XPS of GaAs with sulfide passivation.

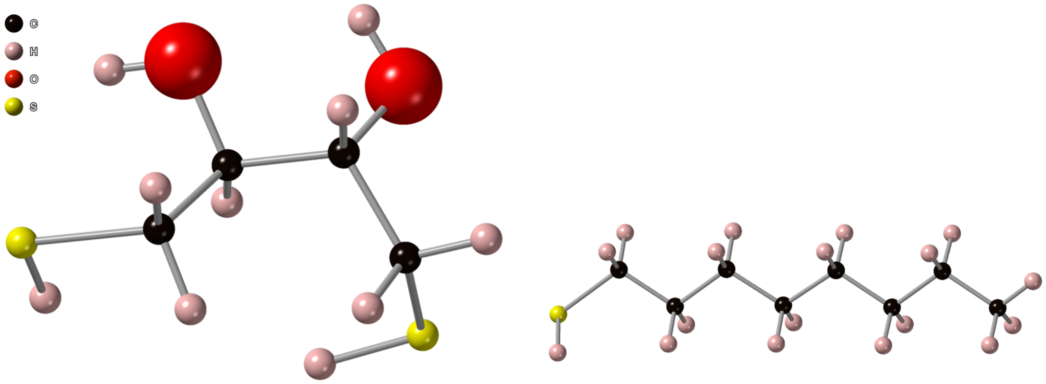

(a) Dithiothreitol (DTT)

(b) Octanethiol (OT)

Figure 4.15: Ball-and-stick models of (a) DTT and (b) OT molecules. The colored balls correspond to the relevant atoms as follows: black = carbon, pink = hydrogen, red = oxygen, yellow = sulfur.

The large perturbation of the NHC treated surface qualitatively correlates with the unique Ga 2p spectra compared to native oxide, sputter cleaned, sulfide, and thiol passivated surfaces.

Despite the differences in bonding states between the different passivation lay-

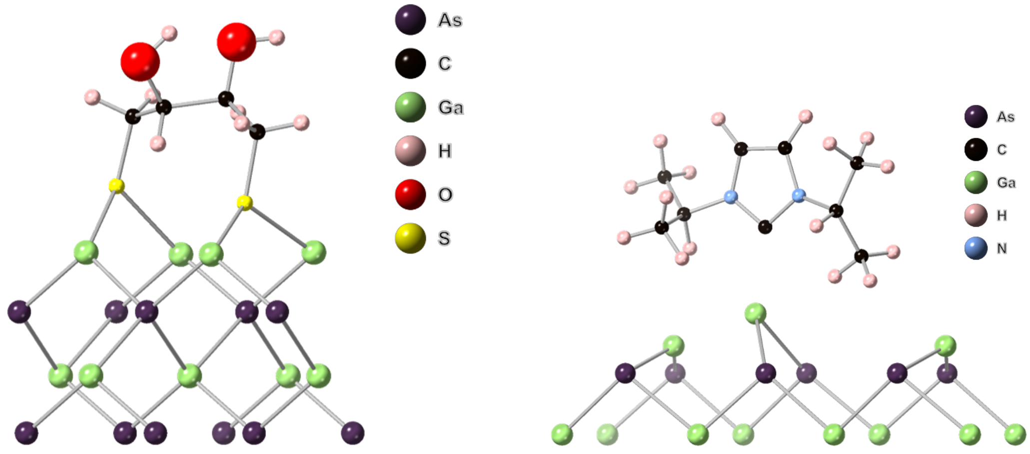

(a) DTT on GaAs

(b) NHC on GaAs

Figure 4.16: DTF calculated orientation of (a) DTT and (b) NHC on GaAs and resulting GaAs surface atom displacement. The colored balls correspond to the relevant atoms as follows: purple = arsenic, black = carbon, green = gallium, pink = hydrogen, red = oxygen, yellow = sulfur, blue = nitrogen. (a) The DTT bonds to the GaAs surface at the sulfur atoms on either end of the molecule. (b) The middle Ga atom of the displayed unit cell at the GaAs/NHC interface is significantly displaced by the bonding to the carbene center.

ers, we can confirm that the determined non-oxide bonding states are consistent with well-passivated samples. We characterize the minority carrier recombination properties of the passivated GaAs surfaces using time-resolved photoluminescence measurements (TRPL). Different passivation schemes were applied to an n-type GaAs substrate with a 50 nm GaInP confinement layer and 50 nm GaInP passivation layer, which is etched away before the other passivation layers are added. The stability of the passivation layers was studied by heating the samples on a hotplate in air for 5 min at increasing temperatures. Carrier lifetimes and surface recombination velocities were determined similarly to the method reported in Chapter 4. The carrier lifetime and surface recombination velocity for each passivation layer as a function of hotplate temperature are reported in Figs. 4.17 and 4.18.

Notably, the carrier lifetimes with tested passivation layers, sulfide, octanethiol, dithiothreitol, and n-heterocyclic carbene are all longer than the naive radiative lifetime of ≈150 ns at room temperature. This indicates the presence of photon recycling in all samples at room-temperature. The carrier lifetime of the intact double-heterojunction with GaInP sample is included as reference, and implies a photon-recycling factor of at least 6.5. The inorganic sulfide passivates best at room

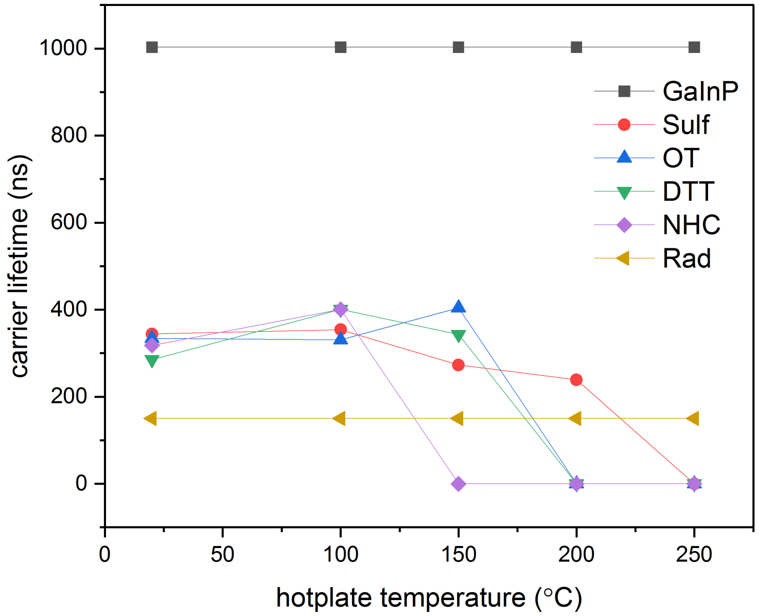

Figure 4.17: TRPL-determined carrier lifetimes of GaAs passivated with GaInP on the rear and GaInP (grey square), sulfide (red circle), octanethiol (blue triangle △), dithiothreitol (green triangle ▽), and n-heterocyclic carbene (purple diamond) after 5 minutes on a hotplate at the reported temperatures. The radiative lifetime (no photon recycling) is shown for reference at 150 ns in gold triangles ◃.

temperature of the tested layers, achieving an SRV of 240 cm/s. The octanethiol layer is the best of the organic layers at room temperature, with an SRV of 250 cm/s. Passivation with DTT and NHC improve with hotplate temperature upto 100°C, and with OT upto 150°C. All organic chemical passivants reach a minimum SRV of 200 cm/s, corresponding to a photon recycling factor of 2.7. To our knowledge, this is the first report of photon recycling in chemically-passivated GaAs films. Passivation fails with increasing temperature for each layer, starting with NHC at 100°C, the thiols at 150°C, and the sulfide above 200°C.

4.4 Conclusions

X-ray photoelectron spectroscopy proves to be a powerful tool for evaluating the appropriateness of different materials for carrier-selective contacts and passivation layers on Si and GaAs. Experimentally determined band offsets vary significantly from those predicted theoretically, and this difference has an impact on application. As such, experimentally determined band offsets should be used in the design of

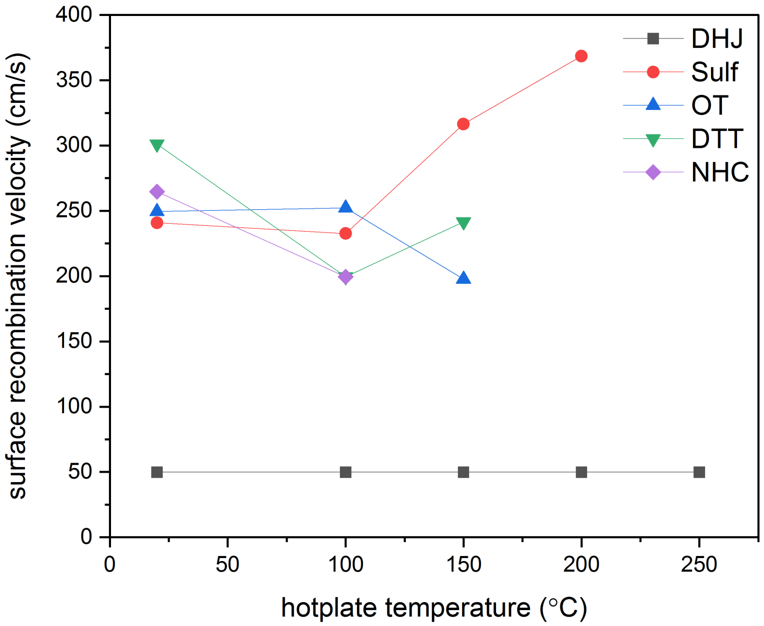

Figure 4.18: TRPL-determined surface recombination velocities of GaAs passivated with GaInP on the rear and GaInP (DHJ, grey square), sulfide (red circle), octanethiol (blue triangle △), dithiothreitol (green triangle ▽), and n-heterocyclic carbene (purple diamond) after 5 minutes on a hotplate at the reported temperatures for which passivation is maintained with each treatment.

photovoltaic devices and in the search for new heterojunctions.

Chapter 5

SIMULATION OF II-VI CARRIER-SELECTIVE CONTACTS

While this thesis focuses on a small subset of potential heterojunctions for photovoltaic devices, the parameter space within these materials offers a wide range of possible carrier-selective contact designs. With respect to $\mathrm{ZnS_xSe_{1-x}}$ thin films on silicon absorbers, knowledge of the material or heterojunction properties themselves do not sufficiently inform a choice for alternative carrier-selective contact. ZnS has a wider band gap than ZnSe, leading to greater transparency, but ZnSe boasts higher electron mobility than ZnS. Both predicted and experimentally determined band offsets of ZnS and ZnSe on Si favor ZnSe as an electron-selective contact based on lower barrier height. As electron-selective contacts are of primary interest in this work, and a key unknown was the quantitative role of an energy barrier in the form of a large conduction band offset, an initial study on the transmission probability of electrons across a heterojunction was performed. Next, full devices were modeled in Sentaurus TCAD and their performance simulated for a thorough comparison of the array of possible $\mathrm{ZnS_xSe_{1-x}}$ carrier-selective contacts in SHJ devices [39].

5.1 Transmission Probability at Contact Interfaces

To have a more intuitive understanding of the role of the conduction band offset in reducing electron collection, transmission probability at a $\mathrm{ZnS_xSe_{1-x}}$/Si interface is approximated as a function of conduction band offset and $\mathrm{ZnS_xSe_{1-x}}$ doping. For an incoming electron with an assumed kinetic energy E based on the expected magnitude of band bending in the p-type c-Si absorber, the transmission probability across the barrier is calculated in three regimes: first where barrier height (i.e. built in potential or conduction band offset) ψ is greater than electron energy E, second where barrier height $\psi = E$, and finally when $\psi < E$.

In the first case where the electron energy is less than the barrier height, electrons must tunnel through the barrier in order to be collected in the contact. The transmission probability, also known as the transmission coefficient or tunneling coefficient, is calculated using the WKB approximation as

$$T_{E<\psi} = \frac{\exp\left(-2\int_{x_1}^{x_2} dx\sqrt{\frac{2m}{\hbar^2}(V(x)-E)}\right)}{\left(1+\frac{1}{4}\exp\left(-2\int_{x_1}^{x_2} dx\sqrt{\frac{2m}{\hbar^2}(V(x)-E)}\right)\right)^2}. \tag{5.1}$$

The bounds of integration x_1 and x_2 are the classical turning points between which the potential barrier is higher than the electron energy. In this case, x_1 is at the interface between the CSC and the Si absorber and x_2 is in the depletion region where the magnitude of band bending brings the CSC conduction band below the electron energy. This depth into the contact, known as the depletion width, depends on the barrier height ψ, material permittivity ε_s, and donor concentration N_D as

$$W_D = \sqrt{\frac{2\varepsilon_s\psi}{qN_D}} \tag{5.2}$$

where q is the elementary charge. The profile of the potential barrier $V(x)$ takes a quadratic shape referenced to 0 eV at the substrate side of the classical turning point and again dependent on donor concentration, material permittivity:

$$V(x) = \frac{qN_D}{\varepsilon_s}\left[\frac{W_D^2}{2} - W_D x + \frac{x^2}{2}\right]. \tag{5.3}$$

The upper bound of integration x_2 is thus found by solving the equation $V(x_2) = \psi$.

In the cases where the electron energy is greater or equal to the barrier height, we simplify our calculation by assuming a rectangular barrier, still with width W_D. This assumption is made because we expect our primary losses in transmission to be for $E < \psi$. The simplification to a rectangular barrier rather than a quadratically decaying spike will underestimate the transmission probability for $E \geq \psi$, but as our results show, this undercount is insignificant compared to the $E < \psi$ region. Under the rectangular barrier assumption, the transmission probability at $E = \psi$ evaluates to

$$T_{E=\psi} = \frac{1}{1 + mW_D^2\psi/2\hbar^2}. \tag{5.4}$$

At electron energies above the conduction band offset, the transmission probability is

$$T_{E>\psi} = \frac{1}{1 + \frac{\psi^2 \sin kW_D{}^2}{4E(E-\psi)}} \tag{5.5}$$

where the wave number k is given by

$$k = \sqrt{2m(E-\psi)/\hbar^2}. \tag{5.6}$$

Prior to knowledge of the actual conduction band offset, or to explore the influence of a tunable conduction band offset (perhaps based on surface treatments), the exploration of transmission probability as a function of band offset and dopant concentration for a given material can guide prioritization of experimental measurements. In Fig. 5.1, we compare the transmission probability T for ZnS (a, b) and ZnSe (c, d) as for assumed incident electron energy of 1 eV (a, c) and 0.5 eV (b, d). Because the only CSC material-dependent parameters taken into account in these calculations are permittivity and effective mass, which are each similar between ZnS and ZnSe, there is no significant difference between the transmission probabilities from material to material. The incident electron energies were chosen as test cases based on the energy difference between the conduction bands in the bulk of the Si substrate and II-VI CSC. We can see a general trend that when the conduction band offset is more than the electron energy (electron must tunnel), the transmission probability is near zero except at high doping. With its slightly larger permittivity and smaller effective electron mass, tunneling is more likely in ZnSe than ZnS. Of course, the energy of incident electrons is not one value, but a distribution based on the wavelength of the exciting photon, where in the device the light was absorbed, and any loss processes the electron may have undergone before reaching the contact. After conduction band offsets were measured, another layer of specificity was added to the model. Figure 5.2 shows transmission probability T as a function of electron energy for (a) ZnS, with ψ =1.1 eV and (b) ZnSe, with $\psi = 0.7\ eV$. Again we can see that when electrons must tunnel ($E < \Delta E_{CB}$), their collection is significantly reduced.

Again, this is a simple model that does not account for the differences in light absorption profiles as the mole fraction, thickness, and dopant density varies in a $\mathrm{ZnS_xSe_{1-x}}$ contact, nor does it take into account the difference between the energy band profiles without bias in the dark and the quasi Fermi levels that actually define carrier transport in a device. To account for these factors, we must use full device simulation.

5.2 Introduction to Photovoltaic Device Simulation

Sentaurus TCAD

Full device simulations were performed in Sentaurus TCAD from Synopsys. Sentaurus includes an advanced multidimensional device simulator that models optical, electrical, and thermal characteristics of semiconductor devices. While the physics models and material properties provided in Sentaurus are centered around crys-

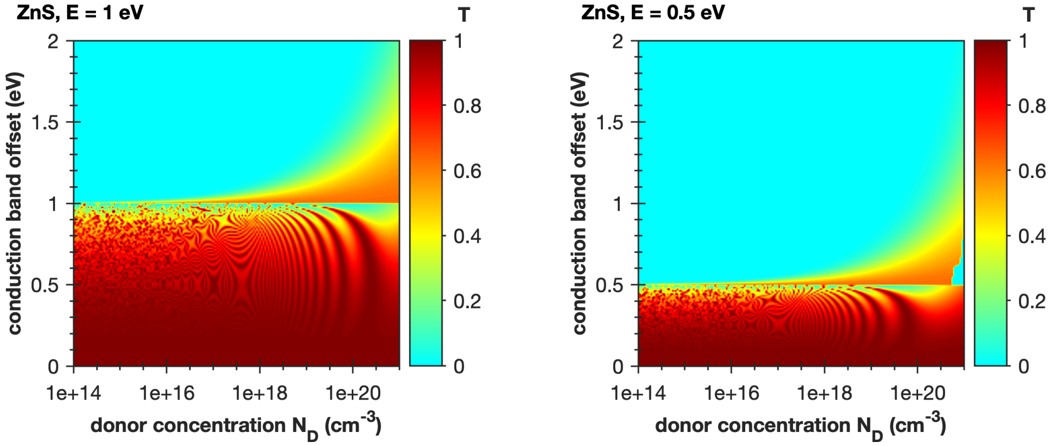

(a) ZnS, E = 1 eV (b) ZnS, E = 0.5 eV

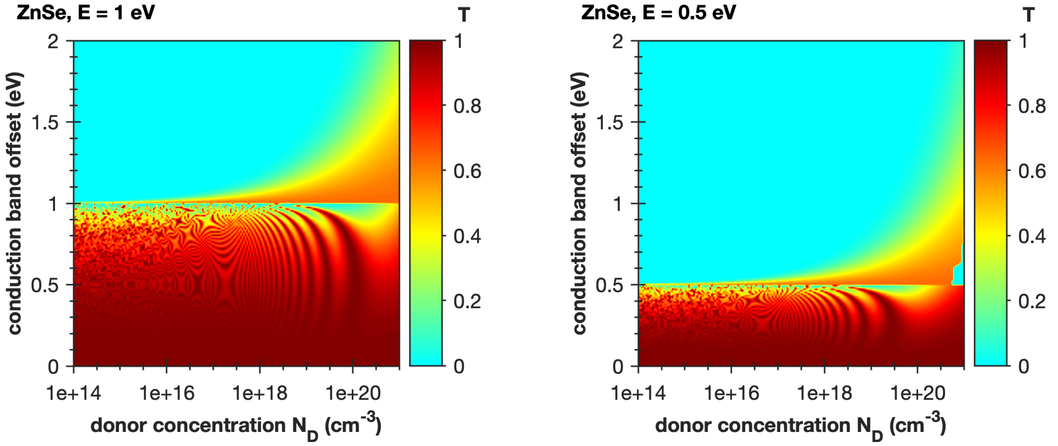

(c) ZnSe, E = 1 eV (d) ZnSe, E = 0.5 eV

Figure 5.1: Electron transmission probabilities across ZnS (a, b) and ZnSe (c, d) conduction band barriers as a function of ZnS_xSe_{1-x} donor concentration N_D and conduction band offset for assumed incident electron energies of 1 eV (a, c) and 0.5 eV (b, d). Transmission probability is near 1 when for conduction band offsets less than electron energy and near 0 for higher offsets, except at high donor concentrations.

talline silicon, detailed models for the properties of any material can be defined. Importantly, this includes the parameterization of properties of mole fraction materials such as ZnS_xSe_{1-x} as a function of x. Critical to these device simulations is the handling of degenerately-doped wide band gap semiconductors, including controllable band offsets and carrier transport via tunneling.

Three types of devices were modeled in Sentaurus TCAD to compare the performance of a ZnS_xSe_{1-x} carrier-selective contact (CSC) to an a-Si CSC in a SHJ-style

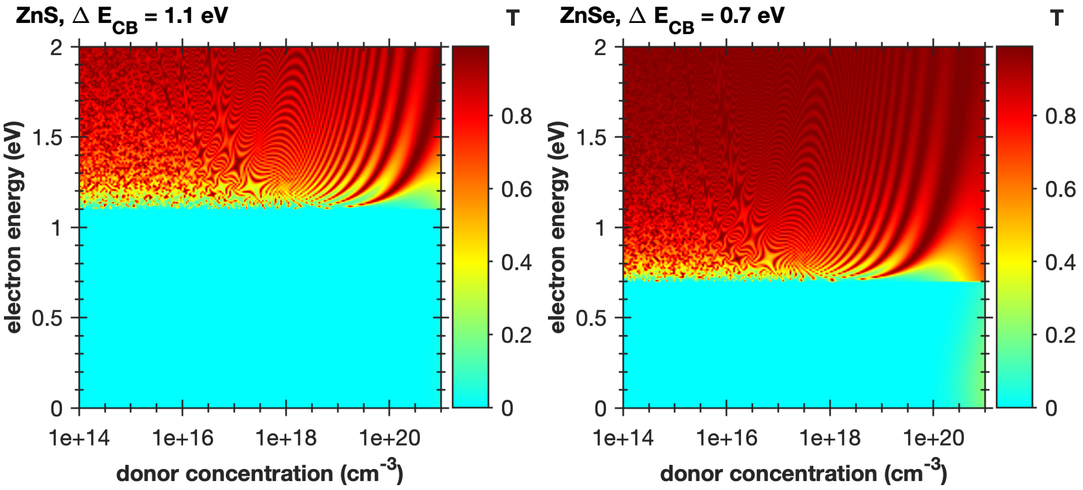

(a) ZnS, $\Delta E_{CB} = 1.1\ eV$ (b) ZnSe, $\Delta E_{CB} = 0.7\ eV$

Figure 5.2: Electron transmission probabilities across ZnS (a) and ZnSe (b) on Si conduction band barriers as a function of $\mathrm{ZnS_xSe_{1-x}}$ donor concentration and incident electron energy.

solar cell. First, a p-type SHJ cell with an a-Si CSC on each side was modelled, using the device parameters outlined in [40] to serve as a control simulation. Second, a SHJ-style cell with a p-type c-Si absorber, p-type hole-selective a-Si rear contact, and n-type electron-selective $\mathrm{ZnS_xSe_{1-x}}$ front contact. Third, a SHJ-style cell with a p-type c-Si absorber, p-type hole-selective a-Si rear contact, an intrinsic a-Si front passivating layer, and an n-type electron-selective $\mathrm{ZnS_xSe_{1-x}}$ front contact. The $\mathrm{ZnS_xSe_{1-x}}$ donor concentration N_D, thickness, and mole fraction x were varied to find the $\mathrm{ZnS_xSe_{1-x}}$-based CSC leading to the highest-efficiency solar cell. Simulated device parameters including efficiency, short-circuit current, open-circuit voltage, and fill factor were calculated as metrics for viability of a $\mathrm{ZnS_xSe_{1-x}}$ CSC on Si. Additionally, modified versions of the contact-specific and device-level metrics for passivation, conductivity, and selectivity introduced in [41] were employed to more specifically analyze the impact of design variation.

5.3 Reference Device Model

The control SHJ model was based on the p-type device discussed in [40], as Kanevce and Metzger also include experimental results of a device with similar architecture. In order to reduce simulation time, a 100-micron c-Si base was chosen for the $\mathrm{ZnS_xSe_{1-x}}$ models. Both 100-micron and 250-micron base-thickness devices were simulated for the reference SHJ models, and for select $\mathrm{ZnS_xSe_{1-x}}$-CSC models.

Table 5.1: Reference device parameters

Parameter **Layer**	t (nm)	E_g (eV)	χ (eV)	N_D ($\mathrm{cm^{-3}}$)	μ_e $\mathrm{cm^2/V\text{-}s}$	μ_h $\mathrm{cm^2/V\text{-}s}$
c-Si	100 000	1.12	4.05	10^{16}	1500	450
a-Si:H (intrinsic)	5	1.67	3.95	10^{13}	1	0.01
a-Si:H (doped)	5	1.67	3.95	10^{19}	1	0.01
ITO	70	3.7	4.5	10^{20}	50	30

[a] Ref. [40]

Specifics of the reference device architecture are listed in Table 5.1. Mid-gap Gaussian defects were modeled for each layer, following the profile

$$N_G(E) = N_0 \exp\left(-\frac{(E - E_0)^2}{2\sigma^2}\right),$$

where the peak concentration N_0 in $\mathrm{eV^{-1}cm^{-3}}$ is calculated from the volume defect density N_{tr} in $\mathrm{cm^{-3}}$ as

$$N_0 = \frac{N_{tr}}{\sigma\sqrt{2\pi}}.$$

The band tail states of a-Si are modeled with exponential traps at the band edges following the profile

$$N_T(E) = N_0 \exp\left(-\left|\frac{E - E_0}{\sigma}\right|\right)$$

where the peak concentration N_0 is related to the volume defect density N_{tr} as

$$N_0 = \frac{N_{tr}}{\sigma}.$$

In both types of traps, σ, or E_S in Sentaurus documentation is characteristic of the energy spread of the defects. The specific parameters of each trap modeled is included in Table 5.2.

5.4 Standard Device Metrics

The primary metric of interest for photovoltaic devices is the power conversion efficiency, i.e. the ratio of maximum extracted power to incident power. In order to understand the loss mechanisms that reduce power, photovoltaic devices are characterized not just at their maximum power operating point, but at short-circuit (no voltage across the device) and at open-circuit (no current across the device).

Table 5.2: Trap/Defect parameters

Trap Label	Type	Profile	E_0 (eV)	E_0 ref.	σ (eV)	N_0 $\mathrm{eV}^{-1}\mathrm{cm}^{-3}$
c-Si db	A	G	0	mid	0.15	6.65×10^{12}
a-Si:H (i) db	A + D	G	0.15	mid	0.15	2.66×10^{16}
a-Si:H (i) bt	A	E	0	CB	0.02	2.50×10^{20}
a-Si:H (i) bt	D	E	0	VB	0.05	2.50×10^{20}
a-Si:H (n/p) db	A + D	G	0.15	mid	0.2	1×10^{18}
a-Si:H (n/p) bt	A	E	0	CB	0.07	1×10^{21}
a-Si:H (n/p) bt	D	E	0	VB	0.12	1×10^{21}
ITO db	A	E	0	mid	0.15	2.66×10^{15}

[a] Ref. [40]

The efficiency, often represented by the Greek letter η, is then related to the short circuit current density, J_{sc}, and open-circuit voltage, V_{oc}, via the fill factor (FF), a unitless measure of the "squareness" of an IV (current-voltage) curve (see Eq. 5.7 and Eq. 5.8).

$$\eta = \frac{J_{mp}V_{mp}}{P_{in}} = \frac{J_{sc}V_{oc}FF}{P_{in}} \tag{5.7}$$

$$FF = \frac{J_{mp}V_{mp}}{J_{sc}V_{oc}} \tag{5.8}$$

As discussed in Chapter 1 regarding device efficiency, the maximum FF for a given absorber is not 100%. An empirical expression for the maximum FF as a function of normalized V_{oc} ($v_{oc} = \frac{q}{nkT}V_{oc}$) is given by

$$FF_{max} = \frac{v_{oc} - \ln v_{oc} + 0.72}{v_{oc} + 1} \tag{5.9}$$

where q is the elementary charge, k is the Boltzmann constant, and n is the ideality factor related to the dominant recombination mechanism [42]. The maximum FF of a laboratory silicon PV device is around 0.85 or 85%. If we consider a circuit model of a solar cell, we can identify two types of parasitic resistances. First is the series resistance R_S, in series with the photogenerated current I_{ph} and the dark saturation current I_0 (in parallel with each other). The main contributors to series resistance are the contact resistances and bulk resistance of the absorber. The other type of parasitic resistance is the shunt resistance, which characterizes alternative recombination pathways for photogenerated carriers rather than across the load. The smaller the shunt resistance, the more current across the shunt pathways, which are mostly due to manufacturing defects. The current across the device as a function of voltage is given by

$$I = I_{ph} - I_0 \exp\left[\frac{q(V + IR_s)}{nkT}\right] - \frac{V + IR_S}{R_{SH}}. \tag{5.10}$$

The individual contributions to parasitic resistances will be considered further in the next section. For a specific photovoltaic device, the short-circuit current depends on the area of the solar cell, the power (intensity) and spectrum (wavelength dependence) of the incident light, the optical properties of the solar cell, and the collection probability of the charge carriers. To most directly compare photovoltaic device designs, it is standard to consider current density per unit area (J or j) rather than current (I). While the solar spectrum changes with time of day, location, and weather, the AM1.5G light spectrum is assumed as a convenient standard. The AM1.5G spectrum is calculated from the AM0 spectrum (no air between sunlight an cell), and is representative of the sunlight incident on a solar cell at sea level, where the sun is shining at 11.2° from the cell's normal vector, the cell faces a blue sky and light sandy soil without concentration of light (G for "global" condition), and the sun is 41° above the horizon. This angle of the sun corresponds to a path length through the atmosphere 1.5 times longer than when the sun is at its zenith (high noon), also known as "air mass 1.5" (AM1.5), compared to air mass 1 (AM1) for the sun at its zenith, or air mass 0 (AM0) for sunlight before it passes through the atmosphere. The AM1.5G spectrum has an integrated power of 100 mW/cm^2, and this corresponds to the incident power P_{in} in all following data.

The optical properties of the solar cell and the collection probability of the charge carriers vary between the designs considered in this study. The previous section on transmission probability began the exploration of collection probability with changing CSC donor concentration and conduction band offset, and will be further discussed in the next section. The Sentaurus model includes the wavelength-dependent absorption and extinction coefficients for each layer, and so can accurately simulate where within the cell each wavelength of light is absorbed. The main impact on light absorption profiles in the studied designs is the CSC band gap (as a function of mole fraction) and the CSC thickness.

5.5 Carrier-Selective Contact Metrics

While full device simulations can be compared based on their performance metrics (efficiency, short-circuit current, open-circuit voltage, fill factor), it is useful to calculate carrier-selectivity metrics to elucidate specifically how the changes in a contact design influence the device operation. As shown in [41], good passivation and good conductivity imply good selectivity, but despite the name "carrier-selective contact," good selectivity does not imply good efficiency, although all other things being equal, the most selective devices will be the highest efficiency. To gain insight into the influence of $\mathrm{ZnS_xSe_{1-x}}$ CSC parameters on device performance, metrics for passivation ($\rho_{\mathrm{c,\,total}}$, (5.13)), conductivity ($P_{\mathrm{res,\,loss}}$, (5.17)), and selectivity (S_{tot}, (5.20)) were compared between a-Si and $\mathrm{ZnS_xSe_{1-x}}$ CSCs [41]. These metrics are based in an electrical circuit model of a solar cell, where electron and hole currents, dark recombination currents, and contact resistances can be related to the voltage across the absorber and across the device. Given their separate populations, electrons in the conduction band and holes in the valence band are treated as separate current pathways. There is a positive, voltage independent current from the conduction band to the valence band as carriers are photogenerated with current density j_{ph}. There are multiple voltage-dependent recombination currents from the valence band to the conduction band in the bulk, namely radiative recombination, trap-assisted recombination, and Auger-Meitner recombination. In each contact, there is positive current from the hole population and negative current from the electron population to the single Fermi level of the electrode. At open-circuit, when current across the device is 0, the circuit can be summarized as

$$0 = j_{ph} + \sum_i j_{0,i}\left(1 - \exp\left(\frac{q \times iV_{oc}}{n_i kT}\right)\right) - \frac{iV_{oc}}{\rho^l_{c,e} + \rho^l_{c,h}} - \frac{iV_{oc}}{\rho^r_{c,e} + \rho^r_{c,h}} \tag{5.11}$$

where i iterates through the bulk recombination pathways, and the partial specific contact resistances relate the partial currents (j_e, j_h) to the quasi Fermi level collapse in the relevant contact (see Eq. (5.21)).

Passivation

Passivation is the measure of how well carrier recombination is prevented. Different passivation mechanisms block the occupation of defect states (recombination sites in the bandgap) by charge carriers. In a well-passivated material, more electrons (holes) are in the conduction band (valence band) rather than in a mid-gap defect state. Given this higher occupation, the quasi-Fermi level(s) are farther away from the intrinsic quasi-Fermi level E_i, implying a higher open-circuit voltage. From Eq. (5.11), since j_{ph} is voltage independent, implied V_{oc} is maximized where the partial specific contact resistance coefficient is maximized.

$$iV_{oc}\left[\frac{1}{\rho^{l}_{c,e}+\rho^{l}_{c,h}}+\frac{1}{\rho^{r}_{c,e}+\rho^{r}_{c,h}}\right]=iV_{oc}\times\frac{\rho^{l}_{c,e}+\rho^{l}_{c,h}+\rho^{r}_{c,e}+\rho^{r}_{c,h}}{\left(\rho^{l}_{c,e}+\rho^{l}_{c,h}\right)\left(\rho^{r}_{c,e}+\rho^{r}_{c,h}\right)} \tag{5.12}$$

Comparing to Eq. (5.10), we can see that this factor is analogous the shunt resistance, and is a convenient full device passivation metric.

$$\rho_{\text{c, total}}=\frac{\left(\rho^{l}_{c,e}+\rho^{l}_{c,h}\right)\left(\rho^{r}_{c,e}+\rho^{r}_{c,h}\right)}{\rho^{l}_{c,e}+\rho^{l}_{c,h}+\rho^{r}_{c,e}+\rho^{r}_{c,h}} \tag{5.13}$$

Conductivity

Conductivity is a measure of the ease of travel of a charge carrier through a material, or the current of charge carriers across a unit of potential difference over a unit distance (A V^{-1} cm^{-1} in SI units). Partial (carrier-specific) conductivities $\sigma_{e/h}$ are calculated as the product of elementary charge q, charge carrier mobility $\mu_{e/h}$, and charge carrier density $n_{e/h}$:

$$\sigma_e = q\mu_e n_e \tag{5.14}$$

$$\sigma_h = q\mu_h n_h. \tag{5.15}$$

At open circuit conditions, the sum of partial currents must cancel out ($j_e + j_h = 0$). Since the partial currents are directly proportional to the relevant partial conductivities and qFL gradients, any asymmetry in partial conductivity (due to asymmetry in mobility or density) will lead to an asymmetry in qFL gradient. While mobility is hard to control except through choice in material, density is easier to influence through design choices like contact work function, doping, or defect states. In a non-absorbing contact, the partial specific contact resistance is related to the average partial conductivity across the contact as

$$\rho_{e/h}=\frac{L_c}{\overline{\sigma_{e/h}}}. \tag{5.16}$$

This suggests a convenient metric for conductivity based on the reduction of resistive losses at maximum power operating conditions. For an electron selective contact on the left and hole selective contact on the right, we have

$$P_{\text{res, loss}}=\left(\rho^{l}_{c,e}+\rho^{r}_{c,h}\right)j_{mpp}^{2} \tag{5.17}$$

where j_{mpp} is the current density at the maximum power point.

Selectivity

Asymmetry in qFL collapse between carriers in one contact is the basis for contact-specific selectivity and asymmetry in qFL for the same carrier between contacts is the basis for device level selectivity. At the contact-specific level, selectivity describes the collection probability of one carrier compared to another. The larger the partial contact resistivity is for one carrier compared to another, the more of the qFL collapse occurs in a single population, and the closer the electrode Fermi level is to the qFL for the carrier with lower partial contact resistivity. Thus the electron selectivity for a specific contact can be defined as

$$S_e = \frac{\rho_h}{\rho_e + \rho_h} \tag{5.18}$$

and similarly for a hole contact. The sum of partial specific contact resistances is used in the denominator so that contact selectivity takes values between 0 and 1, inclusive. At a device level, if the carrier selectivity were identical between contacts ($S_e^l = S_e^r$), there would be no voltage across the device. Hence, a device-level selectivity metric must optimize for opposite selectivity between opposing contacts, as well as high contact-specific selectivity. Equivalently, to consider the loss in voltage from iV_{oc} (proportional to qFL in bulk) to V_{oc} (Fermi level separation between electrodes), we see the voltage loss in each contact is related to any undesired selection for the minority carrier, i.e. S_h in the electron contact and S_e in the hole contact. The voltages are thus related by

$$V_{oc} = iV_{oc}\left[1 - S_h^l - S_e^r\right] \tag{5.19}$$

and device level selectivity is defined as a unitless measure between -1 and 1 as

$$S_{\text{tot}} = \frac{V_{oc}}{iV_{oc}} = \left[1 - \frac{\rho_{c,h}^l}{\rho_{c,e}^l + \rho_{c,h}^r} - \frac{\rho_{c,e}^r}{\rho_{c,e}^r + \rho_{c,h}^l}\right]. \tag{5.20}$$

In this framework, defined in [41], negative selectivity means the electron selective contact is at the front. In Sentaurus, we extract the voltage as positive regardless of which contact is in front, so depending on which device parameters are used to calculate selectivity (voltages or resistivities), the negative sign may be dropped.

Metric Modification for Absorbing Contacts

In [41], it is assumed that no absorption occurs in the contacts. Since one of the motivations of the device is to reduce parasitic absorption in the front contact, the partial specific contact resistance definitions are modified as follows:

$$\rho_{c,e/h} = \frac{\Delta V_{e/h}}{\overline{j_{e/h}}}, \tag{5.21}$$

where the local current has been replaced by the average electron or hole current across the left or right contact:

$$\overline{j_{e/h}} = \frac{1}{L_C} \int_{L_{abs}}^{L_{abs}+L_C} j_{e/h}(x)dx. \tag{5.22}$$

The x-position of the outer-edge of the absorber is L_{abs} and $L_{abs} + L_C$ is the outer edge of the contact. In (5.22) only, x represents the position of depth in the device rather than mole fraction composition of the II-VI CSC. The use of voltage drop and current rather than conductivities to calculate partial specific contact resistances further expands the application of these metrics to tunneling contacts and contacts with non-zero recombination at the interface. As a confirmation that this metric modification is necessary for our devices compared to the simplified devices in considered in [41], the passivation, conductivity, and selectivity metrics were calculated using both definitions. In some cases, non-physical results were found for the conductivity-based calculation, such as infinite resistive losses. The validity of the current-based method can be determined by a comparison of the total device selectivity metric. S_{tot} can be calculated from the Sentaurus output in four ways. The first two use the partial-specific contact resistivity ratio definition (right-hand side of (5.20)), where $\rho_{e/h}^{l/r}$ is based on conductivity ((5.16)) or current ((5.21)). The second two use the ratio of the $V_{oc}$to iV_{oc}. The implied V_{oc} can be calculated from the qFL separation or the carrier density in the middle of the absorber.

$$iV_{oc} = \frac{kT}{q} \ln \left[\frac{(N_A + \Delta n)\Delta n}{n_i^2} \right] \tag{5.23}$$

N_A is the acceptor concentration, δn the excess carrier concentration, and n_i the intrinsic carrier concentration, all for the c-Si absorber. When calculating device-level selective S_{tot} with the passivation metric ρ (5.3a, 5.3b), a negative selectivity implies the electron selective contact is on the front. When calculated from bulk values (voltage ratios 5.3c, 5.3d), the sign of the selectivity metric does not change with location (front or back) of the electron-selective contact. As shown in Fig. 5.3, the partial specific contact resistivity based on carrier conductivities yields selectivity measurements inconsistent with the other three methods.

5.6 Simulated Device Performance Results

We find that ZnS_xSe_{1-x} CSCs on c-Si, with and without an a-Si:i passivating layer at the front, perform similarly to a reference p-SHJ cells in experiment and simulation. Table 5.3 lists the efficiency (η), short-circuit current (J_{sc}), open-circuit

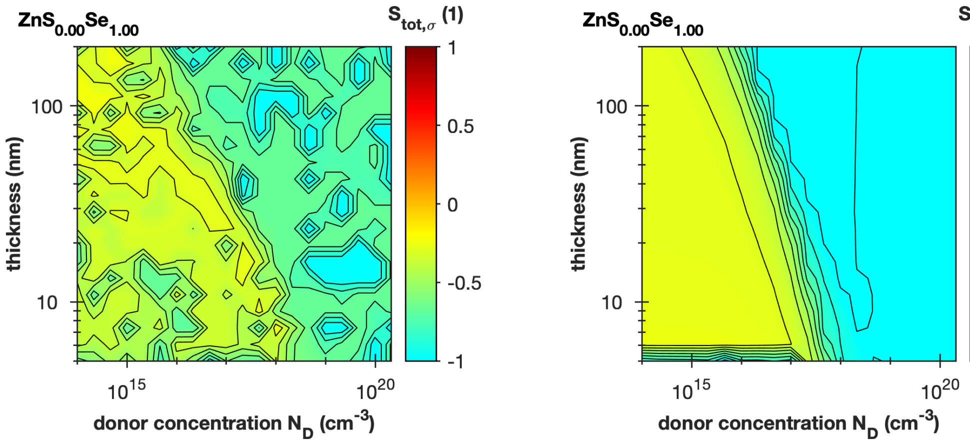

(a) S_{tot} from carrier conductivities

(b) S_{tot} from carrier currents

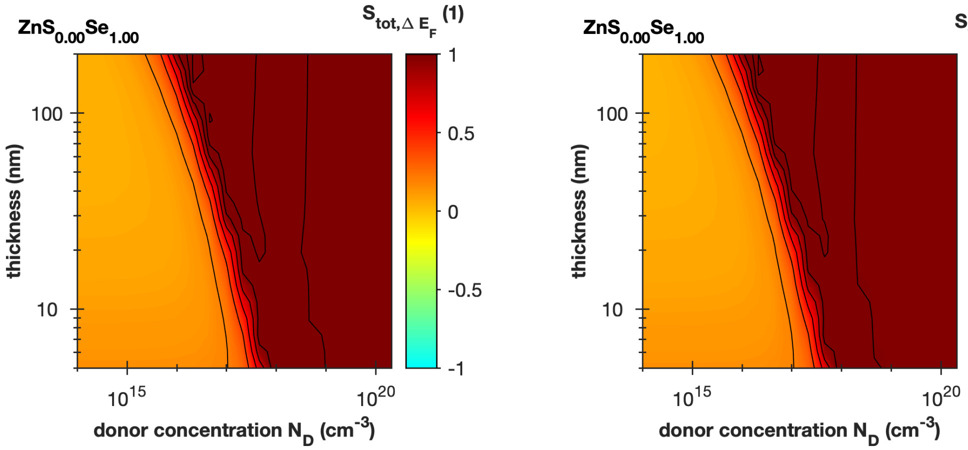

(c) S_{tot} from quasi Fermi level splitting

(d) S_{tot} from carrier concentration

Figure 5.3: Full device selectivity metric S_{tot} calculated four ways for simulated SHJ devices with ZnSe (x = 0) carrier-selective contacts as a function of CSC donor concentration N_D and thickness: (a) $S_{\text{tot},\sigma}$ from carrier conductivities, (b) $S_{\text{tot,j}}$ from carrier currents, (c) $S_{\text{tot},\Delta \text{E}_\text{F}}$ from quasi Fermi level splitting, and (d) $S_{\text{tot,n}}$ from carrier concentration.

voltage (V_{oc}), and fill factor (FF) of a reference experiment cell, a reference p-SHJ simulation, and the champion results of the $\text{ZnS}_\text{x}\text{Se}_{1-\text{x}}$ simulations [40]. The champion devices for the CSCs with and without a-Si were found at nearly the same design parameters ($\text{ZnS}_\text{x}\text{Se}_{1-\text{x}}$ doping $N_D = 4.5 \times 10^{18}$ cm^{-3} and 4.5×10^{19} cm^{-3} respectively, thickness = 62 nm, and mole fraction = 1). The $\text{ZnS}_\text{x}\text{Se}_{1-\text{x}}$ CSCs exhibit superior V_{oc} to the reference SHJ devices. The $\text{ZnS}_\text{x}\text{Se}_{1-\text{x}}$-only CSCs increases J_{sc} and V_{oc} compared to the reference SHJ simulation, and is more efficient than the champion $\text{ZnS}_\text{x}\text{Se}_{1-\text{x}}$+a-Si CSC design. Of the simulated devices, the $\text{ZnS}_\text{x}\text{Se}_{1-\text{x}}$ had the lowest fill-factor, likely a consequence of the large conduction band offset at the ZnS_xSe_{1-x}/c-Si surface. As seen in Fig. 5.4a, while there is not a strong dependence of efficiency on mole fraction, the champion devices are both found at mole fraction x = 1, corresponding to ZnS. Given the large conduction band offset between ZnS and Si, it appears the main advantage of the wider bandgap of ZnS (compared to lower mole fraction ZnS_xSe_{1-x}), outweighs the losses due to the barrier to electron transport at the heterojunction, but not enough to outperform a standard p-SHJ design in simulation.

Table 5.3: Champion performance comparison

Device Type	η **(%)**	J_{sc} **(mA/cm^2)**	V_{oc} **(mV)**	***FF*** **(%)**
ZnSSe CSC	20.9	35.1	744	80.1
ZnSSe+a-Si CSC	20.4	34.1	743	80.2
SHJ ref. sim.	21.5	34.4	731	85.6
SHJ ref. exp.[a]	19.1	35.9	678	78.6

[a] Ref. [40]

5.7 Proposed Designs and Sensitivities

The optimized device consists of a ≈60 nm thick ZnS CSC n-type doped to $\approx 10^{19}\text{cm}^{-3}$, a lightly p-type c-Si absorber, a 5-nm thick a-Si:i rear passivating layer, a 5-nm thick a-Si:p+ hole selective contact, and a full area metallic back contact (assumed as 100 nm Ag in simulation). Figure 5.6 illustrates the device stack (not to scale). Near this design, the most device performance is most sensitive to variations in dopant density. This is because of the key role tunneling plays in electron transport across the large conduction band spike in the ZnS near the interface. We can quantify the important of tunneling by comparing simulated device performance with and without tunneling transport included in the device physics model. Figure 5.7 shows device efficiency as a function of CSC thickness at dopant density $N_D = 4.5\times10^{19}$ cm^{-3} for x = 1 (ZnS) and x = 0 (ZnSe) devices. While the ZnS devices when tunneling is accounted for outperform the ZnSe devices at all thicknesses, when carrier transport through tunneling is not included in the model, the efficiency drops to almost zero. For ZnSe devices at this high dopant density, the effect is less severe, as the conduction band spike is not as large of an energetic barrier. When tunneling is not included in the ZnSe devices, the efficiency (driven by the short-circuit current, not shown here), drops by ≈1% absolute across all thickness. So at N_D = 4.5×10^{19} cm^{-3}, with the 0.7 eV conduction band offset in ZnSe CSC's, some but not most current is from tunneling electrons. The opposite is true for ZnS CSC's, where nearly all current is from electrons tunneling through the conduction band barrier. An experimental analog of turning tunneling on and off is making the barrier too wide for electrons to tunnel through, i.e. decreasing the donor density and therefore increasing the width of the barrier (see (5.2)). The device efficiency is more sensitive to dopant density with a ZnS CSC than a ZnSe CSC. As shown in Fig. 5.8, the efficiency of ZnS CSC devices, while peaking higher than ZnSe CSC devices, begins to drop significantly at N_D = 9×10^{18} cm^{-3}. By 4×10^{18} cm^{-3}, almost all current is lost. For ZnSe CSC devices, similar drops in efficiency do not occur until 2×10^{18} cm^{-3}. The non-monotonic nature of the efficiency change with increasing device thickness is hypothesized to be primarily due to two factors. At the higher thickness end, based on open-circuit voltages greater than 1 V in some low efficiency devices, we propose that at thicknesses greater than 100 nm, significant absorption is occuring in the carrier-selective contact, and it begins to act like a tandem on Si. However, in this regime, very little current is extracted, and the higher open-circuit voltages are coupled with very low fill factors.

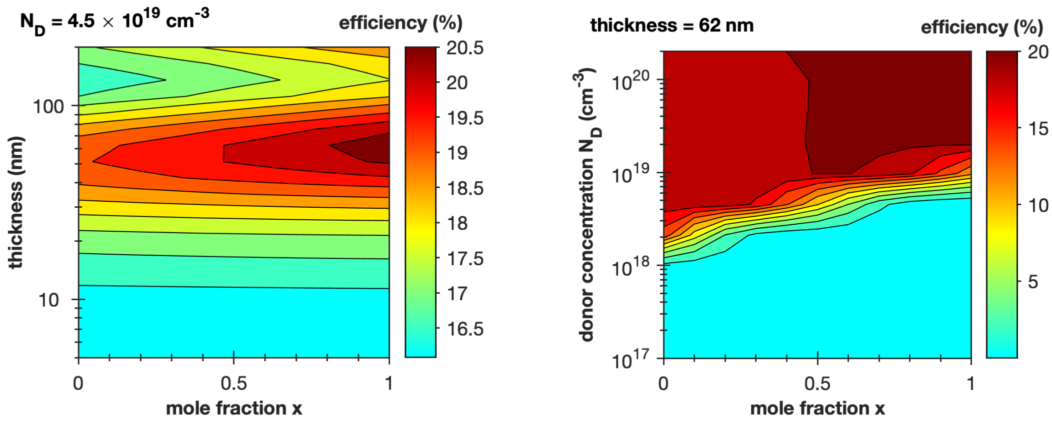

(a) ZnS_xSe_{1-x} doping $N_D = 4.5\times10^{19}$ cm^{-3}

(b) ZnS_xSe_{1-x} thickness 62 nm

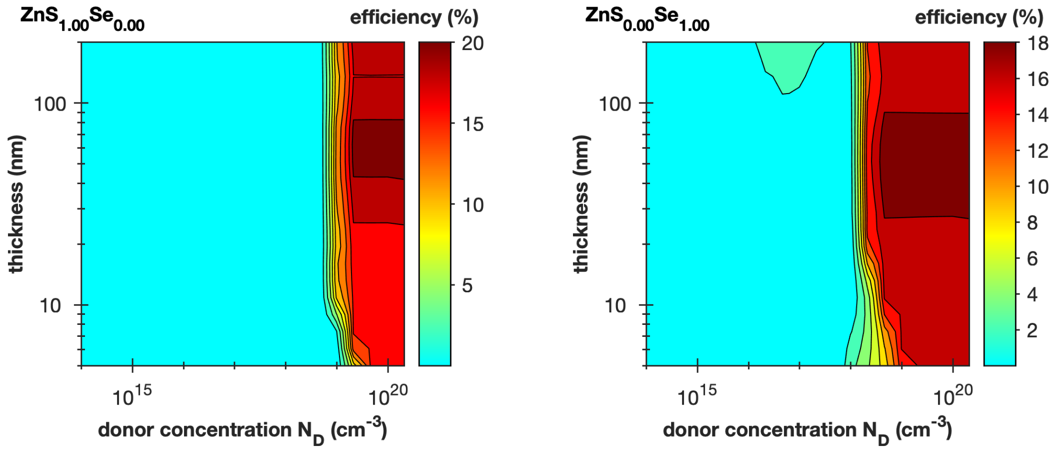

(c) Efficiency of ZnS_xSe_{1-x} mole fraction x = 1 (ZnS)

(d) Efficiency of ZnS_xSe_{1-x} mole fraction x = 0 (ZnSe)

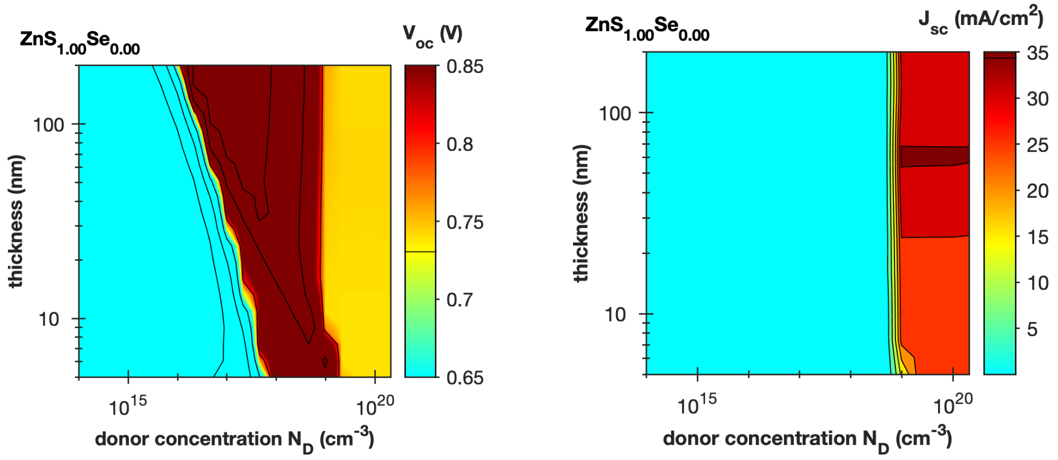

(e) V_{oc} of ZnS_xSe_{1-x} mole fraction x = 1 (ZnS). Black line in color bar indicates reference SHJ device simulated V_{oc}

(f) J_{sc} of ZnS_xSe_{1-x} mole fraction x = 1 (ZnS). Black line in color bar indicates reference SHJ device simulated J_{sc}

Figure 5.4: Device performance for selected subsets of simulations: efficiency of devices with (a) ZnS_xSe_{1-x} doping $N_D = 4.5\times10^{19}$ cm^{-3}, (b) ZnS_xSe_{1-x} thickness 62 nm, (c) ZnS_xSe_{1-x} mole fraction x = 1 (ZnS), and (d) ZnS_xSe_{1-x} mole fraction x = 0 (ZnSe). Cross-sections (a)-(c) include the champion device design.

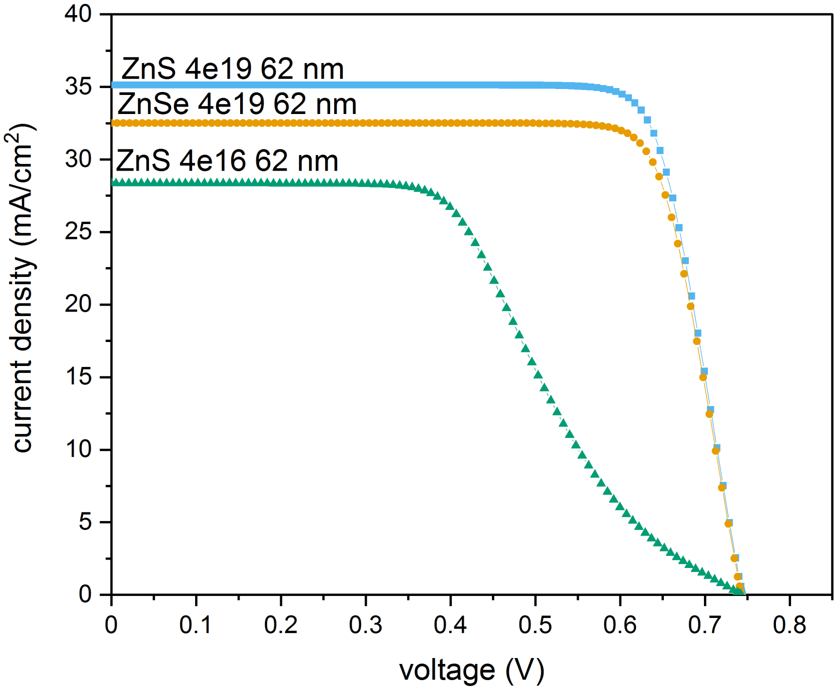

Figure 5.5: Simulated current-voltage curves solar cells with 62-nm thick CSCs of ZnS with donor concentration N_D = 4×10^{19} (top, blue squares), ZnSe with N_D = 4×10^{19} (middle, gold circles), and ZnS with N_D = 4×10^{16} (bottom, green triangles), in order of highest to lowest J_{sc}

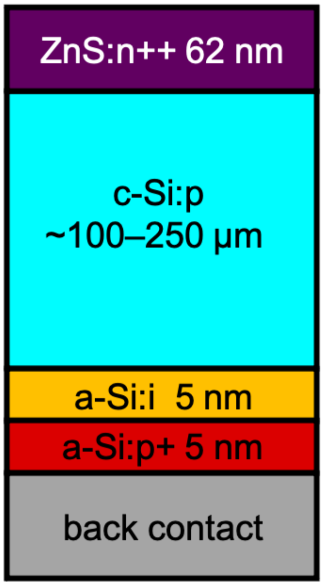

Figure 5.6: Schematic of champion device.

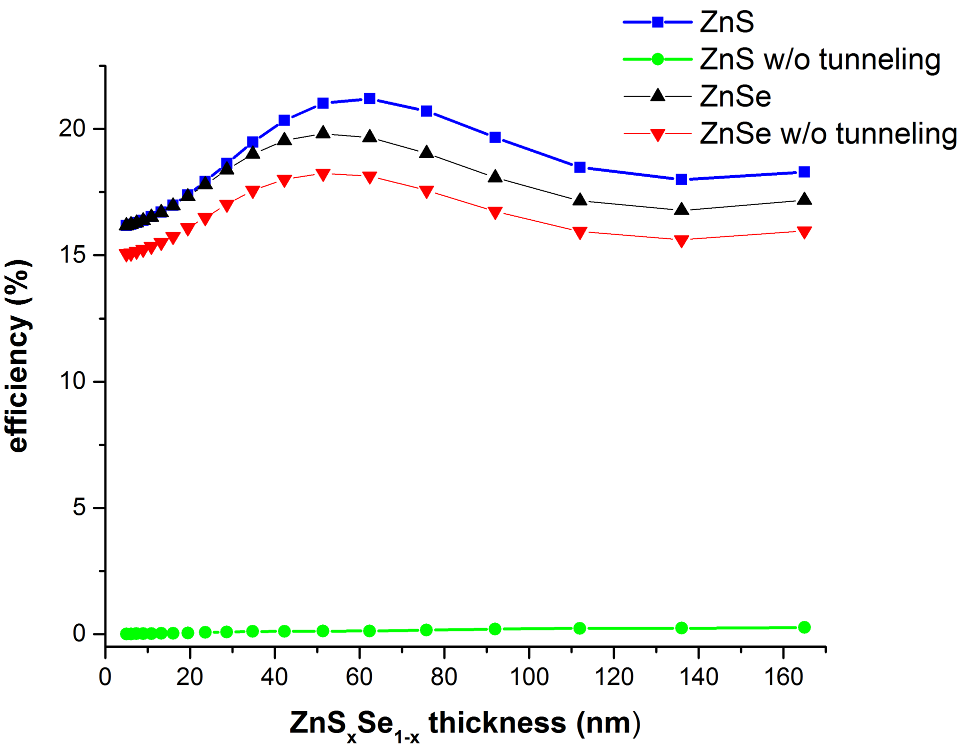

Figure 5.7: ZnS and ZnSe CSC device efficiency as a function of thickness with and without tunneling with $N_D = 4.5\times10^{19}$ cm^{-3}. From top to bottom ZnS CSC with tunneling (blue squares), ZnSe CSC with tunneling (black triangle △), ZnSe CSC without tunneling (red triangle ▽), and ZnS CSC without tunneling (green circles).

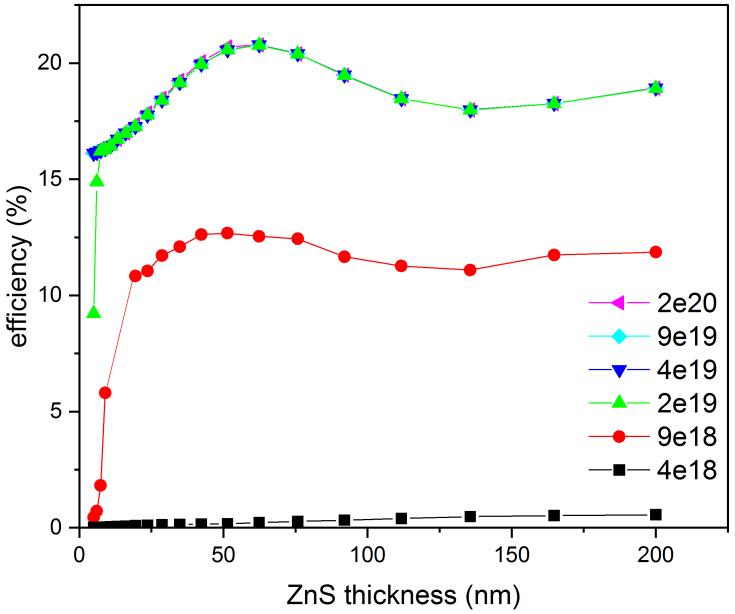

(a) ZnS:n++ CSC device efficiencies

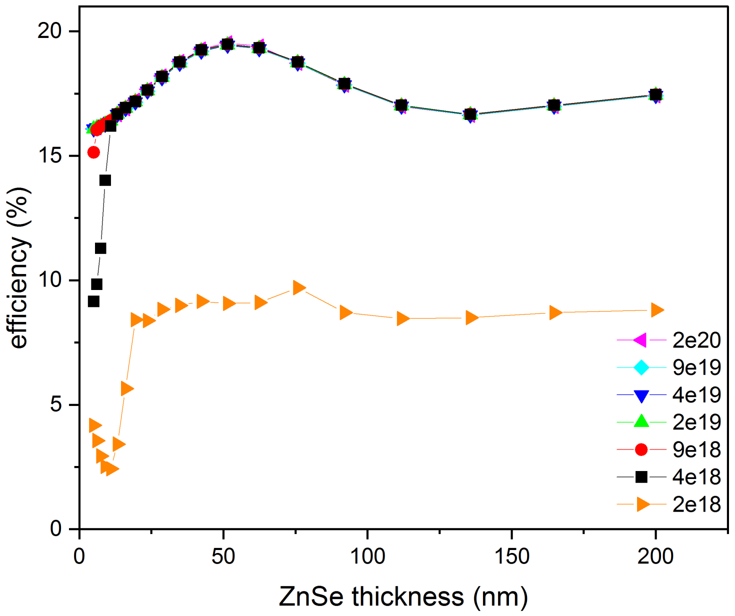

(b) ZnSe:n++ CSC device efficiencies

Figure 5.8: Simulated device efficiencies as a function of ZnS_xSe_{1-x} thickness for highly doped ZnS (a) and ZnSe (b) CSCs. From top to bottom, N_D in cm^{-3} is $2{\times}10^{20}$ (magenta triangles ◂), $9{\times}10^{19}$ (cyan diamonds), $4{\times}10^{19}$ (blue triangles ▽), $2{\times}10^{19}$ (green triangles △), $9{\times}10^{18}$ (red circles), $4{\times}10^{18}$ (black squares), $2{\times}10^{18}$ (orange triangles ▸, (b) only.

Chapter 6

II-VI–ON–C-SI PHOTOVOLTAIC DEVICES

6.1 Fabrication

High-lifetime c-Si wafers were provided to ASU, where PECVD a-Si was deposited and doped (as appropriate) to create a hole-selective back contact consisting of 5 nm a-Si:i and 5 nm a-Si:p. Some wafers also had a 5 nm a-Si:i passivating layer on the front surface of the device. If the front surface was bare, the front surface was cleaned via oxygen plasma ashing and buffered HF drop etching. To maintain the passivation quality of the a-Si:i layers, the samples were heated to only 200°C in the growth chamber. Then, ZnS_xSe_{1-x}:Al was deposited via molecular beam (bulk) and electron beam (Al dopant). The electrical contacting was completed with thermally evaporated silver: 100 nm full coverage on the rear and 50 nm-thick 5 mm-diameter circles on the front. Device edges were further defined via photolithography and mesa etching in a solution of potassium permanganate and phosphoric acid [43].

6.2 Characterization

External Quantum Efficiency

External quantum efficiency (EQE) is a measurement of the number of collected charge carriers per incident photon as a function of photon wavelength (or energy). Because shorter wavelengths of light are primarily absorbed near the front of the cell, changes in EQE in the blue region correlates with loss factors dominating at the front of the cell, namely front surface recombination, and in our case, significant contact resistance. For longer wavelengths of light still above the band gap of the absorber that are absorbed deeper in the device, losses in EQE are influenced by the quality of the rear contact and reduced absorption. In the case of comparison to a SHJ with a-Si layers as the top contact, since ZnS_xSe_{1-x} contacts parasitically absorb less in the wavelength regime bounded by the band gaps of ZnS and a-Si (namely between $\approx$350 nm and $\approx$700 nm), there should be some gains in EQE in this low-to mid-wavelength regime if the previously parasitically absorbed light instead leads to collected charge carriers. The measured EQE of a ZnS/SHJ device is shown in Fig. 6.1. Unfortunately, stable Ohmic contact was quite difficult to achieve with the fabricated devices. Hall measurements showed that donor activation was quite low (<1%) as fabricated, and efforts to activate the donors via annealing in forming gas

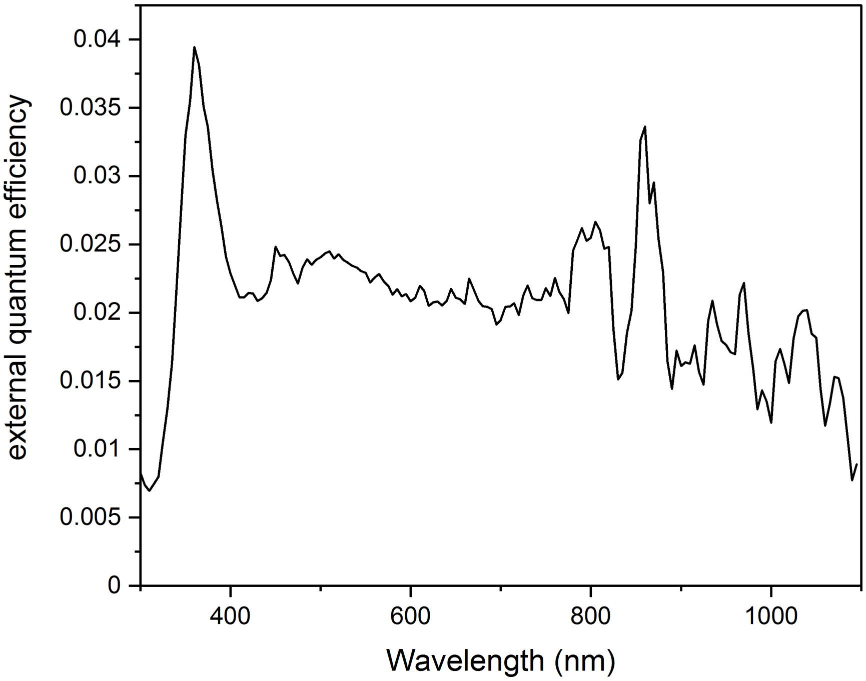

Figure 6.1: External quantum efficiency as a function of wavelength for SHJ device with ZnS:Al top contact and silver electrodes on top and bottom. EQE values are quite noisy, indicating poor electrical contact or non-optimal contact properties.

still did not reach sufficiently high donor concentration to match the goal device. The mismatch between expected and actual device performance is ascribed primarily to insufficient donor concentration, which leads to untenably high series resistance.

I-V Curves

6.3 Transition to Industry

Through discussions with scientists at NREL, an industrial-scale fabrication option and cost modeled were identified. Full device fabrication and characterization for the research cells was undertaken at two separate locations, namely ASU and Caltech. The a-Si layers were deposited at ASU, the ZnS_xSe_{1-x} CSCs were deposited at Caltech, and characterization was done at Caltech. This motivated a-Si deposition to precede ZnS_xSe_{1-x}, but given the non-neglible impact of ZnS_xSe_{1-x} deposition processes on the thin a-Si layers, we propose a reversal of that fabrication order for a single-location fabrication. A general schematic of a silicon heterojunction device fabrication process is shown in Fig. 6.3, with the primary process change outlined

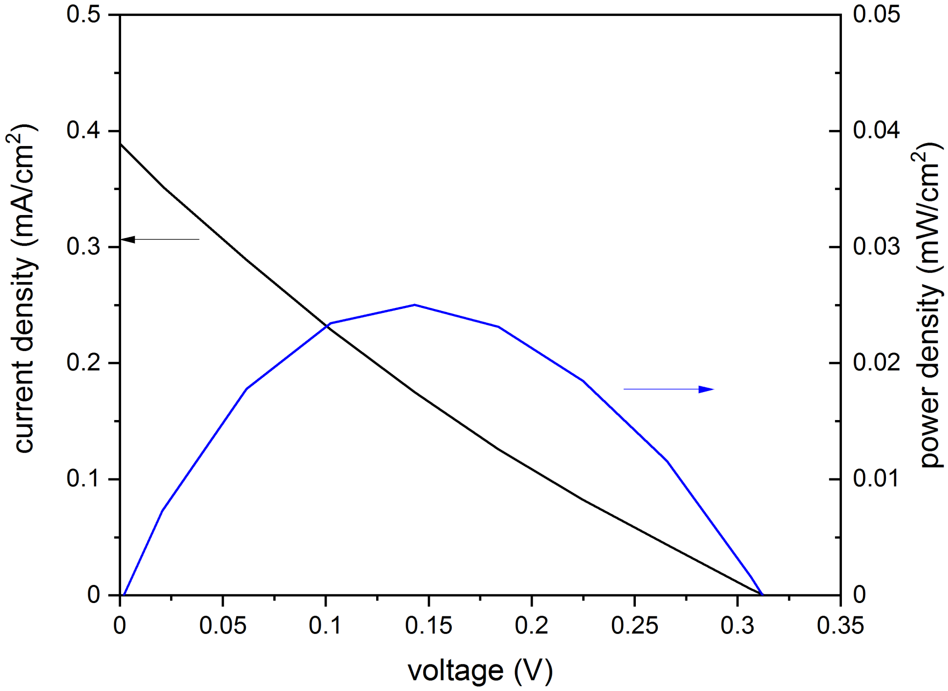

Figure 6.2: Current-voltage curve (black, left ordinate) and power-voltage curve (blue, right ordinate) for ≈ 0.25 cm^2 SHJ device with ZnS:Al top contact and silver electrodes. J_{sc} of ≈0.4 mA/cm^2, V_{oc} of ≈0.3 V, and FF of ≈50% indicate CSC and top electrodes are contributing to significant unintended absorption and series resistance.

in step 4. Since the ZnS CSC in this study is an n-doped electron selective contact and the remain a-Si CSC is hole selective, the order of contact depostion changes compared to a standard process (n then p rather than p then n). The fabrication would proceed as follows: test incoming wafer, saw damage removal and surface texturization in KOH bath, HF dip for oxide removal, atomic layer deposition of ZnS carrier-selective contact, plasma-enhanced chemical vapor deposition (PECVD) of 5-nm thick intrinsic a-Si passivation layer and 5-nm thick p-doped a-Si hole-selective layer, sputter rear transparent conducting oxide for bifacial option, screen print mask on front and back, plate metallic contacts, remove contact masks, and characterize via current-voltage measurements and sort cells accordingly. It is estimated that the cost per unit area in high volume manufacturing of ALD ZnS will be similar to the PECVD a-Si it replaces, so the levelized cost of energy advantage of a ZnS-SHJ over a standard SHJ will primarily be through the increased efficiency. For the 1.7%

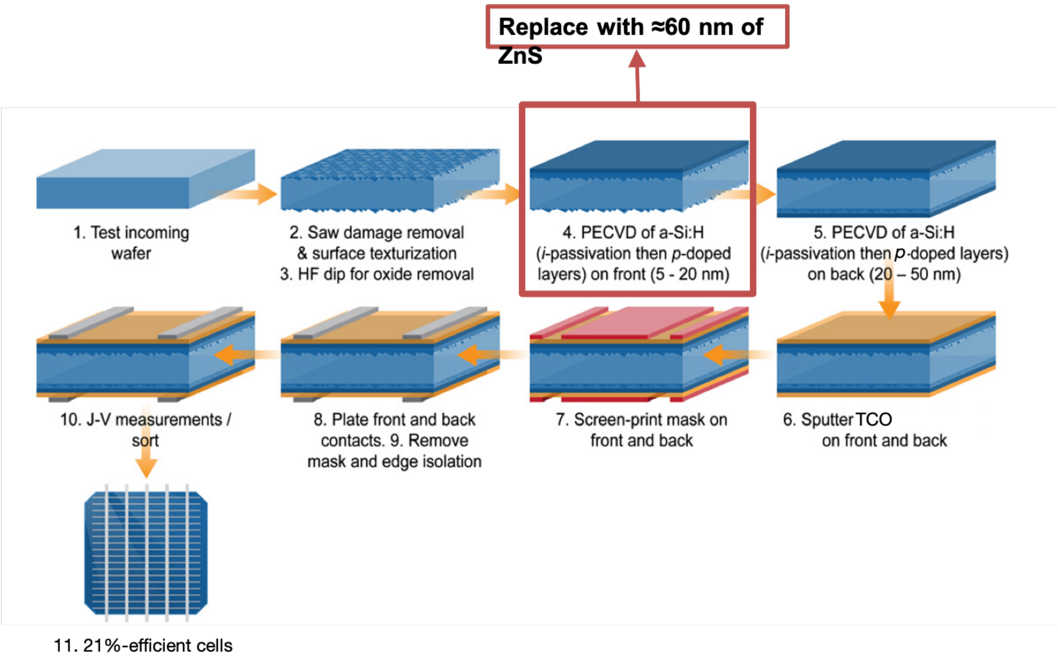

Figure 6.3: Adaptation of silicon heterojunction fabrication for ZnS carrier-selective front contact. Starting at upper left, steps are grouped as follows: 1. Test incoming wafer, 2.+3. Saw damage removal & surface texturization and HF dip for oxide removal, 4. ALD deposition of ZnS instead of PECVD of a-Si:H (i-passivation then p-doped layers on front), 5. PECVD of a-Si:H (i-passivation then p-doped layers on back), 6. sputter TCO on front and back, 7. screen-print mask on front and back, 8. + 9. plate front and back contact and remove mask and edge isolation, 10. J-V measurements/sort, 11. resulting 21%-efficient cells.

absolute efficiency increase from the p-tye SHJ device reference to the champion $\mathrm{ZnS_xSe_{1-x}}$ device, this corresponds to about \$0.09/W savings at the utility scale.

Chapter 7

GROWTH OF 2D II-VI SEMICONDUCTOR LAYERS BY HYBRID LAMINATION

7.1 Introduction to 2D II-VI Semiconductor Layers

The unique physics present in 2D layered materials gained enormous interest after the discovery of graphene in 2004. New phenomena have been observed and the different-from-bulk materials properties of thin layers promise use in an array of applications, such as taking advantage of increased absorbance or bandgap tunability with stacking to design 2D photovoltaic devices. In particular, it has been shown that the electronic and optical properties of Zn-based chalcogenides can be manipulated with dimension. Colloidal quantum dots, 1D quantum ribbons, wires, rods, and belts exhibit quantum confinement effects, opening an extended phase space for material tunability. Parallel to graphene and other 2D-layered materials, the zinc blende phase of Zn-chalcogenides incorporates a hexagonal symmetry easily viewed in the (110) plane. Unlike many other graphene analogues, the Zn-based chalcogenides can not be easily exfoliated to 2D slabs. The layers are held to together by strong covalent bonds rather than weaker van der Walls bonds featured in materials like MoS_2 or InSe. The underlying honeycomb lattice featured in graphene and graphene analogues of interest lead to interesting physics with applications for 2D versions of field effect transistors, memory, light emitting diodes, biosensors, and photovoltaic devices. Huang, Li, and Sun ([44], [45]) developed a new technique for creating atomic slabs of 2D II-VI materials where layers of II-VI crystals are held together by organic species, which makes exfoliation via sonication possible, after which the organic species can be evaporated away to produce freestanding sheets. These layers have improved mobility compared to their bulk counterparts, as well as expanded bandgap tunability based on number and type of different layers. Without any vacuum steps, their fabrication is simply scaled through the use of larger reaction vessels.

7.2 Fundamentals of Hybrid Lamination

The first challenge of fabricating 2D layers in materials whose planes of interest are held together by covalent bonds is to reduce the energetic barrier required to separate the layers. Huang and Li achieved this in many II-VI semiconductors by introducing an organic molecule during crystal growth in solvothermal reactions [45]. The reaction temperature and time were varied to optimize for the output of the desired phase. In this work, the reaction of interest was fabricating double-layer 2D-[(Zn_2Se_2)(pa)] from zinc source $Zn(NO_3)_2 \cdot 6\, H_2O$ selenium powder, and propylamine (pa).

$$Zn^{2+} + Se + pa \longrightarrow [Zn_2Se_2(pa)] \tag{7.1}$$

In this work, 2.66 mmol $Zn(NO_3)_2 \cdot 6\, H_2O$, 1.33 mmol Se, and 10 mL n-propylamine were mixed in the teflon liner of a 45-mL Parr 4744 General Purpose Acid Digestion Bomb. Huang and Li found that [(Zn_2Se_2)(L)] compounds (L = organic species) were obtained when materials were reacted at temperatures from 120°C-150°C [45]. At higher temperature bulk ZnSe became the major product, while at lower temperature only single-layered [(ZnSe)(pa)] phases formed. As such, the materials were heated to 140°C for 5 days in accordance with protocols specified in Huang and Li [45]. After allowing the reaction vessel to cool, the materials were removed with and washed in 30% ethanol solution in a Büchner funnel connected to an aspirator pump. The products were further washed in the funnel with 80% ethanol and dried with anhydrous ethyl ether. X-ray diffraction spectra of the [(Zn_2Se_2)(pa)] powder products confirmed the presence of ZnSe layers with 1.5 nm separation, as expected for [(Zn_2Se_2)(pa)]. An example is shown in Fig. 7.1The higher angle peaks are consistent with orthorhombic *Pbca* crystallization.

7.3 Free-standing II-VI Layers

While the lamellar hybrid [(Zn_2Se_2)(pa)] system has applications in its own right, the achievement of free-standing II-VI layers opens up even more possibilities. With the weaker bonding between II-VI planes enabled by the organic ligands, separation of the layers can be accomplished simply through sonication in solvent. In a typical preparation, 20–50 mg[(Zn_2Se_2)(pa)] product was mixed with ethanol (1 mL ethanol per 1 mg [(Zn_2Se_2)(pa)]), then sonicated for 4 hours. Single layers of ZnSe-pa were selected by centrifuging the resulting mixture for 40 min and 500 rpm and collected the top three-fourths of the resulting dispersion by pipette, with the expectation and clear result that larger stacks were left in the bottom of the tube. This dispersion was then heated at 140°C for two or more hours until the solvent and propylamine were volatilized. In some cases, this product collection occurred directly on a substrate (glass, silicon wafer) with an aim to concentrate the resulting Zn_2Se_2 layers onto the desired location. In other cases, the product was collected, dispersed into ethanol at a concentration of 0.3 mg/mL, spun coat onto a silicon substrate, and the solvent

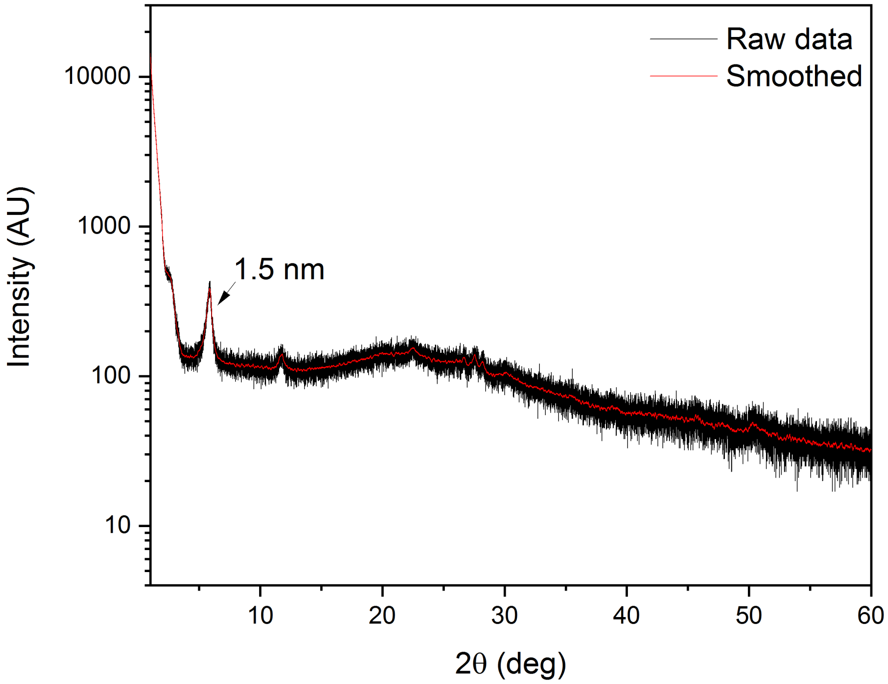

Figure 7.1: X-ray diffraction spectra from 2θ-ω scan on [(Zn_2Se_2)(pa)]. Black line is raw data. Red line is smoothed data. Peak near 6° corresponds to [(Zn_2Se_2)(pa)] layer spacing.

again removed via heat treatment.

7.4 Band Alignment

Energy band alignment measurements of differently structured Zn_2Se_2 on silicon were performed using the same procedure outlined in Chapter 4. Figure 7.2 shows the Zn 2p core level shifting with increasing thickness, and Fig. 7.3 shows the valence band signal shift with increasing thickness. In conjunction with the small shift in Si 2p core level position from substrate bulk to interface, a valence band offset of 1.7 eV is found, where the Zn_2Se_2 valence band is at a higher energy than the Si valence band. The so-called Type III broken-gap heterojunction is shown in Fig. 7.4. The conduction band offset is based on an assumed 3.5 eV Zn_2Se_2 band gap.

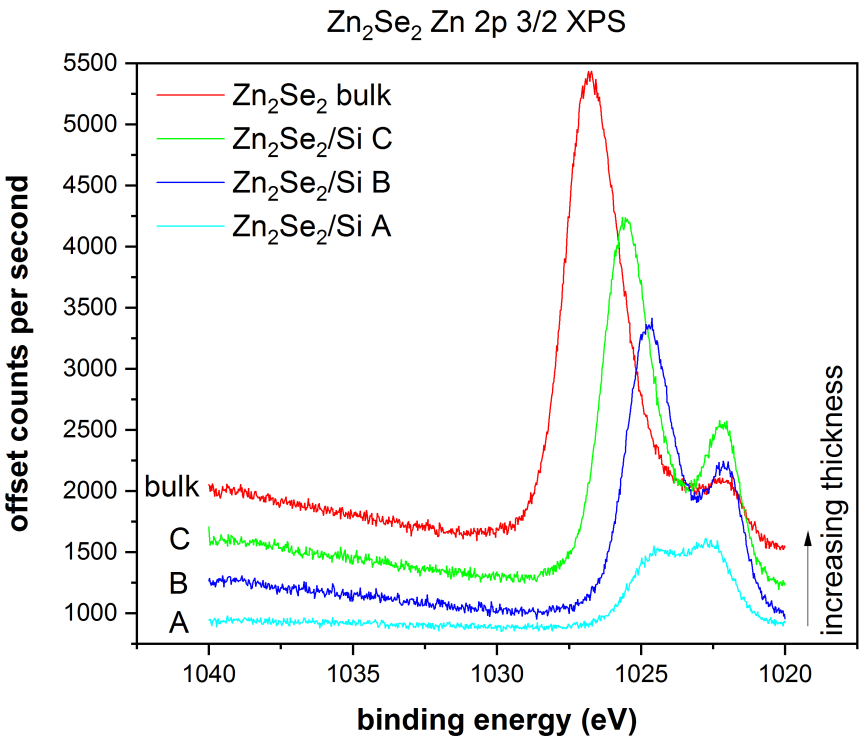

Figure 7.2: Offset Zn 2p 3/2 core level XPS spectra of varied thickness Zn_2Se_2 on Si. From the bulk Zn_2Se_2 spectra (top, red) to the thinnest Zn_2Se_2 layer (bottom, cyan), the primary Zn 2p 3/2 core level line shifts to lower binding energy, indicative of a $\approx$ 2 eV valence band shift towards higher potential energy.

7.5 Future Work

The color of the powder product at different stages of processing changed from tan to red, red-orange, brick, or even black. XRD, transmission, and reflectance spectra were similar between differently-colored powder products at the $[(Zn_2Se_2)(pa)]$ stage, and a lighter color could be reattained with extended heat treatment on a hot plate or mechanical disruption of powder clumps. The inside of a clump was usually lighter in color than the outside, similarly to clumps of unmixed cocoa powder in water or milk. This suggests the color is dependent on water or ethanol content, and more vigorous agitation during washing and a longer drying process should be explored for fully repeatable and consistent intermediate products.

Transmission and reflectance spectra were taken by Megan Phelan in a Cary 5000 UV/Vis/NIR Spectrometer with Integrating Sphere. Transmission spectra are

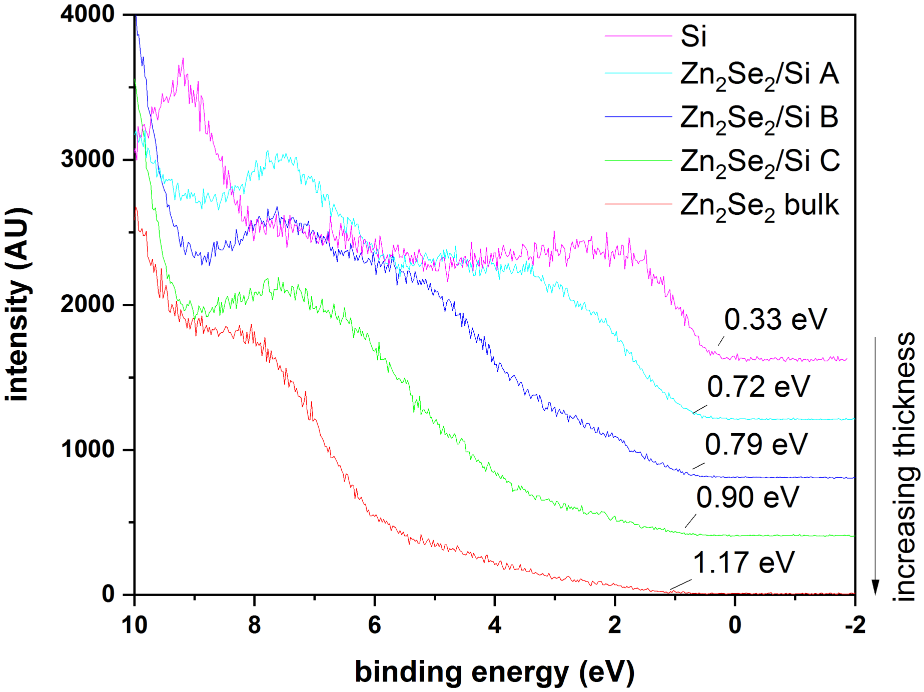

Figure 7.3: Offset XPS valence band spectra of Si with layers of differently structured Zn_2Se_2. Valence band maximum binding energy is labeled for each sample: bare Si (top, pink) at 0.33 eV, interfacial samples of Zn_2Se_2 of increasing thickness (cyan, blue, and green) at 0.72 eV, 0.79 eV, and 0.90 eV, and bulk Zn_2Se_2 (bottom, red) at 1.17 eV.

shown in Fig. 7.8. Reflectance spectra are show in Fig. 7.9. Samples 1–3 are of [(Zn_2Se_2)(pa)], with a and b denoting different spots on the same powder sample. Sample 4 is Zn_2Se_2. Positions a and b on each powder are not the same between transmission and reflectance spectra. The differences in spectra within the same powder sample are similar to the differences between [(Zn_2Se_2)(pa)] of different colors, namely % transmission or reflectance rather than overall shape, suggesting the key factor is thickness rather than composition. The Zn_2Se_2 spectra (4a, 4b) lack the reflectance dip between 800–900 nm present in the [(Zn_2Se_2)(pa)] samples. The samples were not sufficiently uniform or thick for meaningful absorbance measurements.

Raman spectra were acquired on Zn_2Se_2 on c-Si substrates with the assistance of Cora Went in a Renishaw M1000 Micro Raman Spectrometer System. When deposited onto c-Si via spin coating and solvent evaporation, the Zn_2Se_2 is prone

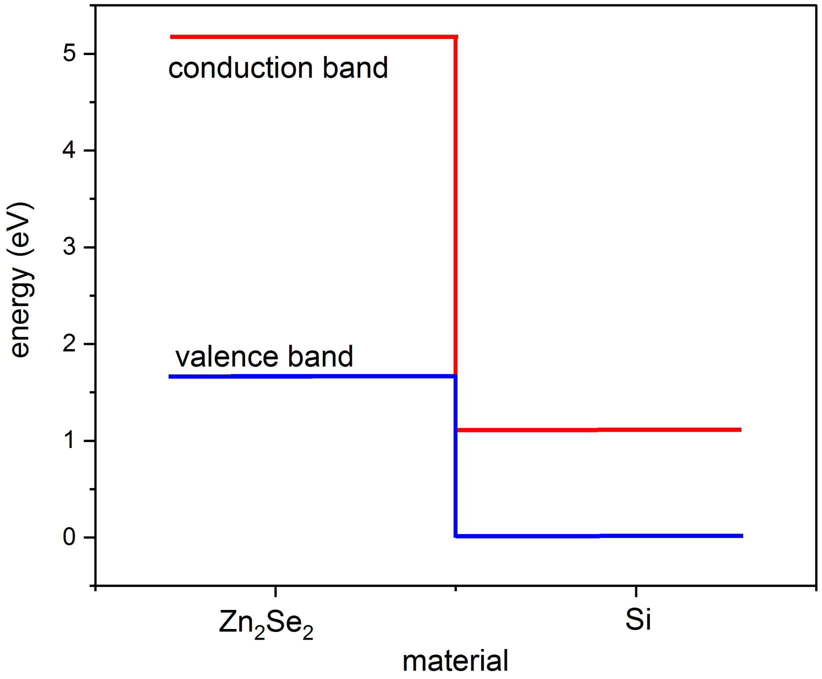

Figure 7.4: Illustration of energy band offsets of Zn$_2$Se$_2$ on c-Si. The red line (top) corresponds to the conduction band minimum of each material, and the blue line (bottom) to the valence band maximum.

to the coffee ring effect, where most of the material concentrates along the edge of the last solvent to evaporate. Thus, the material is not uniformly distributed. Raman spectra were acquired at different spots on such a sample and the variation in features demonstrates the non-uniform composition of the fully processed Zn$_2$Se$_2$. Fig. 7.11 includes spectra from a reference Si wafer and three different spots on a Zn$_2$Se$_2$/Si sample, labelled A, B, and C from top to bottom. The Si calibration spectra (bottom, blue) provides the Si reference peak around 520 cm^{-1}. Spectra A (black) and B (red) were taken while focused on larger Zn$_2$Se$_2$ material, easily visible to the naked eye (see Fig. 7.12). These spectra both have clear peaks around 250 cm^{-1}, consistent with the first longitudinal optical phonon (1LO) band of bulk ZnSe. Position A has additional features between 400 cm^{-1}and 600 cm^{-1}, overlapping with the Si peak. The broader contribution is interpreted as mainly due to the 2LO band from bulk ZnSe. Spectrum C (green) was taken away from the clumped material, where thinner deposition remained. The Si signal is clearly visible at 520 cm^{-1}, consistent with a focus closer to the substrate in an area without

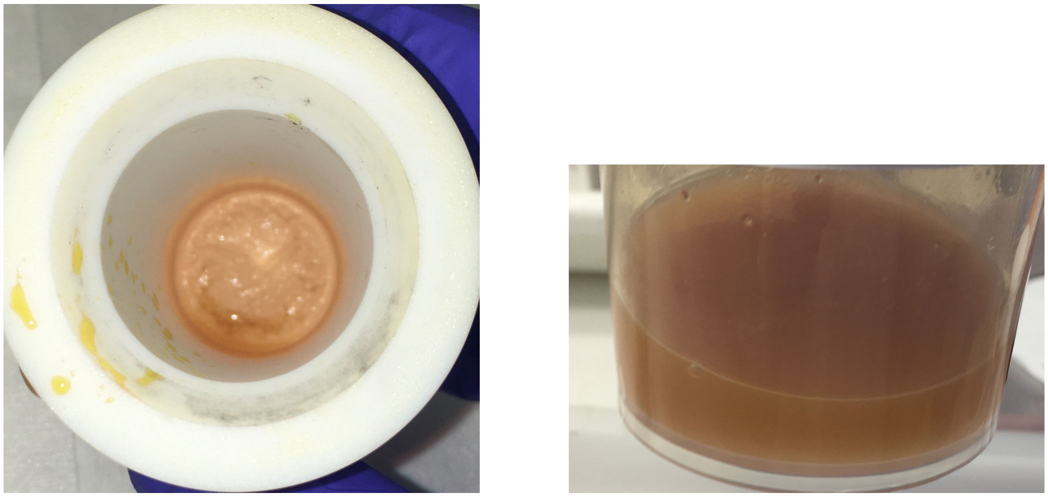

(a) Tan $[(Zn_2Se_2)(pa)]$ product in reaction vessel liner

(b) Tan product in ethanol immediately after collection

(c) Red product in ethanol immediately after collection

(d) Darkened product in ethanol $\approx$ 10 min after collection

Figure 7.5: Intermediate lamellar hybrid $[(Zn_2Se_2)(pa)]$ reaction product before completion of washing and drying. When reaction vessel is opened, excess reactants are poured off, and (a) tan powder product in reaction vessel liner remains. Powder product is collected by washing reaction vessel in 30% ethanol, which may appear as (b) tan product in solution or (c) red product in solution. While product is transported to washing station (Büchner funnel assembly), color may darken from (b) to (d) over a matter of minutes.

complete coverage. The additional broad feature around 900 cm^{-1} to 1000 cm^{-1} is interpreted as the contribution from the Zn_2Se_2, and suggests a facile test for desired product of Zn_2Se_2. The Raman spectra show that while steps were taken to isolate the differently-structured freestanding Zn_2Se_2 slabs in accordance with previous work, the same preferential production and collection was not achieved.

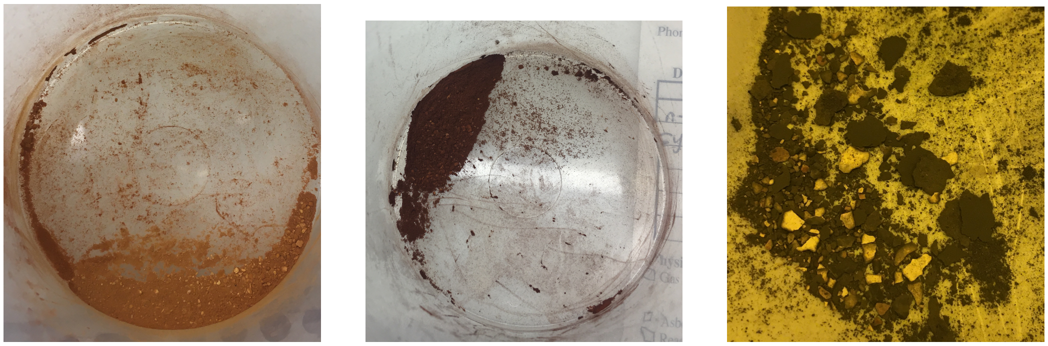

(a) Orange [(Zn_2Se_2)(pa)] (b) Red [(Zn_2Se_2)(pa)] (c) Black [(Zn_2Se_2)(pa)]

Figure 7.6: Representative intermediate lamellar hybrid [(Zn_2Se_2)(pa)] products after washing and drying, showing variation in color with reaction run. (a) Powder product orange in color, with lighter tan flecks visible. (b) Powder product uniformly red in color. (c) Powder product primarily black in color, with light tan and red flake-shaped aggregations a few millimeters in diameter.

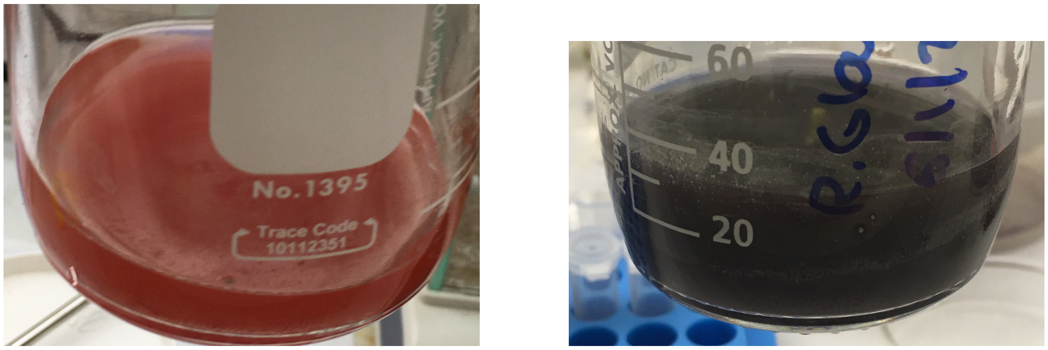

(a) [(Zn_2Se_2)(pa)] in ethanol before exfoliation. (b) [(Zn_2Se_2)(pa)] in ethanol after exfoliation.

Figure 7.7: [(Zn_2Se_2)(pa)] products in ethanol before (a, red) and after (b, black) exfoliation.

7.6 Conclusions

The initial interest in this work, as with the rest of this thesis, was in potential application to photovoltaic devices. However, given the large Type III broken-gap heterojunction of Zn_2Se_2 on Si and associated charge transport via band-to-band quantum tunneling, this heterostructure may prove more useful in designing new high-speed switching devices. Regardless of application, further work must be undertaken towards reproducibility and desired yield that other researchers have reported. Scalable, low-temperature, vacuum-free solution processing is possible but by no means straightforward. Efforts towards this end are likely not to be funded with photovoltaic applications in mind given the tight profit margins of photovoltaic

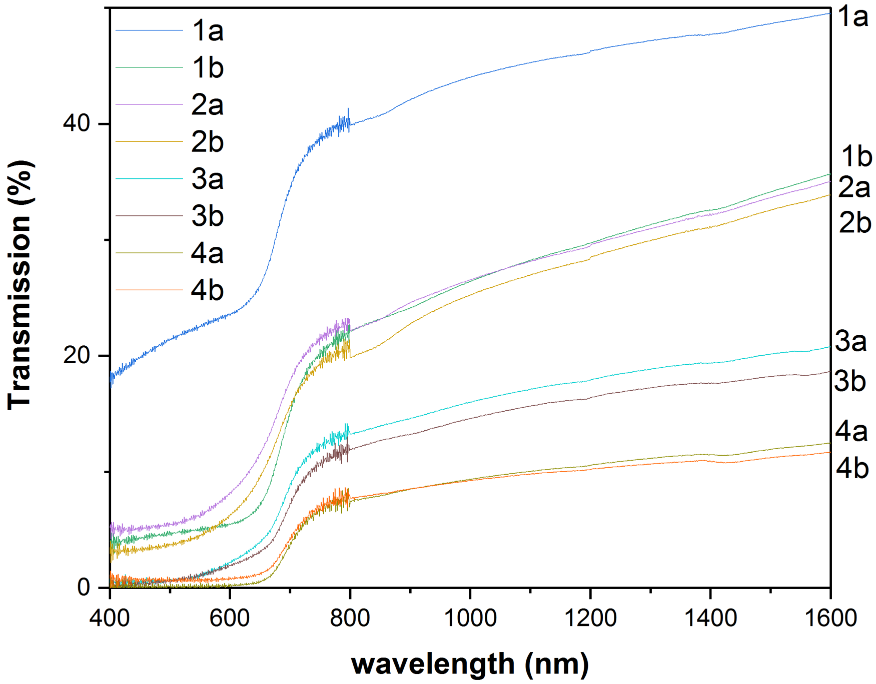

Figure 7.8: Transmission spectra of $[(Zn_2Se_2)(pa)]$ and Zn_2Se_2 powders mounted with double-sided tape on a glass slide.

device production, where well-established technologies perform near their efficiency limits. The design space of lamellar hybrid or freestanding differently-structured Zn-chalcogenide systems, either as heterojunctions on bulk crystal substrates or alternating layers maintain their promise for device applications with the space for more growth, such as photocatalysis for liquid fuels. Material study in this field requires a more thorough optimization of the fabrication, preferably enabled by deeper experience in solvothermal synthesis and scalable wet chemistry techniques.

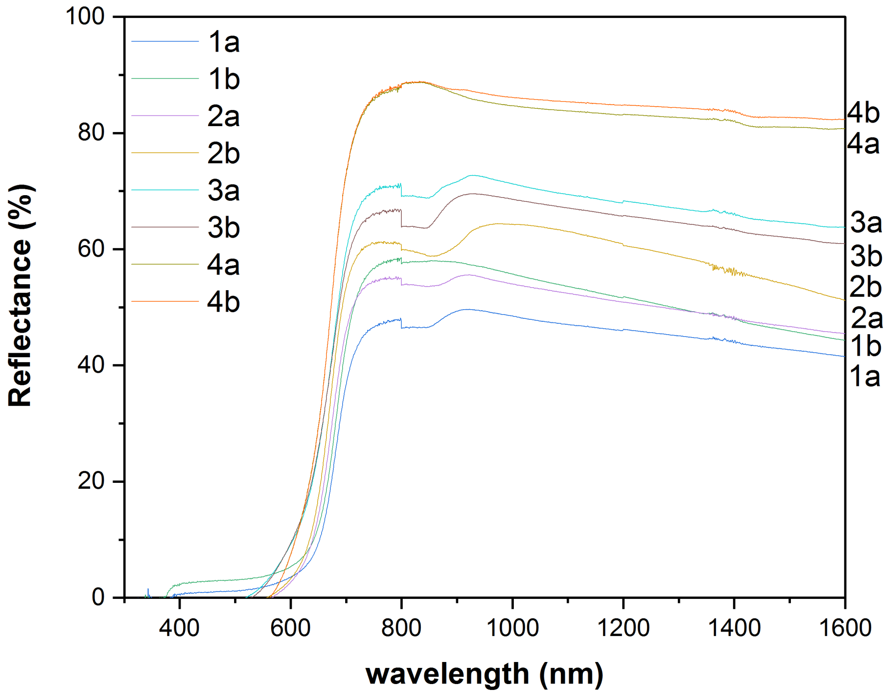

Figure 7.9: Diffuse reflectance spectra of [(Zn_2Se_2)(pa)] and Zn_2Se_2 powders mounted with double-sided tape on a glass slide.

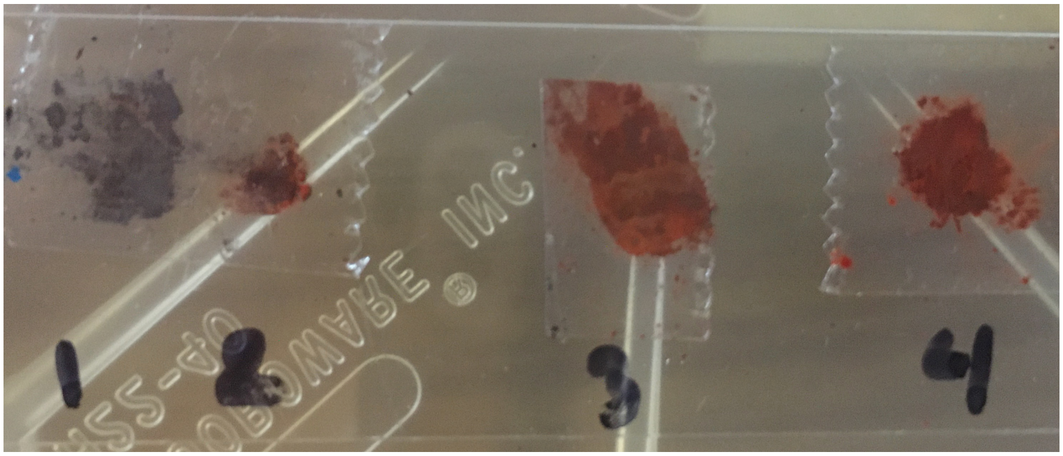

Figure 7.10: Image of samples 1–4, from left to right, represented in transmission and diffuse reflectance spectra.

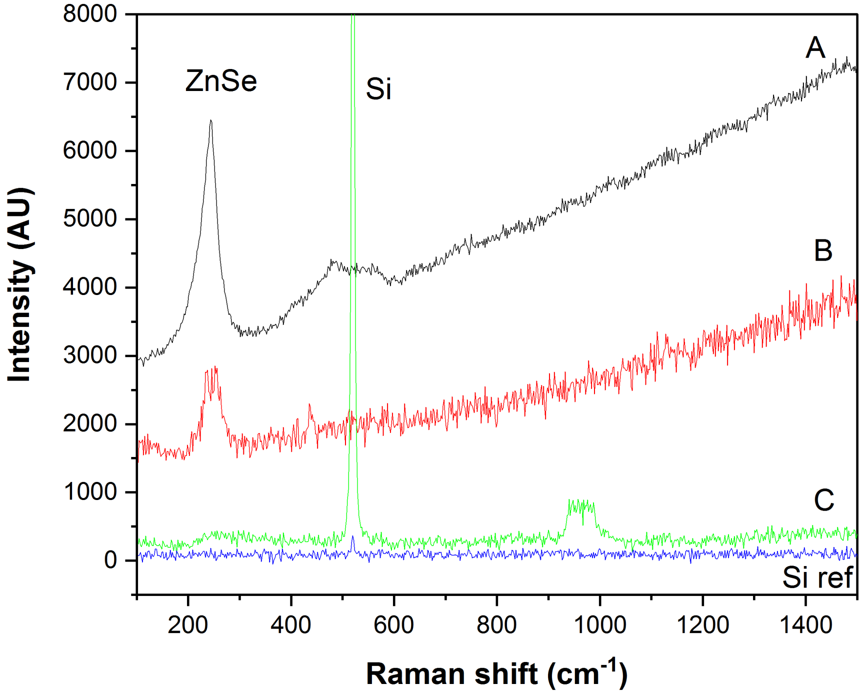

Figure 7.11: Raman spectra of different locations on Zn_2Se_2/Si sample (A-C) and silicon reference spectra (bottom).

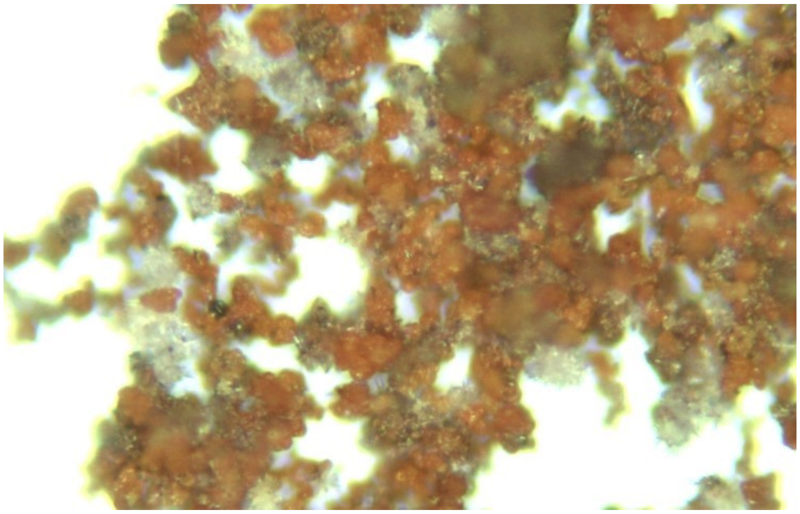

Figure 7.12: Zn_2Se_2 on Si at location (B) at 50× magnification.

Chapter 8

FINAL REMARKS

The goal of this work was to improve photovoltaic devices through novel interface designs. We considered that state-of-the-art photovoltaic devices experience addressable losses in the contacting layers required for charge collection, and that alternatives can be designed with production costs in mind. We identified $\mathrm{ZnS_xSe_{1-x}}$ thin films and $\mathrm{Zn_2Se_2}$ sheets as candidates for a carrier-selective contact on a silicon heterojunction devices. We selected several materials as possibilities for epitaxy- and vacuum-free passivants and selective contacts for GaAs photovoltaic devices. We determined that the band energetics and bonding states at heterointerfaces play a key role in device performance, and that a thorough understanding of the impact of the interface on the whole should guide material choice in photovoltaic device design.

Our first goal was to determine the band alignment between the conduction bands and valence bands of potential carrier-selective contacts and their underlying substrate. This was done by fabricating $\mathrm{ZnS_xSe_{1-x}}$ alloys for x from 0 to 1 through compound-source molecular beam deposition, where the mole fraction x was varied by changing the ZnS and ZnSe compound source temperatures. Additionally, $\mathrm{Zn_2Se_2}$ sheets were fabricated by solvothermal methods in an acid digestion bomb, dispersed in solvent, then coated onto Si substrates. Contacts on GaAs were made through spin coating and thermal evaporation. We employed high-resolution x-ray photoelectron spectroscopy to determine the energy band alignment for each heterojunction pair via the Kraut method. From these measurements, we were able to screen candidates as potential electron selective contacts, hole selective contacts, or neither.

Our second goal was to determine what balance of optoelectronic properties variable through choice in $\mathrm{ZnS_xSe_{1-x}}$ mole fraction, thickness, and donor concentration was the best electron selective front contact for a silicon heterojunction photovoltaic device. This was achieved by modeling a full photovoltaic devices in Sentaurus TCAD and simulating their performance under standard conditions, and comparing them to analogous SHJ devices with standard ITO/a-Si front contacts. We found that a 62-nm thick degenerately doped (N_D = $4.5\times10^{19}\mathrm{cm^{-3}}$) ZnS contact was the champion II-VI carrier selective contact, with absorption gains as the deciding factor between alternative mole fraction materials at high dopant densities. The champion simulated device outperformed a comparable experimental device with an improved short-circuit current and open-circuit voltage, but its lower fill factor led to a lower efficiency than the reference SHJ in simulation.

For epitaxy-free GaAs photovoltaic devices, band alignment measurements have identified several candidates for electron and hole selective contacts. Further, high resolution x-ray photoelectron spectroscopy studies of GaAs-passivation layer bonding states showed that the GaAs surface can be passivated in the presence of Ga^{1+} oxide, leading to carrier lifetimes of 300 ns or more, stable under heating upto 200°C.

Free-standing sheets of differently-structured II-VI semiconductors were studied as candidates for solution-processable carrier-selective contacts, where optoelectronic properties can be tuned with layer number and stacking partners. High-resolution x-ray photoelectron spectroscopy measurements of Zn_2Se_2 on c-Si showed a type III broken-gap band alignment, with the Zn_2Se_2 valence band above the c-Si conduction band, appropriate for a hole-selective contact in a photovoltaic device or for other electronics applications.

Further work needs to be done to develop reliable Ohmic contacts on ZnS, and to investigate industry-compatible non-equilibrium growth methods for heavily n-type doped ZnS to enable incorporation of the proposed ZnS electron-selective contact into manufactured silicon heterojunction devices.

BIBLIOGRAPHY

[1] R. Perez and M. Perez, "A fundamental look at supply side energy reserves for the planet," *Int. Energy Agency SHC Program. Sol. Updat*, vol. 62, pp. 4–6, 2015.

[2] E. A. Wrigley, "Energy and the english industrial revolution," *Philosophical Transactions of the Royal Society A: Mathematical, Physical and Engineering Sciences*, vol. 371, no. 1986, p. 20 110 568, Mar. 13, 2013. DOI: `10.1098/rsta.2011.0568`.

[3] J.-P. Bocquet-Appel, "When the world's population took off: The springboard of the neolithic demographic transition," *Science*, vol. 333, no. 6042, pp. 560–561, Jul. 29, 2011. DOI: `10.1126/science.1208880`.

[4] O. C. Kopp, *Coal*, in *Encyclopedia Britannica*, Feb. 18, 2022.

[5] T. Savery, *{The Miner's Friend: Or, an Engine to Raise Water by Fire}*. London: S. Crouch, 1827, 72 pp.

[6] D. C. Sands, C. E. Morris, E. A. Dratz, and A. L. Pilgeram, "Elevating optimal human nutrition to a central goal of plant breeding and production of plant-based foods," *Plant Science*, vol. 177, no. 5, pp. 377–389, Nov. 2009. DOI: `10.1016/j.plantsci.2009.07.011`.

[7] J. H. O'Keefe and L. Cordain, "Cardiovascular disease resulting from a diet and lifestyle at odds with our paleolithic genome: How to become a 21st-century hunter-gatherer," *Mayo Clinic Proceedings*, vol. 79, no. 1, pp. 101–108, Jan. 2004, ISSN: 00256196. DOI: `10.4065/79.1.101`. [Online]. Available: `https://linkinghub.elsevier.com/retrieve/pii/S002561961163262X` (visited on 04/24/2022).

[8] V. S. Peterson, "{Sex matters: A queer history of hierarchies}," *International Feminist Journal of Politics*, vol. 16, no. 3, pp. 389–409, Jul. 3, 2014. DOI: `10.1080/14616742.2014.913384`.

[9] J. Diamond, "The worst mistake in the history of the human race," *Discover Magazine*, pp. 64–66, May 1, 1999.

[10] J. Komlos and H. Küchenhoff, "The diminution of the physical stature of the english male population in the eighteenth century," *Cliometrica*, vol. 6, no. 1, pp. 45–62, Jan. 2012. DOI: `10.1007/s11698-011-0070-7`.

[11] M. R. Hannah Ritchie and P. Rosado, "Energy," *Our World in Data*, 2020, https://ourworldindata.org/energy.

[12] "State of the climate: Monthly global climate report for annual 2020," NOAA National Centers for Environmental Information, Jan. 2021.

[13] K. Yoshikawa, H. Kawasaki, W. Yoshida, *et al.*, "Silicon heterojunction solar cell with interdigitated back contacts for a photoconversion efficiency over 26%," *Nature Energy*, vol. 2, no. 5, p. 17 032, May 2017. doi: `10.1038/nenergy.2017.32`.

[14] Z. C. Holman, A. Descoeudres, L. Barraud, *et al.*, "Current losses at the front of silicon heterojunction solar cells," *IEEE Journal of Photovoltaics*, vol. 2, no. 1, pp. 7–15, Jan. 2012. doi: `10.1109/JPHOTOV.2011.2174967`.

[15] M. A. Woodhouse, B. Smith, A. Ramdas, and R. M. Margolis, "Crystalline silicon photovoltaic module manufacturing costs and sustainable pricing: 1h 2018 benchmark and cost reduction road map," NREL/TP-6A20-72134, 1495719, Feb. 15, 2019, NREL/TP–6A20–72 134, 1 495 719. doi: `10.2172/1495719`.

[16] K. Ohkawa, A. Tsujimura, T. Nishikawa, *et al.*, "Compound source molecular beam epitaxy for II–VI laser structures," *Journal of Crystal Growth*, vol. 159, no. 1, pp. 632–635, Feb. 1996. doi: `10.1016/0022-0248(95)00828-4`.

[17] A. A. Akl, S. A. Aly, and H. Howari, "Structural characterisation and optical properties of annealed ZnSSe thin films," *CHALCOGENIDE LETTERS*, vol. 13, no. 6, pp. 247–255, Jun. 2016, Place: ATOMISTILOR STR 105 BIS, PO BOX MG-7, BUCHAREST-MAGURELE, 077125, ROMANIA Publisher: NATL INST R&D MATERIALS PHYSICS Type: Article, issn: 1584-8663.

[18] H. K. Sadekar, A. V. Ghule, and R. Sharma, "Bandgap engineering by substitution of s by se in nanostructured ZnS1xSex thin films grown by soft chemical route for nontoxic optoelectronic device applications," *Journal of Alloys and Compounds*, vol. 509, no. 18, pp. 5525–5531, May 2011. doi: `10.1016/j.jallcom.2011.02.089`.

[19] R. G. Kaufman and P. Dowbor, "Mechanism of formation of ohmic contacts to ZnSe, ZnS, and mixed crystals ZnS $_X$ se $_{1\ X}$," *Journal of Applied Physics*, vol. 45, no. 10, pp. 4487–4490, Oct. 1974. doi: `10.1063/1.1663075`.

[20] J. P. Bosco, S. B. Demers, G. M. Kimball, N. S. Lewis, and H. A. Atwater, "Band alignment of epitaxial ZnS/zn$_3$p$_2$ heterojunctions," *Journal of Applied Physics*, vol. 112, no. 9, p. 093 703, Nov. 2012. doi: `10.1063/1.4759280`.

[21] M. A. Herman and H. Sitter, *Molecular beam epitaxy: Fundamentals and current status*, ser. Springer series in materials science v. 7. Berlin ; New York: Springer-Verlag, 1989, 382 pp.

[22] Collaboration: Authors and editors of the volumes III/17B-22A-41B, "Zinc sulfide (ZnS) vapor pressure, heat of vaporization," in *II-VI and I-VII Compounds; Semimagnetic Compounds*, O. Madelung, U. Rössler, and M. Schulz, Eds., vol. 41B, Series Title: Landolt-Börnstein - Group III

Condensed Matter, Berlin/Heidelberg: Springer-Verlag, 1999, pp. 1–5. DOI: `10.1007/10681719_411`.

[23] K. Madiomanana, M. Bahri, J. Rodriguez, *et al.*, "Silicon surface preparation for III-v molecular beam epitaxy," *Journal of Crystal Growth*, vol. 413, pp. 17–24, Mar. 2015. DOI: `10.1016/j.jcrysgro.2014.12.004`.

[24] A. Augusto, J. Karas, P. Balaji, S. G. Bowden, and R. R. King, "Exploring the practical efficiency limit of silicon solar cells using thin solar-grade substrates," *Journal of Materials Chemistry A*, vol. 8, no. 32, pp. 16 599–16 608, 2020. DOI: `10.1039/D0TA04575F`.

[25] P. Balaji, W. J. Dauksher, S. G. Bowden, and A. Augusto, "Improving surface passivation on very thin substrates for high efficiency silicon heterojunction solar cells," *Solar Energy Materials and Solar Cells*, vol. 216, p. 110 715, Oct. 2020. DOI: `10.1016/j.solmat.2020.110715`.

[26] P. F. Fewster, *X-ray scattering from semiconductors*, 2nd ed. River Edge, NJ: Imperial College Press, 2003, 299 pp.

[27] A. Ichimiya and P. I. Cohen, *Reflection high-energy electron diffraction*. Cambridge, U.K. ; New York: Cambridge University Press, 2004, 353 pp., OCLC: ocm54529276.

[28] M. Renninger, "\"Umweganregung", eine bisher unbeachtete Wechselwirkungserscheinung bei Raumgitterinterferenzen," *Zeitschrift fr Physik*, vol. 106, no. 3, pp. 141–176, Mar. 1937. DOI: `10.1007/BF01340315`.

[29] J. Bosco, F. Tajdar, and H. Atwater, "Molecular beam epitaxy of n-type ZnS: A wide band gap emitter for heterojunction PV devices," in *2012 38th IEEE Photovoltaic Specialists Conference*, Austin, TX, USA: IEEE, Jun. 2012, pp. 002 513–002 517. DOI: `10.1109/PVSC.2012.6318105`.

[30] O. Palais and A. Arcari, "Contactless measurement of bulk lifetime and surface recombination velocity in silicon wafers," *Journal of Applied Physics*, vol. 93, no. 8, pp. 4686–4690, Apr. 15, 2003. DOI: `10.1063/1.1562741`.

[31] C. Fujihira, M. Morin, H. Hashizume, J. Friedt, Y. Nakai, and M. Hirose, "Carrier lifetime measurements by microwave photoconductive decay method at low injection levels," *Japanese Journal of Applied Physics*, vol. 32, pp. L1362–L1364, Part 2, No. 9B Sep. 15, 1993. DOI: `10.1143/JJAP.32.L1362`.

[32] E. A. Kraut, R. W. Grant, J. R. Waldrop, and S. P. Kowalczyk, "Precise determination of the valence-band edge in X-ray photoemission spectra: Application to measurement of semiconductor interface potentials," *Physical Review Letters*, vol. 44, no. 24, pp. 1620–1623, Jun. 16, 1980. DOI: `10.1103/PhysRevLett.44.1620`.

[33] G. Major, D. Shah, T. Avval, V. Fernandez, N. Fairley, and M. Linford, “Advanced Line Shapes in X-ray Photoelectron Spectroscopy II. The Finite Lorentzian (LF) Line Shape (with some MATLAB code illustrating the use of the subplot function),” vol. 21, pp. 35–39, Apr. 2020.

[34] L. Feng, L.-d. Zhang, H. Liu, *et al.*, “Characterization study of native oxides on GaAs(100) surface by XPS,” presented at the ISPDI 2013 - Fifth International Symposium on Photoelectronic Detection and Imaging, B. Chang and H. Guo, Eds., Beijing, China, Aug. 16, 2013, 89120N. DOI: `10.1117/12.2033679`.

[35] C. L. Hinkle, M. Milojevic, B. Brennan, *et al.*, “Detection of ga suboxides and their impact on III-v passivation and fermi-level pinning,” *Applied Physics Letters*, vol. 94, no. 16, p. 162 101, Apr. 20, 2009. DOI: `10.1063/1.3120546`.

[36] G. H. Major, N. Fairley, P. M. A. Sherwood, *et al.*, “Practical guide for curve fitting in X-ray photoelectron spectroscopy,” *Journal of Vacuum Science & Technology A*, vol. 38, no. 6, p. 061 203, Dec. 2020, ISSN: 0734-2101, 1520-8559. DOI: `10.1116/6.0000377`. [Online]. Available: `http://avs.scitation.org/doi/10.1116/6.0000377` (visited on 06/02/2022).

[37] Y. Hinuma, A. Grüneis, G. Kresse, and F. Oba, “Band alignment of semiconductors from density-functional theory and many-body perturbation theory,” *Physical Review B*, vol. 90, no. 15, Oct. 3, 2014. DOI: `10.1103/PhysRevB.90.155405`.

[38] R. L. Anderson, “Germanium-gallium arsenide heterojunctions [letter to the editor],” *IBM Journal of Research and Development*, vol. 4, no. 3, pp. 283–287, 1960, Publisher: IBM. DOI: `10.1147/rd.43.0283`.

[39] *Sentaurus Device User Guide Version R-2020.09*, Sep. 2020.

[40] A. Kanevce and W. K. Metzger, “The role of amorphous silicon and tunneling in heterojunction with intrinsic thin layer (HIT) solar cells,” *Journal of Applied Physics*, vol. 105, no. 9, p. 094 507, May 2009. DOI: `10.1063/1.3106642`.

[41] A. Onno, C. Chen, P. Koswatta, M. Boccard, and Z. C. Holman, “Passivation, conductivity, and selectivity in solar cell contacts: Concepts and simulations based on a unified partial-resistances framework,” *Journal of Applied Physics*, vol. 126, no. 18, p. 183 103, Nov. 14, 2019. DOI: `10.1063/1.5117201`.

[42] M. A. Green, “Solar cell fill factors: General graph and empirical expressions,” *Solid-State Electronics*, vol. 24, no. 8, pp. 788–789, Aug. 1981. DOI: `10.1016/0038-1101(81)90062-9`.

[43] G. Mao, M. W. Bench, Z.-M. Qiu, and X. Sun, “Novel wet etching agent for II-VI semiconductors and method,” European pat. 2502263A2, Sep. 26, 2012.

[44] Y. Sun, Z. Sun, S. Gao, *et al.*, "Fabrication of flexible and freestanding zinc chalcogenide single layers," *Nature Communications*, vol. 3, no. 1, p. 1057, Jan. 2012. DOI: `10.1038/ncomms2066`.

[45] X. Huang and J. Li, "From single to multiple atomic layers: A unique approach to the systematic tuning of structures and properties of inorganicorganic hybrid nanostructured semiconductors," *Journal of the American Chemical Society*, vol. 129, no. 11, pp. 3157–3162, Mar. 2007. DOI: `10.1021/ja065799e`.

FURTHER READING

[46] T. E. Cook, C. C. Fulton, W. J. Mecouch, R. F. Davis, G. Lucovsky, and R. J. Nemanich, "Band offset measurements of the GaN (0001)/HfO2 interface," *Journal of Applied Physics*, vol. 94, no. 11, pp. 7155–7158, Dec. 2003. DOI: `10.1063/1.1625579`.

[47] B. Brar, R. Stczinhoff, A. Seabaugh, X. Zhou, S. Jiang, and W. P. Kirk, "Band offset measurement of the ZnS/Si(001) heterojunction," p. 4,

[48] J. Leiro, M. Heinonen, T. Laiho, and I. Batirev, "Core-level XPS spectra of fullerene, highly oriented pyrolitic graphite, and glassy carbon," *Journal of Electron Spectroscopy and Related Phenomena*, vol. 128, no. 2, pp. 205–213, Feb. 2003. DOI: `10.1016/S0368-2048(02)00284-0`.

[49] G. Kresse and J. Furthmüller, "Efficiency of ab-initio total energy calculations for metals and semiconductors using a plane-wave basis set," *Computational Materials Science*, vol. 6, no. 1, pp. 15–50, Jul. 1996. DOI: `10.1016/0927-0256(96)00008-0`.

[50] H. Matsuura, T. Okuno, H. Okushi, and K. Tanaka, "Electrical properties of *n*-amorphous/ *p*-crystalline silicon heterojunctions," *Journal of Applied Physics*, vol. 55, no. 4, pp. 1012–1019, Feb. 15, 1984. DOI: `10.1063/1.333193`.

[51] S. Hu, M. H. Richter, M. F. Lichterman, *et al.*, "Electrical, photoelectrochemical, and photoelectron spectroscopic investigation of the interfacial transport and energetics of amorphous TiO_2 /Si heterojunctions," *The Journal of Physical Chemistry C*, vol. 120, no. 6, pp. 3117–3129, Feb. 18, 2016. DOI: `10.1021/acs.jpcc.5b09121`.

[52] S. Pookpanratana, K. Goetz, E. Bittle, *et al.*, "Electronic properties and structure of single crystal perylene," *Organic Electronics*, vol. 61, pp. 157–163, Oct. 2018. DOI: `10.1016/j.orgel.2018.05.035`.

[53] R. Saive, H. Emmer, C. T. Chen, and H. Atwater, "GaP/Si heterojunction solar cells: Band alignment study by X-ray photo electron spectroscopy and cross-sectional kelvin probe force microscopy," p. 5,

[54] J. P. Perdew, K. Burke, and M. Ernzerhof, "Generalized gradient approximation made simple," *Physical Review Letters*, vol. 77, no. 18, pp. 3865–3868, Oct. 28, 1996. DOI: `10.1103/PhysRevLett.77.3865`.

[55] A. Franciosi, "Heterojunction band offset engineering," *Surface Science Reports*, vol. 25, no. 1, pp. 1–140, 1996. DOI: `10.1016/0167-5729(95)00008-9`.

[56] D. A. Shirley, “High-resolution X-ray photoemission spectrum of the valence bands of gold,” *Physical Review B*, vol. 5, no. 12, pp. 4709–4714, Jun. 15, 1972. DOI: `10.1103/PhysRevB.5.4709`.

[57] J. R. Waldrop and R. W. Grant, “Measurement of AlN/GaN (0001) heterojunction band offsets by x-ray photoemission spectroscopy,” *Applied Physics Letters*, vol. 68, no. 20, pp. 2879–2881, May 13, 1996. DOI: `10.1063/1.116355`.

[58] D. C. Gleason-Rohrer, B. S. Brunschwig, and N. S. Lewis, “Measurement of the band bending and surface dipole at chemically functionalized Si(111)/vacuum interfaces,” *The Journal of Physical Chemistry C*, vol. 117, no. 35, pp. 18 031–18 042, Sep. 5, 2013. DOI: `10.1021/jp401585s`.

[59] J. Uhlrich, L. Grabow, M. Mavrikakis, and T. Kuech, “Practical surface treatments and surface chemistry of n-type and p-type GaN,” *Journal of Electronic Materials*, vol. 37, no. 4, pp. 439–447, Apr. 2008. DOI: `10.1007/s11664-007-0348-5`.

[60] E. A. Kraut, R. W. Grant, J. R. Waldrop, and S. P. Kowalczyk, “Semiconductor core-level to valence-band maximum binding-energy differences: Precise determination by X-ray photoelectron spectroscopy,” *Physical Review B*, vol. 28, no. 4, pp. 1965–1977, Aug. 15, 1983. DOI: `10.1103/PhysRevB.28.1965`.

[61] R. Saive, H. Emmer, C. T. Chen, C. Zhang, C. Honsberg, and H. Atwater, “Study of the interface in a GaP/Si heterojunction solar cell,” *IEEE Journal of Photovoltaics*, vol. 8, no. 6, pp. 1568–1576, Nov. 2018. DOI: `10.1109/JPHOTOV.2018.2861724`.

[62] L. Ley, R. A. Pollak, F. R. McFeely, S. P. Kowalczyk, and D. A. Shirley, “Total valence-band densities of states of III-v and II-VI compounds from X-ray photoemission spectroscopy,” *Physical Review B*, vol. 9, no. 2, pp. 600–621, Jan. 15, 1974. DOI: `10.1103/PhysRevB.9.600`.

[63] C. Maierhofer, “Valence band offset in ZnS layers on Si(111) grown by molecular beam epitaxy,” *Journal of Vacuum Science & Technology B: Microelectronics and Nanometer Structures*, vol. 9, no. 4, p. 2238, Jul. 1991. DOI: `10.1116/1.585727`.

[64] G. Greczynski and L. Hultman, “X-ray photoelectron spectroscopy: Towards reliable binding energy referencing,” *Progress in Materials Science*, vol. 107, p. 100 591, Jan. 2020. DOI: `10.1016/j.pmatsci.2019.100591`.

[65] E. A. Skryleva, Y. N. Parkhomenko, I. M. Karnaukh, E. A. Zhukova, A. R. Karaeva, and V. Z. Mordkovich, “XPS characterization of MWCNT and C_{60} -based composites,” *Fullerenes, Nanotubes and Carbon Nanostructures*, vol. 24, no. 8, pp. 535–540, Aug. 2, 2016. DOI: `10.1080/1536383X.2016.1197910`.

[66] S. Turishchev, O. Chuvenkova, E. Parinova, *et al.*, "XPS investigations of MOCVD tin oxide thin layers on Si nanowires array," *Results in Physics*, vol. 11, pp. 507–509, Dec. 2018. DOI: `10.1016/j.rinp.2018.09.046`.

[67] G. Silversmit, D. Depla, H. Poelman, G. B. Marin, and R. De Gryse, "An XPS study on the surface reduction of V2O5(001) induced by ar+ ion bombardment," *Surface Science*, vol. 600, no. 17, pp. 3512–3517, Sep. 2006. DOI: `10.1016/j.susc.2006.07.006`.

[68] G. Coulston, E. Thompson, and N. Herron, "Characterization of VPO catalysts by X-ray photoelectron spectroscopy," *Journal of Catalysis*, vol. 163, no. 1, pp. 122–129, Sep. 1996. DOI: `10.1006/jcat.1996.0311`.

[69] R. A. Sinton and A. Cuevas, "Contactless determination of current–voltage characteristics and minority-carrier lifetimes in semiconductors from quasi-steady-state photoconductance data," *Applied Physics Letters*, vol. 69, no. 17, pp. 2510–2512, Oct. 21, 1996. DOI: `10.1063/1.117723`.

[70] D. Prakash, A. Aboraia, M. El-Hagary, E. Shaaban, and K. Verma, "Determination of the optical constants and film thickness of ZnTe and ZnS thin films in terms of spectrophotometric and spectroscopic ellipsometry," *Ceramics International*, vol. 42, no. 2, pp. 2676–2685, Feb. 2016. DOI: `10.1016/j.ceramint.2015.10.096`.

[71] G. Silversmit, D. Depla, H. Poelman, G. B. Marin, and R. De Gryse, "Determination of the V2p XPS binding energies for different vanadium oxidation states (V5+ to V0+)," *Journal of Electron Spectroscopy and Related Phenomena*, vol. 135, no. 2, pp. 167–175, Apr. 2004. DOI: `10.1016/j.elspec.2004.03.004`.

[72] L. T. Romano, R. D. Bringans, X. Zhou, and W. P. Kirk, "Interface structure of ZnS/Si(001) and comparison with ZnSe/Si(001) and GaAs/Si(001)," *Physical Review B*, vol. 52, no. 15, pp. 11 201–11 205, Oct. 15, 1995. DOI: `10.1103/PhysRevB.52.11201`.

[73] F. d. Groot, "Multiplet effects in X-ray spectroscopy," *Coordination Chemistry Reviews*, vol. 249, no. 1, pp. 31–63, Jan. 2005. DOI: `10.1016/j.ccr.2004.03.018`.

[74] M. C. Biesinger, L. W. Lau, A. R. Gerson, and R. S. Smart, "Resolving surface chemical states in XPS analysis of first row transition metals, oxides and hydroxides: Sc, Ti, V, Cu and Zn," *Applied Surface Science*, vol. 257, no. 3, pp. 887–898, Nov. 2010. DOI: `10.1016/j.apsusc.2010.07.086`.

[75] R. Zimmermann, R. Claessen, F. Reinert, P. Steiner, and S. Hüfner, "Strong hybridization in vanadium oxides: Evidence from photoemission and absorption spectroscopy," *Journal of Physics: Condensed Matter*, vol. 10, no. 25, pp. 5697–5716, Jun. 29, 1998. DOI: `10.1088/0953-8984/10/25/018`.

[76] M. Labrune, "Silicon surface passivation and epitaxial growth on c-Si by low temperature plasma processes for high efficiency solar cells," p. 229,

[77] E. Yablonovitch, D. L. Allara, C. C. Chang, T. Gmitter, and T. B. Bright, "Unusually low surface-recombination velocity on silicon and germanium surfaces," *Physical Review Letters*, vol. 57, no. 2, pp. 249–252, Jul. 14, 1986. DOI: `10.1103/PhysRevLett.57.249`.

[78] T. Orent, "Electrical characteristics of zinc sulfide thin films deposited by various methods," *Journal of The Electrochemical Society*, vol. 141, no. 5, p. 1320, 1994. DOI: `10.1149/1.2054917`.

[79] Y. Chuan-Zheng, H. Jian-Min, and P. Guang-Wen, "Brief introduction of X-ray multiple diffraction," vol. 17, no. 1, p. 12, 2000.

[80] P. Zaumseil, "High-resolution characterization of the forbidden Si 200 and Si 222 reflections," *Journal of Applied Crystallography*, vol. 48, no. 2, pp. 528–532, Apr. 1, 2015. DOI: `10.1107/S1600576715004732`.

[81] S. Andrieu and P. Fréchard, "What information can be obtained by RHEED applied on polycrystalline films?" *Surface Science*, vol. 360, no. 1, pp. 289–296, Jul. 1996. DOI: `10.1016/0039-6028(96)00303-2`.

[82] N. Arora, J. Hauser, and D. Roulston, "Electron and hole mobilities in silicon as a function of concentration and temperature," *IEEE Transactions on Electron Devices*, vol. 29, no. 2, pp. 292–295, Feb. 1982. DOI: `10.1109/T-ED.1982.20698`.

[83] M. Aven, "High electron mobility in zinc selenide through low-temperature annealing," *Journal of Applied Physics*, vol. 42, no. 3, pp. 1204–1208, Mar. 1971. DOI: `10.1063/1.1660167`.

[84] J. R. Haynes and W. Shockley, "The mobility and life of injected holes and electrons in germanium," *Physical Review*, vol. 81, no. 5, pp. 835–843, Mar. 1, 1951. DOI: `10.1103/PhysRev.81.835`.

[85] H. E. Ruda, "Theoretical study of hole transport in ZnSe," *Journal of Applied Physics*, vol. 59, no. 10, pp. 3516–3526, May 15, 1986. DOI: `10.1063/1.337041`.

[86] J. Waldmeyer, "A contactless method for determination of carrier lifetime, surface recombination velocity, and diffusion constant in semiconductors," *Journal of Applied Physics*, vol. 63, no. 6, pp. 1977–1983, Mar. 15, 1988. DOI: `10.1063/1.341097`.

[87] L. Sirleto, A. Irace, G. Vitale, L. Zeni, and A. Cutolo, "All-optical multi-wavelength technique for the simultaneous measurement of bulk recombination lifetimes and front/rear surface recombination velocity in single crystal silicon samples," *Journal of Applied Physics*, vol. 93, no. 6, pp. 3407–3413, Mar. 15, 2003. DOI: `10.1063/1.1556567`.

[88] H. Yang and P. H. Holloway, "Efficient and photostable ZnS-passivated CdS:Mn luminescent nanocrystals," *Advanced Functional Materials*, vol. 14, no. 2, pp. 152–156, Feb. 2004. DOI: `10.1002/adfm.200305011`.

[89] G. Bahir, V. Ariel, V. Garber, D. Rosenfeld, and A. Sher, "Electrical properties of epitaxially grown CdTe passivation for long-wavelength HgCdTe photodiodes," *Applied Physics Letters*, vol. 65, no. 21, pp. 2725–2727, Nov. 21, 1994. DOI: `10.1063/1.112548`.

[90] J. K. White, C. A. Musca, H. C. Lee, and L. Faraone, "Hydrogenation of ZnS passivation on narrow-band gap HgCdTe," *Applied Physics Letters*, vol. 76, no. 17, pp. 2448–2450, Apr. 24, 2000. DOI: `10.1063/1.126372`.

[91] A. Descoeudres, L. Barraud, S. De Wolf, *et al.*, "Improved amorphous/crystalline silicon interface passivation by hydrogen plasma treatment," *Applied Physics Letters*, vol. 99, no. 12, p. 123 506, Sep. 19, 2011. DOI: `10.1063/1.3641899`.

[92] S. Deb and B. R. Nag, "Measurement of lifetime of carriers in semiconductors through microwave reflection," *Journal of Applied Physics*, vol. 33, no. 4, pp. 1604–1604, Apr. 1962. DOI: `10.1063/1.1728779`.

[93] J. Schmidt, R. Peibst, and R. Brendel, "Surface passivation of crystalline silicon solar cells: Present and future," *Solar Energy Materials and Solar Cells*, vol. 187, pp. 39–54, Dec. 2018. DOI: `10.1016/j.solmat.2018.06.047`.

[94] K. Banerjee, J. Huang, S. Ghosh, *et al.*, "Surface study of thioacetamide and zinc sulfide passivated long wavelength infrared type-II strained layer superlattice," presented at the SPIE Defense, Security, and Sensing, B. F. Andresen, G. F. Fulop, and P. R. Norton, Eds., Orlando, Florida, United States, May 13, 2011, p. 801 243. DOI: `10.1117/12.900198`.

[95] J. Geissbühler, J. Werner, S. Martin de Nicolas, *et al.*, "22.5% efficient silicon heterojunction solar cell with molybdenum oxide hole collector," *Applied Physics Letters*, vol. 107, no. 8, p. 081 601, Aug. 24, 2015. DOI: `10.1063/1.4928747`.

[96] E. Yablonovitch, O. D. Miller, and S. R. Kurtz, "A great solar cell also needs to be a great LED: External fluorescence leads to new efficiency record," presented at the Nobel Symposium 153: Nanoscale Energy Converters, Orenas Castle, Sweden, 2013, pp. 9–11. DOI: `10.1063/1.4794698`.

[97] A. Froitzheim, R. Stangl, L. Elmer, *et al.*, "AFORS-HET: A computer-program for the simulation of hetero-junction solar cells to be distributed for public use," p. 4,

[98] J. I. Pankove and M. L. Tarng, "Amorphous silicon as a passivant for crystalline silicon," *Applied Physics Letters*, vol. 34, no. 2, pp. 156–157, Jan. 15, 1979. DOI: `10.1063/1.90711`.

[99] M. Taguchi, H. Sakata, Y. Yoshimine, *et al.*, "An approach for the higher efficiency in the HIT cells," in *Conference Record of the Thirty-first IEEE Photovoltaic Specialists Conference, 2005.*, Lake buena Vista, FL, USA: IEEE, 2005, pp. 866–871. DOI: `10.1109/PVSC.2005.1488270`.

[100] E. Centurioni and D. Iencinella, "Role of front contact work function on amorphous silicon/crystalline silicon heterojunction solar cell performance," *IEEE Electron Device Letters*, vol. 24, no. 3, pp. 177–179, Mar. 2003. DOI: `10.1109/LED.2003.811405`.

[101] U. Wurfel, A. Cuevas, and P. Wurfel, "Charge carrier separation in solar cells," *IEEE Journal of Photovoltaics*, vol. 5, no. 1, pp. 461–469, Jan. 2015. DOI: `10.1109/JPHOTOV.2014.2363550`.

[102] Q. Wang, M. Page, E. Iwaniczko, *et al.*, "Crystal silicon heterojunction solar cells by hot-wire CVD," in *2008 33rd IEEE Photovolatic Specialists Conference*, San Diego, CA, USA: IEEE, May 2008, pp. 1–5. DOI: `10.1109/PVSC.2008.4922448`.

[103] R. Stangl, M. Schmidt, and H.-M.-I. Berlin, "Design criteria for amorphouscrystalline silicon heterojuction solar cells - a simulation study," p. 4,

[104] W. Shockley and H. J. Queisser, "Detailed balance limit of efficiency of p-n junction solar cells," p. 11,

[105] K. Ghosh, C. J. Tracy, B. Dauksher, S. Herasimenka, C. Honsberg, and S. Bowden, "Determination of charged state density at the interface between amorphous silicon and crystalline silicon by lateral conductance measurement," p. 4,

[106] T. Mishima, M. Taguchi, H. Sakata, and E. Maruyama, "Development status of high-efficiency HIT solar cells," *Solar Energy Materials and Solar Cells*, vol. 95, no. 1, pp. 18–21, Jan. 2011. DOI: `10.1016/j.solmat.2010.04.030`.

[107] C.-Y. Wei, C.-H. Lin, H.-T. Hsiao, P.-C. Yang, C.-M. Wang, and Y.-C. Pan, "Efficiency improvement of HIT solar cells on p-type Si wafers," *Materials*, vol. 6, no. 11, pp. 5440–5446, Nov. 22, 2013. DOI: `10.3390/ma6115440`.

[108] A. Onno, C. Chen, and Z. C. Holman, "Electron and hole partial specific resistances: A framework to understand contacts to solar cells," in *2019 IEEE 46th Photovoltaic Specialists Conference (PVSC)*, Chicago, IL, USA: IEEE, Jun. 2019, pp. 2329–2333. DOI: `10.1109/PVSC40753.2019.8980762`.

[109] L. C. Hirst and N. J. Ekins-Daukes, "Fundamental losses in solar cells," *Progress in Photovoltaics: Research and Applications*, vol. 19, no. 3, pp. 286–293, May 2011. DOI: `10.1002/pip.1024`.

[110] J. Wong, D. Jariwala, G. Tagliabue, *et al.*, "High photovoltaic quantum efficiency in ultrathin van der waals heterostructures," *ACS Nano*, vol. 11, no. 7, pp. 7230–7240, Jul. 25, 2017. DOI: `10.1021/acsnano.7b03148`.

[111] "HIT$^{\text{TM}}$ cells-high-efficiency crystalline Si cells with novel structure," p. 11, 1999.

[112] Z. C. Holman, M. Filipic, A. Descoeudres, *et al.*, "Infrared light management in high-efficiency silicon heterojunction and rear-passivated solar cells," *Journal of Applied Physics*, vol. 113, no. 1, p. 013 107, Jan. 7, 2013. DOI: `10.1063/1.4772975`.

[113] F. Wang, Y. Gao, Z. Pang, L. Yang, and J. Yang, "Insights into the role of the interface defects density and the bandgap of the back surface field for efficient p-type silicon heterojunction solar cells," *RSC Advances*, vol. 7, no. 43, pp. 26 776–26 782, 2017. DOI: `10.1039/C7RA04018K`.

[114] R. Varache, C. Leendertz, M. Gueunier-Farret, J. Haschke, D. Muñoz, and L. Korte, "Investigation of selective junctions using a newly developed tunnel current model for solar cell applications," *Solar Energy Materials and Solar Cells*, vol. 141, pp. 14–23, Oct. 2015. DOI: `10.1016/j.solmat.2015.05.014`.

[115] B. M. Kayes, H. A. Atwater, and N. S. Lewis, "Comparison of the device physics principles of planar and radial p-n junction nanorod solar cells," *Journal of Applied Physics*, vol. 97, no. 11, p. 114 302, Jun. 2005. DOI: `10.1063/1.1901835`.

[116] T. Tiedje, E. Yablonovitch, G. Cody, and B. Brooks, "Limiting efficiency of silicon solar cells," *IEEE Transactions on Electron Devices*, vol. 31, no. 5, pp. 711–716, May 1984. DOI: `10.1109/T-ED.1984.21594`.

[117] M. Green, "Limits on the open-circuit voltage and efficiency of silicon solar cells imposed by intrinsic auger processes," *IEEE Transactions on Electron Devices*, vol. 31, no. 5, pp. 671–678, May 1984. DOI: `10.1109/T-ED.1984.21588`.

[118] A. Cuevas and D. Yan, "Misconceptions and misnomers in solar cells," *IEEE Journal of Photovoltaics*, vol. 3, no. 2, pp. 916–923, Apr. 2013. DOI: `10.1109/JPHOTOV.2013.2238289`.

[119] P. Luppina, S. Bowden, P. Lugli, and S. M. Goodnick, "Modeling of a gallium phosphide/silicon heterojunction solar cells," in *2016 IEEE 43rd Photovoltaic Specialists Conference (PVSC)*, Portland, OR, USA: IEEE, Jun. 2016, pp. 2467–2472. DOI: `10.1109/PVSC.2016.7750087`.

[120] P. Luppina, P. Lugli, and S. M. Goodnick, "Modeling of silicon heterojunction solar cells," in *2015 IEEE 42nd Photovoltaic Specialist Conference (PVSC)*, New Orleans, LA: IEEE, Jun. 2015, pp. 1–6. DOI: `10.1109/PVSC.2015.7356049`.

[121] A. L. Gray, M. Stan, T. Varghese, *et al.*, "Multi-terminal dual junction InGaP2/GaAs solar cells for hybrid system," in *2008 33rd IEEE Photovolatic Specialists Conference*, San Diego, CA, USA: IEEE, May 2008, pp. 1–4. DOI: `10.1109/PVSC.2008.4922575`.

[122] H. Ramli, S. K. A. Rahim, T. A. Rahim, and M. M. Aminuddin, "Optimization of zinc sulfide (ZnS) electron affinity in copper indium sulfide (CIS) based photovoltaic cell," p. 7,

[123] L. Zhao, H. Li, C. Zhou, H. Diao, and W. Wang, "Optimized resistivity of p-type Si substrate for HIT solar cell with al back surface field by computer simulation," *Solar Energy*, vol. 83, no. 6, pp. 812–816, Jun. 2009. DOI: `10.1016/j.solener.2008.11.007`.

[124] C. R. Bukowsky, J. Grandidier, K. T. Fountaine, D. M. Callahan, B. J. Stanbery, and H. A. Atwater, "Photon and carrier management design for nonplanar thin-film copper indium gallium selenide photovoltaics," *Solar Energy Materials and Solar Cells*, vol. 161, pp. 149–156, Mar. 2017. DOI: `10.1016/j.solmat.2016.11.008`.

[125] M. A. Green, "Radiative efficiency of state-of-the-art photovoltaic cells: Radiative efficiency of photovoltaic cells," *Progress in Photovoltaics: Research and Applications*, vol. 20, no. 4, pp. 472–476, Jun. 2012. DOI: `10.1002/pip.1147`.

[126] A. Richter, M. Hermle, and S. W. Glunz, "Reassessment of the limiting efficiency for crystalline silicon solar cells," *IEEE Journal of Photovoltaics*, vol. 3, no. 4, pp. 1184–1191, Oct. 2013. DOI: `10.1109/JPHOTOV.2013.2270351`.

[127] S. V. Boriskina, M. A. Green, K. Catchpole, *et al.*, "Roadmap on optical energy conversion," *Journal of Optics*, vol. 18, no. 7, p. 073 004, Jul. 1, 2016. DOI: `10.1088/2040-8978/18/7/073004`.

[128] Y. Hayashi, D. Li, A. Ogura, and Y. Ohshita, "Role of i-aSi:h layers in aSi:h/cSi heterojunction solar cells," *IEEE Journal of Photovoltaics*, vol. 3, no. 4, pp. 1149–1155, Oct. 2013. DOI: `10.1109/JPHOTOV.2013.2274616`.

[129] Z. Yu, M. Leilaeioun, and Z. Holman, "Selecting tandem partners for silicon solar cells," *Nature Energy*, vol. 1, no. 11, p. 16 137, Nov. 2016. DOI: `10.1038/nenergy.2016.137`.

[130] V. A. Dao, J. Heo, H. Choi, *et al.*, "Simulation and study of the influence of the buffer intrinsic layer, back-surface field, densities of interface defects, resistivity of p-type silicon substrate and transparent conductive oxide on heterojunction with intrinsic thin-layer (HIT) solar cell," *Solar Energy*, vol. 84, no. 5, pp. 777–783, May 2010. DOI: `10.1016/j.solener.2010.01.029`.

[131] N. Dwivedi, S. Kumar, A. Bisht, K. Patel, and S. Sudhakar, “Simulation approach for optimization of device structure and thickness of HIT solar cells to achieve 27% efficiency,” *Solar Energy*, vol. 88, pp. 31–41, Feb. 2013. DOI: `10.1016/j.solener.2012.11.008`.

[132] W. Lisheng, C. Fengxiang, and A. Yu, “Simulation of high efficiency heterojunction solar cells with AFORS-HET,” *Journal of Physics: Conference Series*, vol. 276, p. 012 177, Feb. 1, 2011. DOI: `10.1088/1742-6596/276/1/012177`.

[133] W. Shockley and W. T. Read, “Statistics of the recombinations of holes and electrons,” *Physical Review*, vol. 87, no. 5, pp. 835–842, Sep. 1, 1952. DOI: `10.1103/PhysRev.87.835`.

[134] I. Almansouri, A. Ho-Baillie, S. P. Bremner, and M. A. Green, “Supercharging silicon solar cell performance by means of multijunction concept,” *IEEE Journal of Photovoltaics*, vol. 5, no. 3, pp. 968–976, May 2015. DOI: `10.1109/JPHOTOV.2015.2395140`.

[135] H. Liu, Z. Ren, Z. Liu, A. G. Aberle, T. Buonassisi, and I. M. Peters, “The realistic energy yield potential of GaAs-on-si tandem solar cells: A theoretical case study,” *Optics Express*, vol. 23, no. 7, A382, Apr. 6, 2015. DOI: `10.1364/OE.23.00A382`.

[136] D. Bahro, M. Koppitz, A. Mertens, K. Glaser, J. Mescher, and A. Colsmann, “Understanding the external quantum efficiency of organic homo-tandem solar cells utilizing a three-terminal device architecture,” *Advanced Energy Materials*, vol. 5, no. 22, p. 1 501 019, Nov. 2015. DOI: `10.1002/aenm.201501019`.

[137] D. Jariwala, A. R. Davoyan, J. Wong, and H. A. Atwater, “Van der waals materials for atomically-thin photovoltaics: Promise and outlook,” *ACS Photonics*, vol. 4, no. 12, pp. 2962–2970, Dec. 20, 2017. DOI: `10.1021/acsphotonics.7b01103`.

[138] G. Landis, J. Loferski, R. Beaulieu, *et al.*, “Wide-bandgap epitaxial heterojunction windows for silicon solar cells,” *IEEE Transactions on Electron Devices*, vol. 37, no. 2, pp. 372–381, Feb. 1990. DOI: `10.1109/16.46369`.

[139] D. L. Young, W. Nemeth, S. Grover, *et al.*, “Carrier selective, passivated contacts for high efficiency silicon solar cells based on transparent conducting oxides,” *Energy Procedia*, vol. 55, pp. 733–740, 2014. DOI: `10.1016/j.egypro.2014.08.053`.

[140] A. Polman, M. Knight, E. C. Garnett, B. Ehrler, and W. C. Sinke, “Photovoltaic materials: Present efficiencies and future challenges,” *Science*, vol. 352, no. 6283, aad4424–aad4424, Apr. 15, 2016. DOI: `10.1126/science.aad4424`.

[141] A. Cuevas, “The recombination parameter j0,” *Energy Procedia*, vol. 55, pp. 53–62, 2014. DOI: `10.1016/j.egypro.2014.08.073`.

[142] M. Maeder, A. Ramírez, and A. Zehe, “A RHEED study of as-received and atomically clean silicon surfaces in UHV-environment,” p. 3, 1999.

[143] C. Fulk, R. Sporken, J. Dumont, *et al.*, “Arsenic deposition as a precursor layer on silicon (211) and (311) surfaces,” *Journal of Electronic Materials*, vol. 34, no. 6, pp. 846–850, Jun. 2005. DOI: `10.1007/s11664-005-0030-8`.

[144] H. Okumura, “Comparison of conventional surface cleaning methods for Si molecular beam epitaxy,” *Journal of The Electrochemical Society*, vol. 144, no. 11, p. 3765, 1997. DOI: `10.1149/1.1838088`.

[145] M. Jaime-Vasquez, R. N. Jacobs, J. D. Benson, *et al.*, “Evaluation of surface cleaning of si(211) for molecular-beam epitaxy deposition of infrared detectors,” *Journal of Electronic Materials*, vol. 39, no. 7, pp. 951–957, Jul. 2010. DOI: `10.1007/s11664-010-1152-1`.

[146] T. Ohmi, T. Ichikawa, T. Shibata, K. Matsudo, and H. Iwabuchi, “Substrate-surface cleaning for very low temperature silicon epitaxy by low-kinetic-energy particle bombardment,” *Applied Physics Letters*, vol. 53, no. 1, pp. 45–47, Jul. 4, 1988. DOI: `10.1063/1.100121`.

[147] A. Ishizaka, “Low temperature surface cleaning of silicon and its application to silicon MBE,” *Journal of The Electrochemical Society*, vol. 133, no. 4, p. 666, 1986. DOI: `10.1149/1.2108651`.

[148] E. Sacher and A. Yelon, “Comment on “mechanism of HF etching of silicon surfaces: A theoretical understanding of hydrogen passivation”,” *Physical Review Letters*, vol. 66, no. 12, pp. 1647–1647, Mar. 25, 1991. DOI: `10.1103/PhysRevLett.66.1647`.

[149] G. W. Trucks, K. Raghavachari, G. S. Higashi, and Y. J. Chabal, “Trucks *et al*. reply,” *Physical Review Letters*, vol. 66, no. 12, pp. 1648–1648, Mar. 25, 1991. DOI: `10.1103/PhysRevLett.66.1648`.

[150] G. W. Trucks, K. Raghavachari, G. S. Higashi, and Y. J. Chabal, “Mechanism of HF etching of silicon surfaces: A theoretical understanding of hydrogen passivation,” *Physical Review Letters*, vol. 65, no. 4, pp. 504–507, Jul. 23, 1990. DOI: `10.1103/PhysRevLett.65.504`.

[151] D. J. Chadi and J. R. Chelikowsky, “Step-formation energies and domain orientations at Si(111) surfaces,” *Physical Review B*, vol. 24, no. 8, pp. 4892–4895, Oct. 15, 1981. DOI: `10.1103/PhysRevB.24.4892`.

[152] C. Fulk, S. Sivananthan, D. Zavitz, *et al.*, “The structure of the Si (211) surface,” *Journal of Electronic Materials*, vol. 35, no. 6, pp. 1449–1454, Jun. 2006. DOI: `10.1007/s11664-006-0282-y`.

[153] D. J. Chadi, “Theoretical study of the atomic structure of silicon (211), (311), and (331) surfaces,” *Physical Review B*, vol. 29, no. 2, pp. 785–792, Jan. 15, 1984. DOI: `10.1103/PhysRevB.29.785`.

[154] K. A. Horowitz, R. Fu, T. Silverman, M. Woodhouse, X. Sun, and M. A. Alam, "An analysis of the cost and performance of photovoltaic systems as a function of module area," NREL/TP–6A20-67006, 1351153, Apr. 7, 2017, NREL/TP–6A20–67 006, 1 351 153. DOI: `10.2172/1351153`.

[155] D. Ray, "Lazard's levelized cost of energy analysis—version 11.0," p. 22, 2017.

[156] D. M. Powell, M. T. Winkler, A. Goodrich, and T. Buonassisi, "Modeling the cost and minimum sustainable price of crystalline silicon photovoltaic manufacturing in the united states," *IEEE Journal of Photovoltaics*, vol. 3, no. 2, pp. 662–668, Apr. 2013. DOI: `10.1109/JPHOTOV.2012.2230056`.

[157] M. Woodhouse, D. Feldman, R. Fu, K. Horowitz, and D. Chung, "On the path to SunShot: The role of advancements in solar photovoltaic efficiency, reliability, and costs," p. 44,

[158] D. Feldman, R. Margolis, and A. Goodrich, "Photovoltaic (PV) pricing trends: Historical, recent, and near-term projections," p. 30,

[159] S. Philipps, "Photovoltaics report," p. 47,

[160] I. M. Peters, S. Sofia, J. Mailoa, and T. Buonassisi, "Techno-economic analysis of tandem photovoltaic systems," *RSC Advances*, vol. 6, no. 71, pp. 66 911–66 923, 2016. DOI: `10.1039/C6RA07553C`.

[161] N. M. Haegel, H. Atwater, T. Barnes, *et al.*, "Terawatt-scale photovoltaics: Transform global energy," *Science*, vol. 364, no. 6443, pp. 836–838, May 31, 2019. DOI: `10.1126/science.aaw1845`.

[162] D. M. Powell, R. Fu, K. Horowitz, P. A. Basore, M. Woodhouse, and T. Buonassisi, "The capital intensity of photovoltaics manufacturing: Barrier to scale and opportunity for innovation," *Energy & Environmental Science*, vol. 8, no. 12, pp. 3395–3408, 2015. DOI: `10.1039/C5EE01509J`.

[163] C. Tsai, G. Anderson, R. Thompson, and B. Wacker, "Control of silicon network structure in plasma deposition," *Journal of Non-Crystalline Solids*, vol. 114, pp. 151–153, Dec. 1989. DOI: `10.1016/0022-3093(89)90096-3`.

[164] L. Chen, Y. Z. Wang, Y. Wu, *et al.*, "Molecular beam epitaxy growth of CdTe on si(211)," presented at the Photonics Asia 2004, H. Gong, Y. Cai, and J.-P. Chatard, Eds., Beijing, China, Jan. 10, 2005, p. 684. DOI: `10.1117/12.573170`.

[165] J. S. Hill and G. N. Simpson, "A technique for the epitaxial growth of zinc sulphide on silicon," *Journal of Physics E: Scientific Instruments*, vol. 6, no. 3, pp. 299–302, Mar. 1973. DOI: `10.1088/0022-3735/6/3/029`.

[166] X. Zhou, S. Jiang, and W. P. Kirk, "Epitaxial growth of ZnS on bare and arsenic-passivated vicinal si(100) surfaces," *Journal of Applied Physics*, vol. 82, no. 5, pp. 2251–2262, Sep. 1997. DOI: `10.1063/1.366031`.

[167] M. Yokoyama, K.-i. Kashiro, and S.-i. Ohta, “High quality zinc sulfide epitaxial layers grown on (100) silicon by molecular beam epitaxy,” *Applied Physics Letters*, vol. 49, no. 7, pp. 411–412, Aug. 18, 1986. DOI: `10.1063/1.97604`.

[168] M. L. Madugu, O. I.-O. Olusola, O. K. Echendu, B. Kadem, and I. M. Dharmadasa, “Intrinsic doping in electrodeposited ZnS thin films for application in large-area optoelectronic devices,” *Journal of Electronic Materials*, vol. 45, no. 6, pp. 2710–2717, Jun. 2016. DOI: `10.1007/s11664-015-4310-7`.

[169] K. Ichino, Y. Matsuki, S. T. Lee, T. Nishikawa, M. Kitagawa, and H. Kobayashi, “Li-doped p-type ZnS grown by molecular beam epitaxy,” *physica status solidi (c)*, vol. 1, no. 4, pp. 710–713, Mar. 2004. DOI: `10.1002/pssc.200304125`.

[170] Xiaochuan Zhou, Shan Jiang, Feng Li, G. Spencer, R. Bate, and W. Kirk, “Molecular beam epitaxy of Si/ZnS/Si(100) heterostructures for fabrication of silicon-based quantum devices,” in *Proceedings IEEE/Cornell Conference on Advanced Concepts in High Speed Semiconductor Devices and Circuits*, Ithaca, NY, USA: IEEE, 1995, pp. 498–505. DOI: `10.1109/CORNEL.1995.482546`.

[171] M. Yokoyama, K.-i. Kashiro, and S.-i. Ohta, “Molecular beam epitaxial growth of ZnS on a (100)-oriented Si substrate,” *Journal of Crystal Growth*, vol. 81, no. 1, pp. 73–78, Feb. 1987. DOI: `10.1016/0022-0248(87)90368-X`.

[172] E. Wirthl, H. Sitter, and P. Bauer, “Monocrystalline (100)-oriented ZnS layers grown on Si by molecular beam epitaxy,” *Journal of Crystal Growth*, vol. 146, no. 1, pp. 404–407, Jan. 1995. DOI: `10.1016/0022-0248(94)00523-0`.

[173] S. W. Shin, J. P. Oh, C. W. Hong, *et al.*, “Origin of mechanoluminescence from cu-doped ZnS particles embedded in an elastomer film and its application in flexible electro-mechanoluminescent lighting devices,” *ACS Applied Materials & Interfaces*, vol. 8, no. 2, pp. 1098–1103, Jan. 20, 2016. DOI: `10.1021/acsami.5b07594`.

[174] L. Svob, C. Thiandoume, A. Lusson, M. Bouanani, Y. Marfaing, and O. Gorochov, “*p* -type doping with n and li acceptors of ZnS grown by metalorganic vapor phase epitaxy,” *Applied Physics Letters*, vol. 76, no. 13, pp. 1695–1697, Mar. 27, 2000. DOI: `10.1063/1.126139`.

[175] M. Yokoyama, K.-i. Kashiro, and S.-i. Ohta, “Substrate temperature effect on crystallographic quality and surface morphology of zinc sulfide films on (100)-oriented silicon substrates by molecular-beam epitaxy,” *Journal of Applied Physics*, vol. 60, no. 10, pp. 3508–3511, Nov. 15, 1986. DOI: `10.1063/1.337602`.

[176] Y. Yongnian, C. F. Hickey, and U. J. Gibson, “ZnS molecular beam epitaxy on silicon substrates,” *Thin Solid Films*, vol. 151, no. 2, pp. 207–214, Aug. 1987. DOI: `10.1016/0040-6090(87)90234-3`.

[177] K. Ichino, A. Kotani, H. Tanaka, and T. Kawai, “ZnS:N and ZnS:N,Ag grown by molecular beam epitaxy,” *physica status solidi (c)*, vol. 7, no. 6, pp. 1504–1506, Apr. 1, 2010. DOI: `10.1002/pssc.200983239`.

[178] H. Cheng, S. Mohapatra, J. Potts, and T. Smith, “Effects of beam pressure ratios on film quality in MBE growth of ZnSe,” *Journal of Crystal Growth*, vol. 81, no. 1, pp. 512–517, Feb. 1987. DOI: `10.1016/0022-0248(87)90445-3`.

[179] V. H. Méndez-García, M. López-López, and I. Hernández-Calderón, “ZnSe epitaxial films grown by MBE on nitrogen treated Si(111) substrates,” p. 5, 1999.

[180] S. Adachi, *Optical Constants of Crystalline and Amorphous Semiconductors*. Boston, MA: Springer US, 1999. DOI: `10.1007/978-1-4615-5247-5`.

[181] H. Fritzsche and K.-J. Chen, “Drift-mobility measurements in amorphous semiconductors using traveling-wave method,” *Physical Review B*, vol. 28, no. 8, pp. 4900–4902, Oct. 15, 1983. DOI: `10.1103/PhysRevB.28.4900`.

[182] T. Tiedje, J. M. Cebulka, D. L. Morel, and B. Abeles, “Evidence for exponential band tails in amorphous silicon hydride,” *Physical Review Letters*, vol. 46, no. 21, pp. 1425–1428, May 25, 1981. DOI: `10.1103/PhysRevLett.46.1425`.

[183] M. J. Powell and S. C. Deane, “Improved defect-pool model for charged defects in amorphous silicon,” *Physical Review B*, vol. 48, no. 15, pp. 10 815–10 827, Oct. 15, 1993. DOI: `10.1103/PhysRevB.48.10815`.

[184] M. Lu, U. Das, S. Bowden, S. Hegedus, and R. Birkmire, “Optimization of interdigitated back contact silicon heterojunction solar cells by two-dimensional numerical simulation,” in *2009 34th IEEE Photovoltaic Specialists Conference (PVSC)*, Philadelphia, PA, USA: IEEE, Jun. 2009, pp. 001 475–001 480. DOI: `10.1109/PVSC.2009.5411332`.

[185] M. Schmidt, L. Korte, A. Laades, *et al.*, “Physical aspects of a-Si:H/c-Si hetero-junction solar cells,” *Thin Solid Films*, vol. 515, no. 19, pp. 7475–7480, Jul. 2007. DOI: `10.1016/j.tsf.2006.11.087`.

[186] K. Ghosh, S. Bowden, and C. Tracy, “Role of hot carriers in the interfacial transport in amorphous silicon/crystalline silicon heterostructure solar cells,” *physica status solidi (a)*, vol. 210, no. 2, pp. 413–419, Feb. 2013. DOI: `10.1002/pssa.201228277`.

[187] J. L. Hartke, “The three-dimensional Poole-Frenkel effect,” *Journal of Applied Physics*, vol. 39, no. 10, pp. 4871–4873, Sep. 1968. DOI: `10.1063/1.1655871`.

[188] J. M. Shannon and K. J. B. M. Nieuwesteeg, “Tunneling effective mass in hydrogenated amorphous silicon,” *Applied Physics Letters*, vol. 62, no. 15, pp. 1815–1817, Apr. 12, 1993. DOI: `10.1063/1.109558`.

[189] J. Endres, M. Kulbak, L. Zhao, *et al.*, “Electronic structure of the $CsPbBr_3$ /polytriarylamine (PTAA) system,” *Journal of Applied Physics*, vol. 121, no. 3, p. 035 304, Jan. 21, 2017. DOI: `10.1063/1.4974471`.

[190] Y. Zhao, J. Chen, W. Chen, and D. Ma, “Poly(3,4-ethylenedioxythiophene): Poly(styrenesulfonate)/MoO_3 composite layer for efficient and stable hole injection in organic semiconductors,” *Journal of Applied Physics*, vol. 111, no. 4, p. 043 716, Feb. 15, 2012. DOI: `10.1063/1.3687933`.

[191] Hock-Chun Chin, Ming Zhu, Xinke Liu, *et al.*, “Silane–ammonia surface passivation for gallium arsenide surface-channel n-MOSFETs,” *IEEE Electron Device Letters*, vol. 30, no. 2, pp. 110–112, Feb. 2009. DOI: `10.1109/LED.2008.2010831`.

[192] H. L. Hartnagel, “XPS analysis of (100) GaAs surfaces after applying a variety of technology-etchants,” p. 6,

[193] C.-C. Negrila, M. F. Lazarescu, C. Logofatu, *et al.*, “XPS analysis of AuGeNi/cleaved GaAs(110) interface,” *Journal of Nanomaterials*, vol. 2016, pp. 1–6, 2016. DOI: `10.1155/2016/7574526`.

[194] I. Aller, “InP exposure to hydrogen plasma with DC potential control,” *Journal of The Electrochemical Society*, vol. 140, no. 9, p. 2715, 1993. DOI: `10.1149/1.2220892`.

[195] N. Preissler, O. Bierwagen, A. T. Ramu, and J. S. Speck, “Electrical transport, electrothermal transport, and effective electron mass in single-crystalline in 2 o 3 films,” *Physical Review B*, vol. 88, no. 8, p. 085 305, Aug. 7, 2013. DOI: `10.1103/PhysRevB.88.085305`.

[196] B. Khamala, L. Franklin, Y. Malozovsky, A. Stewart, H. Saleem, and D. Bagayoko, “Calculated electronic, transport, and bulk properties of zincblende zinc sulphide (zb-ZnS),” *Computational Condensed Matter*, vol. 6, pp. 18–23, Mar. 2016. DOI: `10.1016/j.cocom.2015.12.001`.

[197] G. Agawane, S. W. Shin, S. Vanalakar, *et al.*, “Corrigendum to: Non-toxic novel route synthesis and characterization of nanocrystalline ZnS se1 thin films with tunable band gap characteristics [mater. res. bull. 55 (2014) 106-113],” *Materials Research Bulletin*, vol. 57, p. 339, Sep. 2014. DOI: `10.1016/j.materresbull.2014.05.026`.

[198] H. E. Ruda and B. Lai, “Electron transport in ZnS,” *Journal of Applied Physics*, vol. 68, no. 4, pp. 1714–1719, Aug. 15, 1990. DOI: `10.1063/1.346599`.

[199] G. H. E. Al-Shabeeb, A. K. Arof, A. K. Yahya, and S. Alam, “Energy gap calculations for ZnS_xSe_{1x},” presented at the PROGRESS OF PHYSICS RESEARCH IN Malayasia: PERFIK2009, Malacca (Malaysia), 2010, pp. 97–100. DOI: `10.1063/1.3469743`.

[200] C. S. Wang and B. M. Klein, “First-principles electronic structure of Si, Ge, GaP, GaAs, ZnS, and ZnSe. I. self-consistent energy bands, charge densities, and effective masses,” *Physical Review B*, vol. 24, no. 6, pp. 3393–3416, Sep. 15, 1981. DOI: `10.1103/PhysRevB.24.3393`.

[201] J. Liu, A. X. Wei, M. X. Zhuang, and Y. Zhao, “Investigation of the ZnSxSe1-x thin films prepared by chemical bath deposition,” *Journal of Materials Science: Materials in Electronics*, vol. 24, no. 4, pp. 1348–1353, Apr. 2013. DOI: `10.1007/s10854-012-0932-1`.

[202] D. Trefon-Radziejewska, J. Bodzenta, B. Toroń, Ł. Drewniak, and A. Marasek, “Investigations of thermal, optical, and electric properties as a function of composition for ZnS_xSe_{1x} crystals,” *International Journal of Thermophysics*, vol. 36, no. 9, pp. 2486–2495, Sep. 2015. DOI: `10.1007/s10765-015-1900-9`.

[203] G. Agawane, S. W. Shin, S. Vanalakar, *et al.*, “Non-toxic novel route synthesis and characterization of nanocrystalline ZnSxSe1x thin films with tunable band gap characteristics,” *Materials Research Bulletin*, vol. 55, pp. 106–113, Jul. 2014. DOI: `10.1016/j.materresbull.2014.04.002`.

[204] W. Gebhardt, “Preparation and optical properties of wide gap II–VI compounds,” *Materials Science and Engineering: B*, vol. 11, no. 1, pp. 1–9, Jan. 1992. DOI: `10.1016/0921-5107(92)90180-H`.

[205] R. G. Valeev, E. A. Romanov, V. L. Vorobiev, *et al.*, “Structure and properties of ZnS_{x} se_{1x} thin films deposited by thermal evaporation of ZnS and ZnSe powder mixtures,” *Materials Research Express*, vol. 2, no. 2, p. 025 006, Jan. 26, 2015. DOI: `10.1088/2053-1591/2/2/025006`.

[206] L. Zhang, C. Liu, Q. Yang, L. Cui, and Y. Zeng, “Growth and characterization of highly nitrogen doped ZnTe films on GaAs (001) by molecular beam epitaxy,” *Materials Science in Semiconductor Processing*, vol. 29, pp. 351–356, Jan. 2015. DOI: `10.1016/j.mssp.2014.06.045`.

[207] T. Baron, K. Saminadayar, and N. Magnea, “Nitrogen doping of Te-based II–VI compounds during growth by molecular beam epitaxy,” *Journal of Applied Physics*, vol. 83, no. 3, pp. 1354–1370, Feb. 1998. DOI: `10.1063/1.366838`.

[208] A. E. Rakhshani and S. Thomas, "Nitrogen doping of ZnTe for the preparation of ZnTe/ZnO light-emitting diode," *Journal of Materials Science*, vol. 48, no. 18, pp. 6386–6392, Sep. 2013. DOI: `10.1007/s10853-013-7438-y`.

[209] R. Kodama, T. Seldrum, X. Wang, *et al.*, "Nitrogen plasma doping of single-crystal ZnTe and CdZnTe on Si by MBE," *Journal of Electronic Materials*, vol. 42, no. 11, pp. 3239–3242, Nov. 2013. DOI: `10.1007/s11664-013-2810-x`.

[210] C.-H. Hsu, C.-Y. Yan, W.-H. Kao, Y.-T. Yu, and H.-H. Tung, "Properties of ZnTe thin films on silicon substrate," *Ferroelectrics*, vol. 491, no. 1, pp. 118–126, Jan. 26, 2016. DOI: `10.1080/00150193.2015.1071135`.

[211] P. Laukkanen, J. Sadowski, and M. Guina, "Surface studies by low-energy electron diffraction and reflection high-energy-electron diffraction," in *Semiconductor Research*, A. Patane and N. Balkan, Eds., vol. 150, Series Title: Springer Series in Materials Science, Berlin, Heidelberg: Springer Berlin Heidelberg, 2012, pp. 1–21. DOI: `10.1007/978-3-642-23351-7_1`.

[212] A. Stern. "Sterilization abuse in state prisons: Time to break with california's long eugenic patterns," HuffPost. Library Catalog: www.huffpost.com Section: Politics. (400).

[213] W. Shockley, "Is quality of U.S. population declining?" *U.S. News & World Reports*, vol. 59, no. 21, pp. 68–71, Nov. 22, 1965.

[214] *Firing Line with William F. Buckley Jr.: Shockley's Thesis*, Firing Line, Jun. 10, 1974.

[215] R. Kessler, "Absent at the creation; how one scientist made off with the biggest invention since the light bulb," *The Washington Post Magazine*, p. 16, Apr. 6, 1997.

[216] 5. W. S. Leadership. "Silence is never neutral; neither is science," Scientific American Blog Network. ().

[217] F. Galton, *Inquiries into Human Faculty and its Development*. London: Macmillan Publishers, 1883.

[218] E. Black, *War against the weak: eugenics and America's campaign to create a master race*. New York, NY: Four Walls Eight Windows, 2003, 550 pp., OCLC: 845588913.

[219] G. E. Allen, "Eugenics and modern biology: Critiques of eugenics, 1910-1945: Eugenics and its critics," *Annals of Human Genetics*, vol. 75, no. 3, pp. 314–325, May 2011. DOI: `10.1111/j.1469-1809.2011.00649.x`.

[220] W. Shockley, "Models, mathematics, and the moral obligation to diagnose the origin of negro iq deficits," *Review of Educational Research*, vol. 41, no. 4, pp. 369–377, 1971. DOI: `10.3102/00346543041004369`.

[221] C. A. Okoro, N. D. Hollis, A. C. Cyrus, and S. Griffin-Blake, "Prevalence of disabilities and health care access by disability status and type among adults — united states, 2016," *MMWR. Morbidity and Mortality Weekly Report*, vol. 67, no. 32, pp. 882–887, Aug. 17, 2018. DOI: `10.15585/mmwr.mm6732a3`.

[222] B. Ehrler, E. M. Hutter, and J. J. Berry, "The complicated morality of named inventions," *ACS Energy Letters*, pp. 565–567, Jan. 19, 2021. DOI: `10.1021/acsenergylett.0c02657`.

[223] "Silence is never neutral; neither is science," *Scientific American*, Jun. 6, 2020.

[224] B. D. Tatum, *"Why are all the black kids sitting together in the cafeteria?": and other conversations about race*, Third trade paperback edition. New York: Basic Books, 2017, 453 pp.

[225] A. J. Fisher, R. Mendoza-Denton, C. Patt, *et al.*, "Structure and belonging: Pathways to success for underrepresented minority and women PhD students in STEM fields," *PLOS ONE*, vol. 14, no. 1, L. G. Koniaris, Ed., e0209279, Jan. 9, 2019. DOI: `10.1371/journal.pone.0209279`.

[226] G. L. Krahn, D. K. Walker, and R. Correa-De-Araujo, "Persons with disabilities as an unrecognized health disparity population," *American Journal of Public Health*, vol. 105 Suppl 2, S198–206, Apr. 2015. DOI: `10.2105/AJPH.2014.302182`.

[227] R. Greenwood, C. R. Hinings, and R. Suddaby, "Theorizing change: The role of professional associations in the transformation of institutionalized fields," *Academy of Management Journal*, vol. 45, no. 1, pp. 58–80, Feb. 1, 2002. DOI: `10.2307/3069285`.

[228] B. Chen and D. M. McNamara, "Disability discrimination, medical rationing and COVID-19," *Asian Bioethics Review*, pp. 1–8, Sep. 3, 2020. DOI: `10.1007/s41649-020-00147-x`.

[229] P. South, *Lack of medical care, unsafe work practices, and absence of adequate protection against COVID-19 for detained immigrants and employees alike at teh irwin county detention center*, Sep. 14, 2020.

[230] R. für Volksgesundheitsdienst., *The law for the prevention of hereditarily diesased offspring. ("gesetz zur verhütung erbkranken nachwuchses")*, Jul. 14, 1933.

[231] A. M. Stern, "Sterilized in the name of public health: Race, immigration, and reproductive control in modern California," *American Journal of Public Health*, vol. 95, no. 7, pp. 1128–1138, Jul. 2005. DOI: `10.2105/AJPH.2004.041608`.

[232] J.-J. Amy and S. Rowlands, "Legalised non-consensual sterilisation – eugenics put into practice before 1945, and the aftermath. Part 1: USA, Japan, Canada and Mexico," *The European Journal of Contraception & Reproductive Health Care*, vol. 23, no. 2, pp. 121–129, 2018, Publisher: Taylor & Francis _eprint: https://doi.org/10.1080/13625187.2018.1450973. DOI: `10.1080/13625187.2018.1450973`.

[233] *Americans with disability act of 1990*, Jul. 26, 1990.

[234] S. Bowden, K. Ghosh, and C. Honsberg, "Non PN junction solar cells using carrier selective contacts," in *Physics, Simulation, and Photonic Engineering of Photovoltaic Devices II*, A. Freundlich and J.-F. Guillemoles, Eds., Backup Publisher: International Society for Optics and Photonics, vol. 8620, SPIE, 2013, pp. 171–176. DOI: `10.1117/12.2004259`. [Online]. Available: `https://doi.org/10.1117/12.2004259`.

[235] "Science and Engineering Indicators 2020: The State of U.S. Science and Engineering.," National Science Board, National Science Foundation, NSB-2020-1, 2020.

[236] S. Philipps, "Photovoltaics report," Fraunhofer ISE, Sep. 16, 2020.

[237] D. Nesheva, M. Sćepanović, S. Askrabić, Z. Levi, I. Bineva, and Z. Popović, "Raman scattering from ZnSe nanolayers," *Acta Physica Polonica A*, vol. 116, no. 1, pp. 75–77, Jul. 2009. DOI: `10.12693/APhysPolA.116.75`.

[238] J. Lin, H. Jee, J. Yoo, J. Yi, C. Jeong, and J. Lee, "Surface passivation of crystalline silicon wafer using H2S gas," *Applied Sciences*, vol. 11, no. 8, p. 3527, Apr. 15, 2021. DOI: `10.3390/app11083527`.

[239] F. M. Mirabella, Ed., *Modern techniques in applied molecular spectroscopy*, Techniques in analytical chemistry series, New York: Wiley, 1998, 410 pp.

[240] J. Haschke, O. Dupré, M. Boccard, and C. Ballif, "Silicon heterojunction solar cells: Recent technological development and practical aspects - from lab to industry," *Solar Energy Materials and Solar Cells*, vol. 187, pp. 140–153, Dec. 2018. DOI: `10.1016/j.solmat.2018.07.018`.

[241] J. R. Sandercock, "Trends in brillouin scattering: Studies of opaque materials, supported films, and central modes," in *Light Scattering in Solids III*, M. Cardona and G. Güntherodt, Eds., vol. 51, Series Title: Topics in Applied Physics, Berlin, Heidelberg: Springer Berlin Heidelberg, 1982, pp. 173–206. DOI: `10.1007/3540115137_6`.

[242] S. Ho Song, E. S. Aydil, and S. A. Campbell, "Metal-oxide broken-gap tunnel junction for copper indium gallium diselenide tandem solar cells," *Solar Energy Materials and Solar Cells*, vol. 133, pp. 133–142, Feb. 2015. DOI: `10.1016/j.solmat.2014.10.046`.

[243] Z. Chen and T. F. Jaramillo, "The use of UV-visible spectroscopy to measure the band gap of a semiconductor," p. 18,

[244] P. S. Bagus, E. S. Ilton, and C. J. Nelin, "The interpretation of XPS spectra: Insights into materials properties," *Surface Science Reports*, vol. 68, no. 2, pp. 273–304, Jun. 2013. DOI: `10.1016/j.surfrep.2013.03.001`.

[245] C. Tan, S. Yin, J. Chen, *et al.*, "Broken-gap PtS_2/WSe_2 van der waals heterojunction with ultrahigh reverse rectification and fast photoresponse," *ACS Nano*, vol. 15, no. 5, pp. 8328–8337, May 25, 2021. DOI: `10.1021/acsnano.0c09593`.

[246] X. Yan, C. Liu, C. Li, *et al.*, "Tunable $SnSe_2$ /WSe_2 heterostructure tunneling field effect transistor," *Small*, vol. 13, no. 34, p. 1 701 478, Sep. 2017. DOI: `10.1002/smll.201701478`.

[247] D. L. Smith and V. Y. Pickhardt, "Molecular beam epitaxy of II-VI compounds," *Journal of Applied Physics*, vol. 46, no. 6, pp. 2366–2374, Jun. 1975. DOI: `10.1063/1.321915`.

[248] O. Dehaese, X. Wallart, O. Schuler, and F. Mollot, "X-ray photoemission characterization of interface abruptness and band offset of Ga0.5In0.5P grown on GaAs," *Journal of Applied Physics*, vol. 84, no. 4, pp. 2127–2132, 1998, Publisher: AIP Publishing. DOI: `10.1063/1.368357`.

[249] X. Huang, J. Li, Y. Zhang, and A. Mascarenhas, "From 1d chain to 3d network: Tuning hybrid II-VI nanostructures and their optical properties," *Journal of the American Chemical Society*, vol. 125, no. 23, pp. 7049–7055, Jun. 2003. DOI: `10.1021/ja0343611`.

[250] X. Huang and J. Li, "From single to multiple atomic layers: A unique approach to the systematic tuning of structures and properties of inorganic-organic hybrid nanostructured semiconductors," p. 18,

[251] X. Huang, J. Li, and H. Fu, "The first covalent organicinorganic networks of hybrid chalcogenides: Structures that may lead to a new type of quantum wells," *Journal of the American Chemical Society*, vol. 122, no. 36, pp. 8789–8790, Sep. 2000. DOI: `10.1021/ja002224n`.

[252] S. Wang and J. Li, "Two-dimensional inorganic–organic hybrid semiconductors composed of double-layered ZnS and monoamines with aromatic and heterocyclic aliphatic rings: Syntheses, structures, and properties," *Journal of Solid State Chemistry*, vol. 224, pp. 40–44, Apr. 2015. DOI: `10.1016/j.jssc.2014.03.016`.

[253] Y. Kim, P. C. Wu, R. Sokhoyan, *et al.*, "Phase modulation with electrically tunable vanadium dioxide phase-change metasurfaces," *Nano Letters*, vol. 19, no. 6, pp. 3961–3968, Jun. 12, 2019,
R.G. gathered and analyzed data and helped write the manuscript. DOI: `10.1021/acs.nanolett.9b01246`.

[254] P. Jahelka, R. Glaudell, and H. Atwater, “Non-epitxaial GaAs/organic heterojunction solar cells with 830mv Voc,” in *2020 47th IEEE Photovoltaic Specialists Conference (PVSC)*,
R.G. gathered and analyzed data and helped write the manuscript., Calgary, AB, Canada: IEEE, Jun. 14, 2020, pp. 0649–0651. DOI: `10.1109/PVSC45281.2020.9300460`.

[255] R. Glaudell, “Women* in Physics, Math and Astronomy at Caltech: Supporting Women in STEM,” in *2020 47th IEEE Photovoltaic Specialists Conference (PVSC)*,
R.G. conceived of this work, gathered and analyzed data, and wrote the manuscript., Calgary, AB, Canada: IEEE, Jun. 14, 2020, pp. 2147–2150. DOI: `10.1109/PVSC45281.2020.9300477`.

[256] R. D. Glaudell and H. A. Atwater, “Energy band alignment of ZnS_xSe_{1-x} films on Si for photovoltaic carrier-selective contacts,” in *2018 IEEE 7th World Conference on Photovoltaic Energy Conversion (WCPEC) (A Joint Conference of 45th IEEE PVSC, 28th PVSEC & 34th EU PVSEC)*,
R.G. participated in the conception of this project, fabricated samples, gathered and analyzed data, and wrote the manuscript., Waikoloa Village, HI: IEEE, Jun. 2018, pp. 2132–2134. DOI: `10.1109/PVSC.2018.8548022`.

[257] R. Glaudell, P. Balaji, S. Bowden, A. Augusto, and H. A. Atwater, “ZnS_xse_{1-x} carrier-selective contacts for silicon photovoltaics,” in *2021 IEEE 48th Photovoltaic Specialists Conference (PVSC)*,
R.G. participated in the conception of this project, fabricated samples, gathered and analyzed data, and wrote the manuscript., Fort Lauderdale, FL, USA: IEEE, Jun. 20, 2021, pp. 0652–0655. DOI: `10.1109/PVSC43889.2021.9518976`.

[258] R. Glaudell, “The Legacy of William Shockley: Racism and Ableism in STEM,” in *2021 IEEE 48th Photovoltaic Specialists Conference (PVSC)*,
R.G. participated in the conception of this work, gathered and analyzed data, and wrote the manuscript., Fort Lauderdale, FL, USA: IEEE, Jun. 20, 2021, pp. 1887–1889. DOI: `10.1109/PVSC43889.2021.9518411`.

[259] M. E. Phelan, M. M. Potter, P. Balaji, *et al.*, “Fabrication techniques for high-performance Si heterojunction (SHJ) microcells,” in *2021 IEEE 48th Photovoltaic Specialists Conference (PVSC)*,
R.G. gathered and analyzed data and helped write the manuscript., Fort Lauderdale, FL, USA: IEEE, Jun. 20, 2021, pp. 0330–0334. DOI: `10.1109/PVSC43889.2021.9518579`.

[260] H. Lieth and R. H. Whittaker, *Primary productivity of the biosphere*, ser. Ecological studies v. 14. New York: Springer-Verlag, 1975, 339 pp.

[261] S. M. Sze and K. K. Ng, *Physics of semiconductor devices*, 3rd ed. Hoboken, N.J: Wiley-Interscience, 2007, 815 pp.

[262] K. Seshan, Ed., *Handbook of thin-film deposition processes and techniques: principles, methods, equipment, and applications*, 2nd ed, Norwich, N.Y: Noyes Publications, 2002, 629 pp.

[263] *Practical surface analysis. 1: Auger and X-ray photoelectron spectroscopy*, 2. ed., repr. Chichester: Wiley, 1996, 657 pp.

[264] A. Luque and S. Hegedus, Eds., *Handbook of photovoltaic science and engineering*, Hoboken, NJ: Wiley, 2003, 1138 pp.

[265] P. Malanima, *Energy consumption in Italy in the 19th and 20th centuries: a statistical outline*. Naples: Consiglio nazionale delle ricerche, Istituto di studi sulle società del Mediterraneo, 2006, 140 pp.

[266] M. M. Potter, M. E. Phelan, P. Balaji, *et al.*, "Silicon heterojunction microcells," *ACS Applied Materials & Interfaces*, vol. 13, no. 38, pp. 45 600–45 608, Sep. 29, 2021,
R.G. gathered and analyzed data and helped write the manuscript. DOI: `10.1021/acsami.1c11122`.